Lightning Excitation of the Ionospheric Alfvén Resonator

by

Charles Nokes

A thesis submitted in partial fulfillment of the requirements for the degree of

Master of Science

Department of Physics

University of Alberta

Abstract

The ionospheric Alfvén resonator (IAR) is an area of space that, due to sharp Alfvén speed gradients, has the ability to trap electromagnetic plasma wave energy, where it bounces in the Alfvén mode between near-Earth space and the lower ionosphere. Here we present research that, by comparing induction coil magnetometer data from the Canadian Array for Real-time Investigations of Magnetic Activity (CARISMA) with world lightning occurrence data from the World Wide Lightning Location Network (WWLLN), has revealed strong evidence that energy released in terrestrial lightning storms can enter this resonator. Energy from lightning strikes is ducted through the Earth-Ionosphere cavity, generating the well-defined Schumann resonances (SR) with a fundamental frequency of 7.8 Hz. Our results show that in addition to the Schumann resonances, the lightning energy perturbs magnetic field lines as it propagates, generating Alfvén waves that travel up the magnetic field lines towards near-Earth space, and in regions where the ionospheric Alfvén resonator is active, these Alfvén waves are reflected back down from the peak in the Alfvén speed, resulting in one or more echo pulses in the time series magnetometer data. Using the superposed epoch analysis technique reveals two critical characteristics of this paradigm: 1) the pulse-echo(s) signal in the time series, which occur on the scale of 1-2 seconds, is defined by the characteristics of the local resonator, and this is most clearly shown by the spectra of the time series signal; and 2) this pulse-echo signal in the time series has been measured for lightning occurring at large distances, beyond 8000 km from the magnetometer instru-

ment, which contradicts earlier assumptions that the lightning pulse needed to be local (or less than 2000 km away) from the ionospheric Alfvén resonator active region of the ionosphere. Our results suggest the coupling between SR and IAR is a global phenomenon. Lightning might act as a continuous source for Alfvén wave energy input into the magnetosphere with potentially important but heretofore unknown consequences for magnetospheric physics. This provides an interface between space weather and the terrestrial global electric circuit. Future work should reveal more details about this previously unknown pathway for magnetosphere-ionosphere-atmosphere coupling.

Preface

The research in this thesis was conducted by the author.

Dr. Robert Holzworth, Director of the World Wide Lightning Location Network (WWLLN) and Professor of Earth and Space Sciences at the University of Washington provided the WWLLN data files used in the analyses of this thesis, following a request from the author. The WWLLN data are copyrighted, and so the raw stroke location files provided for the analyses cannot be copied and distributed. Further information about the WWLLN data and how to contact Professor Holzworth are provided in Appendix A.

Chapter 4 presents the experimental discovery and validation of the hypothesis that the ionospheric Alfvén resonator (IAR) is excited by lightning. This proposition is supported with very strong evidence from results of the superposed epoch analysis using induction coil magnetometer data from the Canadian Array for Real-time Investigations of Magnetic Activity (CARISMA), correlated with lightning data from the World Wide Lightning Location Network (WWLLN). This chapter is currently being prepared for publication.

Chapter 5 demonstrates that IAR excitation due to lightning is not simply limited to lightning within a radius local to the magnetometer, but also allows for non-local lightning - over 8000 km away - to provide the excitation. These observations describe a physical mechanism whereby lightning energy is first ducted in the Earth-Ionosphere waveguide, even over great distances, at speeds close to the speed of light, but continuously perturbs the field lines as it travels in the Earth-ionosphere waveguide, thereby continuously sending

Alfvén wave pulses up into the IAR and exciting waves inside the IAR even far from the initial lightning strike. This chapter is currently being prepared for publication.

To Nic Moore and Davis Falniuk

Acknowledgements

Data availability

Acknowledgements

Contents

List of Tables

List of Figures

Chapter 1

Introduction

1.1 Thesis Overview

The ionospheric Alfvén resonator (IAR) was first proposed by *Polyakov*, 1976. Magnetic field measurements soon verified its existence, yet even today the mechanism for its excitation remains a topic of debate informed mostly by models and theory. This thesis presents data driven results that clearly demonstrate global lightning activity as a major excitation mechanism for the IAR, revealing a new paradigm coupling atmospheric lightning energy into the ionosphere and magnetosphere.

Chapter 1 provides an overview of the Sun-Earth space weather system. Specifically, it introduces the basic concepts of space plasmas near the Earth, the characteristics of the magnetosphere and the ionosphere, the interaction of these plasma regions with the Earth's magnetic field as defined by magnetohydrodynamic theory, how this results in the formation of perturbations such as shear Alfvén waves, the environmental conditions that result in Alfvén wave reflections and resonance inside the ionospheric Alfvén resonator, and finally basic electromagnetic characteristics of lightning and the fair weather global electric circuit.

Chapter 2 presents an overview of magnetohydrodynamic wave theory, Alfvén waves, and gives an in depth examination of the Ionospheric Alfvén Resonator (IAR), the historical background of its discovery, and characteristics of the harmonics of the Alfvén modes trapped inside the IAR.

Chapter 3 outlines the instrumentation and the datasets that were used

to investigate the relationship between lightning and the IAR. Specifically, we outline how the data was collected and an overview of the data analysis techniques employed, such as time domain analysis, frequency domain analysis, filter design theory, fast-fourier transforms, peak-finding, superposed epoch analysis, and the experimental discovery and validation of the hypothesis that the IAR is excited by lightning.

Chapter 4 presents the experimental discovery and validation of the hypothesis that the IAR is excited by lightning. This proposition is supported with very strong evidence from results of the superposed epoch analysis using induction coil magnetometer data from the Canadian Array for Realtime Investigations of Magnetic Activity (CARISMA), correlated with lightning data from the World Wide Lightning Location Network (WWLLN).

Chapter 5 demonstrates that IAR excitation due to lightning is not simply limited to lightning within a radius local to the magnetometer, but also allows for non-local lightning - over 8000 km away - to provide the excitation. These observations describe a physical mechanism whereby lightning energy is first ducted in the Earth-Ionosphere waveguide, even over great distances, at speeds close to the speed of light, but continuously perturbs the field lines as it travels in the Earth-ionosphere waveguide, thereby continuously sending Alfvén wave pulses up into the IAR and exciting waves inside the IAR even far from the initial lightning strike.

Chapter 6 summarises the discoveries presented in this thesis and presents opportunities for future work. This includes suggestions for future work addressing the properties of individual lightning strikes that excite the IAR, such as their polarity or their energy, or how the results presented here could be used to determine the conductivity of the lower boundary of the ionosphere.

1.2 The Solar-Terrestrial Connection

The sun drives major atmospheric weather and space weather systems. This thesis explores the excitation of the Ionospheric Alfvén Resonator by lightning, delving into the interaction between the neutral atmosphere and the

near-Earth plasma environment. The objective of this chapter is to contextualize this research project by providing a brief introduction to the solar wind, the magnetosphere, the ionosphere, the atmosphere, and briefly describe how terrestrial lightning interacts with the Earth's magnetic field to produce oscillating Alfvén waves within the coupled atmosphere-ionosphere-magnetosphere system.
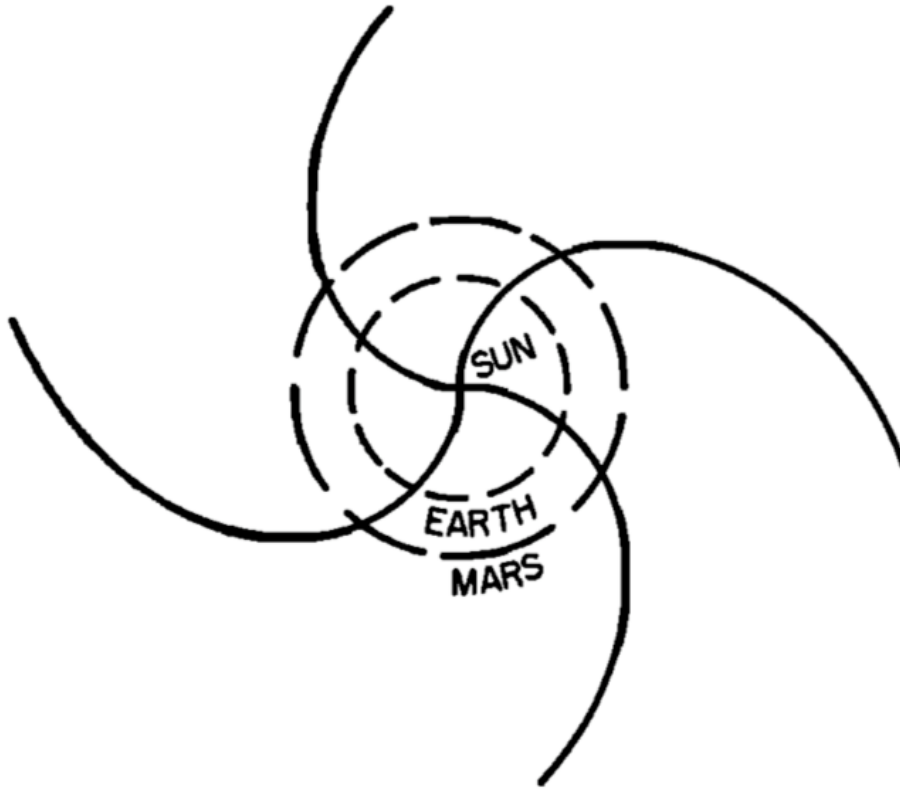
Figure 1.1: Illustration of the Parker spiral representing the interplanetary magnetic field (IMF) frozen in to the solar wind plasma environment (taken from *Parker*, 1959).

1.3   The Sun and Solar Wind

It was *Parker* (1959) who first suggested the sun emits a stream of highly conducting plasma of electrons and protons, now known as the solar wind, a term conceived in that landmark paper. This stream of particles is emitted because the solar atmosphere is sufficiently hot to be able to overcome the

sun's gravity through solar coronal holes, which form when the sun's magnetic field lines stretch out into distant interplanetary space. The solar magnetic field is frozen into the solar wind, due to the high conductivity of the plasma, and is carried out into the solar system as the solar wind expands. Due to the rotation of the sun, this interplanetary magnetic field (IMF) flows out in the form of a spiral (now named the Parker spiral), as demonstrated in Figure (1.1). The direction of the IMF in the ecliptic plane, sunward or anti-sunward, forms sectors that result in current sheets at the boundaries between sunward and anti-sunward field lines. Due to the solar rotation, the current sheet tilts in a wave pattern most similar to the shape taken by the skirt of a spinning ballerina.

Sudden releases of magnetic energy from the solar atmosphere result in powerful ejections of solar wind plasma at higher than normal speeds. This ejection of material is called a Coronal Mass Ejection (CME), which is often preceded by a sudden increase in light intensity emitted by the sun - a solar flare. Today it is understood that the solar wind travels outward into interplanetary space at typical speeds of 400 to 750 km s^{-1}. This qualifies as supersonic and super-Alfvénic flow. Table (1.1) lists some characteristics of the solar-terrestrial environment.

Characteristic	Typical Value	Alternative Unit
Sun-Earth Distance	1.5×10^8 km	1 AU
Earth Radius (R_E)	6378 km	1 R_E
Solar wind speed	$\sim$400-750 km/s	-
Solar wind electron density	$\sim$5 cm^{-3}	-
Solar wind electron temperature	$\sim 10^5$ K	$\approx$ 10 eV
IMF B field	5 nT	-
Earth dipole moment	8.05×10^{22} Am^2	-
Earth B Field at magnetopause	$\sim$31 nT	-
Earth B Field at surface	3.11×10^4 nT	-
Magnetopause standoff distance	$\sim$63,780 km	10 R_E
Magnetotail distance	6.4-12.8$\times 10^5$ km	100-200 R_E
Ionosphere distance from Earth	see section 1.5.2	-
Solar wind Alfvén speeds	$\sim$30-50 km/s	-

Table 1.1: Values of typical parameters related to solar-terrestrial space plasma physics (*Baumjohann* et al., 1996).

4

When it reaches the Earth, the solar wind plasma and solar wind magnetic field encounter the Earth's own dipolar magnetic field, which acts as a large protective barrier, forming an upstream supersonic shock front, named the bow shock, illustrated in Figure 1.2.
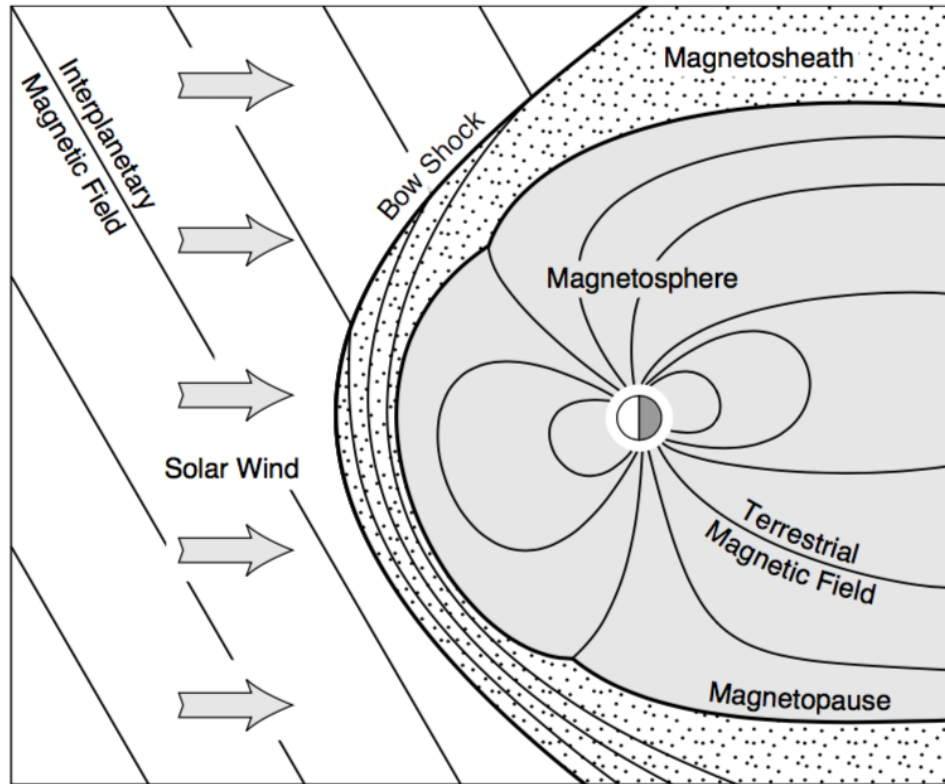
Figure 1.2: Diagram showing interaction of the solar wind and interplanetary magnetic field (IMF) with the geomagnetic field, and the resulting regions formed within (taken from *Baumjohann* et al., 1996).

1.4 The Magnetosphere

At the Earth, the dynamic pressure of the solar wind and the magnetic pressure of the geomagnetic field reach an equilibrium, forming a boundary that deflects the solar wind particles, since they are frozen into the solar magnetic field. The boundary that is formed is called the magnetopause, and the region on the Earth side of the magnetopause is the magnetosphere (Figure1.2). The solar wind encounters the geomagnetic field at supersonic speeds. The interplanetary magnetic field lines cannot easily penetrate through the geo-

magnetic field lines, however the pressure of the IMF sweeps the outer parts of the dipolar geomagnetic field, distorting and carrying the field lines out into the nightside to form a long magnetotail. During periods of higher solar wind speeds, the magnetosphere is compressed on the day side, and conversely in periods of lower solar wind speeds the magnetosphere can relax and expand outward.

Within the magnetosphere the plasma forms a series of layered regions with different temperatures and densities. The plasma is made up of electrons, protons, and small amounts of He^+, O^+, O^{2+}, N^+, N^{2+}, and He^{++} ions that come from the ionosphere and the solar wind. The different regions include the radiation belts, the plasmasphere, the plasma sheet, and the magnetotail lobe as shown schematically in Figure (1.3).
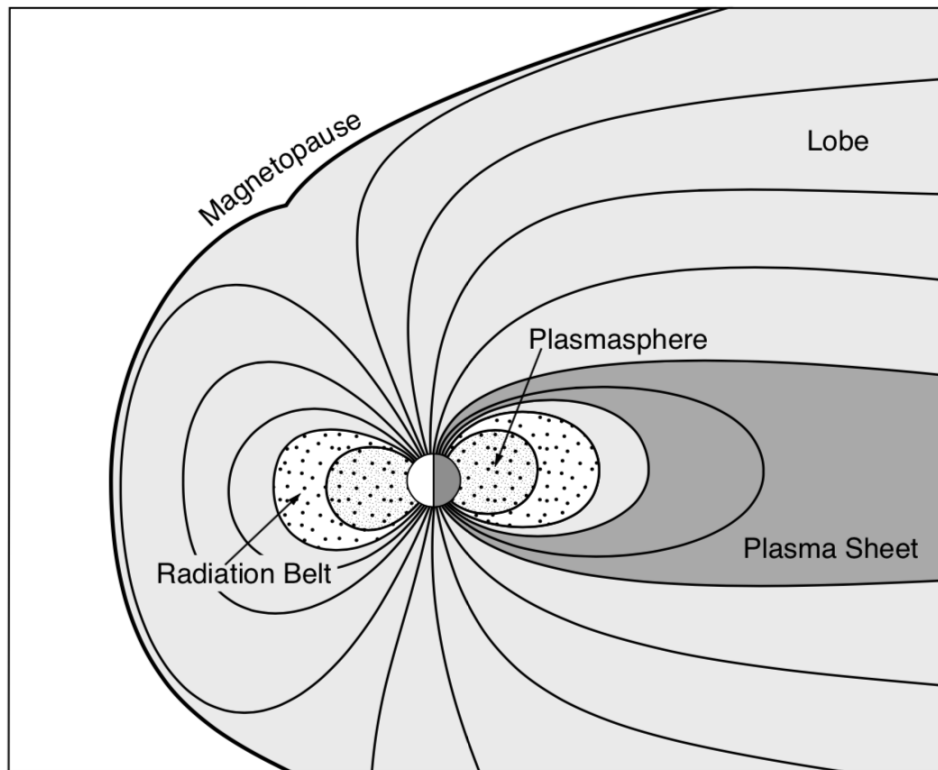
Figure 1.3: Diagram showing regions inside the magnetosphere (taken from *Baumjohann* et al., 1996).

1.4.1 Magnetic Reconnection

The direction of the geomagnetic field in the magnetosphere is defined by the orientation of the Earth's dipole, but the direction of the IMF is variable. When a southward directed IMF encounters the northward geomagnetic field, this gives rise to magnetic reconnection. This process involves the merging of anti-parallel magnetic field lines at a point in space where the two fields meet each other. One of the effects is the connection of the IMF to the geomagnetic field lines. This results in mixing of solar wind plasma with magnetospheric plasma particles, and creates open field lines that are swept to the nightside by the solar wind flow. Once in the nightside magnetotail, reconnection can once again occur, producing closed field lines. Due to the magnetic tension in the field lines, these stretched field lines are drawn Earthward and ultimately move around back to the dayside in order to conserve magnetic flux. This process, illustrated in figure (1.4) bears the name of the researcher who first proposed it: the Dungey cycle (*Dungey*, 1961).

The Dungey cycle is a convection cycle driven by the solar wind, which results in a curl of the magnetic field $\nabla \times \mathbf{B}$. From Ampères law, this means currents are also generated as a result of the flow of field lines from the dayside, over the poles, into the magnetotail, and then back around to the dayside at lower latitudes. These currents contribute to the Region 1 and Region 2 field-aligned currents (FACs) that are closed in the ionosphere, as described in (e.g., *Iijima* et al., 1978). Figure (1.5) illustrates how these currents flow from the magnetosphere through the ionosphere. The inner rings represent Region 1, the outer rings are Region 2 field-aligned currents, and these FAC systems close through sheet currents which flow in the ionosphere.

1.5 The Ionosphere

As ultraviolet rays collide with the Earth's atmosphere, a portion of the neutral particles that form the atmosphere ionize. In the dense regions of the neutral atmosphere, these ionized particles recombine rapidly, however above 80 km altitude the number of collisions between particles is too low for effective
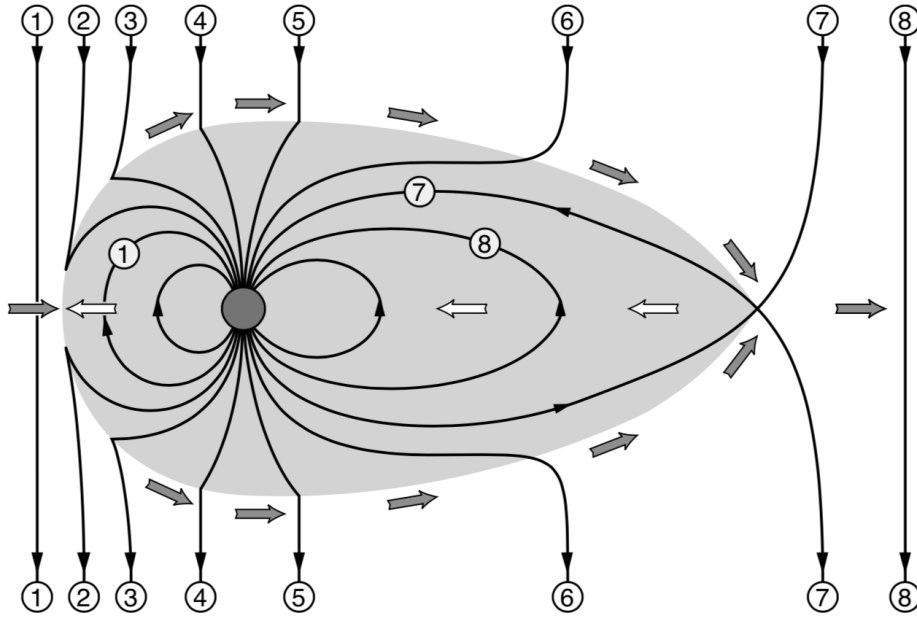
Figure 1.4: Illustration of reconnection and the Dungey cycle. 1-Southward interplanetary magnetic field line. 2 - reconnection with the geomagnetic field line creating open field lines. 3-6 - field lines are swept by the solar wind over the pole into the nightside magnetotail. 7 - reconnection in the nightside. 8 - closed field lines drawn back Earthward by tension of the Lorentz force, eventually being drawn back to the dayside. The open solar wind field line continues past Earth. (Taken from *Baumjohann* et al., 1996).
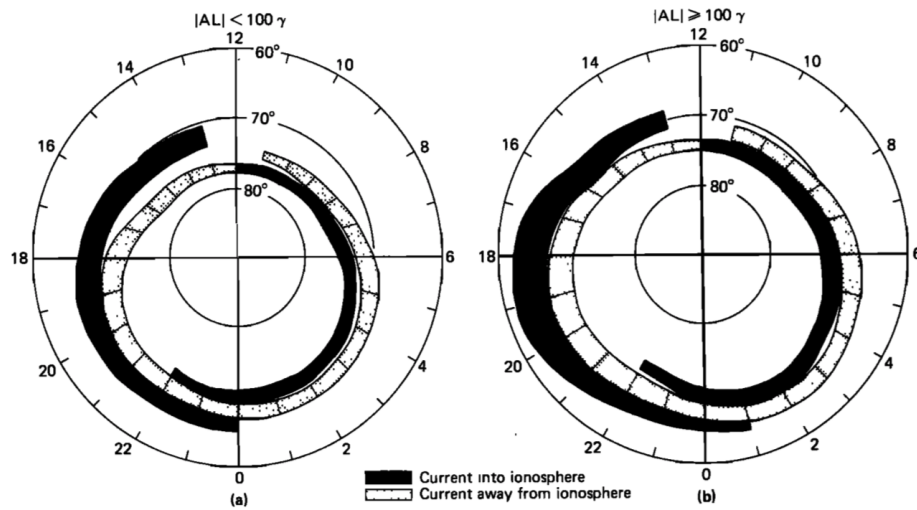
Figure 1.5: Diagram of the Region 1 and Region 2 field-aligned currents flowing from the magnetosphere through the ionosphere. (taken from *Iijima* et al., 1978).

recombination to take place. This results in the formation of a region of permanently ionized particles between the atmosphere, which forms a conducting region called the ionosphere (see e.g., *Hargreaves*, 1992 for more details). Particles from the solar wind, plasma sheet and magnetotail can also be drawn into the ionosphere during geomagnetic disturbances. Auroras are the by-product of the process when accelerated electrons from the magnetosphere precipitate into the neutral atmosphere near the poles along a magnetic field line. When they collide with and ionize neutral particles, photons of light are emitted.

1.5.1 Ionisation and Recombination

The formation of the ionosphere depends on four major processes. The two sources of ions and electrons are solar ultraviolet ionization and ionization by collisions with high energy particles. The two sinks of ions and electrons are recombination to reform neutral atoms, and the attachment of electrons to neutral atoms to form negative ions. In equilibrium the plasma is quasi-neutral, therefore the number density of positively charged ions (n_i) is roughly equal to the number density of electrons (n_e). Under these conditions the electron continuity equation takes the form (e.g., *Baumjohann* et al., 1996),

$$\frac{dn_e}{dt} = q_{v,e} - \alpha_r n_e^2 - \beta_r n_e \tag{1.1}$$

where $\frac{dn_e}{dt}$ is the rate of change in electron density, $q_{v,e}$ is the altitude dependent rate of ionisation due to photoionization and collisions with energetic particles, $-\alpha_r n_e^2$ is the recombination rate, and $-\beta_r n_e$ is the rate of attachment. The coefficients α_r and β_r encompass the photochemical mechanisms that affect the composition of the plasma at different altitudes. At lower altitudes recombination (α_r) dominates, whereas at higher altitudes attachment (β_r) is the dominant loss process.

1.5.2 Layers of the Ionosphere

The ionosphere separates roughly into three major regions called the D-, E-, and F-regions:

- D-region - 60 - 90 km, weakly ionized, $n_e \sim 10^8 - 10^{10}$ m^{-3};

- E-region - 90 - 150 km, partially ionized, $n_e \sim 10^{11}$ m^{-3}, peak ionization at 110 km,;

- F1-region - 150 - 250 km, partially ionized, $n_e \sim 10^{11} - 10^{12}$ m^{-3}, peak ionization at 200 km, ;

- F2-region - 250 - 500 km, partially ionized, $n_e \sim 10^{12}$ m^{-3}, peak ionization at 300 km,.

The D-layer is not considered a true plasma, as the collision frequency is high and the region is dominated by the neutral gas. The E-layer is the result of long wavelength (90 nm) ultraviolet photoionization with the molecularly dense oxygen between 90 and 150 km. The F region splits into two. The F1 region, which reaches a peak density profile near 200 km altitude, results from short wavelength (20-80 nm) ultraviolet photoionization on the dayside of the Earth. The F2 region is the densest plasma layer of the ionosphere. Its formation is driven by the altitude dependent processes in equation 1.1.

1.5.3 Ionospheric Pedersen and Hall Conductance

The density profile of the atmosphere results in different drift motions at different altitudes, which in turn drives currents together with the electric field in the ionosphere. As demonstrated in (e.g., *Hargreaves*, 1992), at low altitude, inside the D-region the high atmospheric density causes a high collision frequency with respect to the cyclotron frequency, thus the plasma flows with the neutral wind and the currents driven by the electric field are very small. At higher altitude, inside the F-region the collision frequency is low compared to the cyclotron frequency, therefore an anti-parallel drift of ions and electrons can result in a small current. Between these two, inside the E-region a region called the dynamo region supports currents given by (e.g., *Baker* et al., 1953):

$$\mathbf{J} = \sigma_{\parallel}\mathbf{E}_{\parallel} + \sigma_P\mathbf{E}_{\perp} + \sigma_H(\mathbf{B} \times \mathbf{E}_{\perp}) \tag{1.2}$$

where $\mathbf{J}$ is the current density, the first term on the right hand side is the longitudinal current density composed of the electric field component parallel to the magnetic field, $\mathbf{E}_\parallel$, and the parallel conductivity, $\sigma_\parallel$, (see e.g., *Baker* et al., 1953). This term can be ignored at mid and high latitudes as the magnetic field is essentially perpendicular to the electric field. The second term on the right is the Pedersen current density composed of the electric field component perpendicular to the magnetic field $\mathbf{E}_\perp$ and the Pedersen conductivity σ_P, where

$$\sigma_P = n_e e^2 \left[\frac{\nu_e}{(m_e(\omega_e^2 + \nu_e^2)} + \frac{\nu_i}{(m_i(\omega_i^2 + \nu_i^2))} \right] \tag{1.3}$$

and the third term on the right, which flows perpendicular to both $\mathbf{B}$ and the electric field, is the Hall current density and the Hall conductivity σ_H

$$\sigma_H = n_e e^2 \left[\frac{\omega_e}{(m_e(\omega_e^2 + \nu_e^2))} - \frac{\omega_i}{(m_i(\omega_i^2 + \nu_i^2))} \right]. \tag{1.4}$$

The height profiles of the Pedersen and Hall conductivity differ (e.g., *Hargreaves*, 1992) with the Pedersen conductivity peaking at higher altitude than the Hall conductivity. Together, the Pedersen and Hall currents in the dynamo region form a horizontal current sheet with a finite height. Thus the Pedersen and Hall conductivities can be integrated across the height of the sheet (e.g., *Hargreaves*, 1992), giving the Pedersen conductance Σ_P and the Hall conductance Σ_H. At mid to high latitudes, and under conditions where the conductivity is uniform, the Pedersen conductance dominates and plays a role in the reflection coefficient for Alfvén waves at the lower boundary of the ionospheric Alfvén resonator, which is detailed in subsection (2.3). In the general case, under conditions with non-uniform conductivity, the Pedersen and Hall conductances are of similar order, as detailed in *Yoshikawa* et al., 2000 and the references therein.

1.6 The Atmosphere

Below the D-layer of the ionosphere sits the neutral atmosphere, which also forms many sub-layers such as the troposphere. The troposphere reaches an

altitude of ~ 10 km and is where most weather systems, including thunderstorms and lightning, occur. Light energy from the sun drives winds, numerous cycles (water, carbon, nitrogen), and the weather across the globe. One mechanism that couples the atmosphere to the ionosphere and the magnetosphere, and terrestrial weather to space weather, is the fair weather global electric circuit and lightning.

1.6.1 The Fair Weather Global Electric Circuit

The Earth-ionosphere waveguide can be considered to form a global scale spherical capacitor, a concept proposed by *Kelvin* (1860). The conductive layers are the ground and the ionosphere, and the gap is filled by the neutral atmosphere (see Figure 1.6). The ground and the lower ionosphere have approximately the same conductivity, with the ionosphere forming the positively charged plate of the capacitor and the ground is the negatively charged plate. This creates a large potential difference on the order of hundreds of kilovolts. As described by Edgar A. *Bering* et al. (2008), this system discharges on average ~ 1 kiloAmpère all around the Earth, and the primary mechanism for this discharge is lightning in global thunderstorms (E. A. *Bering*, 1995).

1.6.2 Lightning

There are multiple forms of lightning discharges, the most common being cloud-to-ground (CG) and cloud-to-cloud (CC) (the latter one is the most prevalent). Cloud-to-ground flashes result from a rapid multi-step process involving multiple leader, follower, and return strokes that rapidly create and then neutralize a negatively charged channel between a cloud and the ground within 0.2 seconds (*Barr* et al., 2000). This process, which is constantly driven by the global equatorial storm centres, closes the fair weather global electric circuit (referred to as the global electric circuit in the rest of this thesis).

Lightning flashes emit electromagnetic energy over a range of frequencies, primarily in the ultra-low/very-low frequency (ULF/VLF) and low frequency (LF) ranges, with some high current components producing signals in the very high frequency (VHF) range (see figure 1.7). Modern lightning location
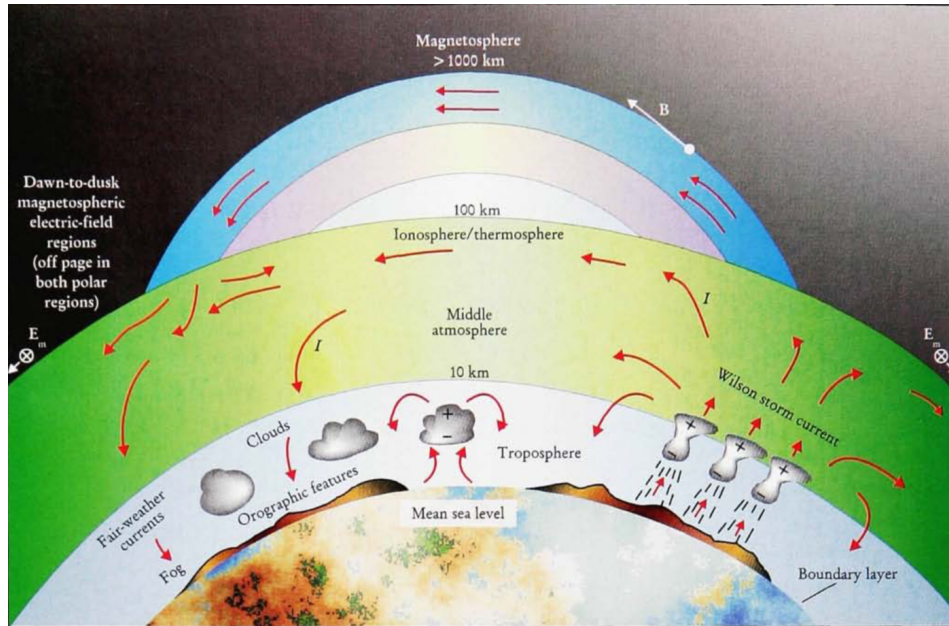
Figure 1.6: An illustration of the fair weather global electric circuit, showing the flow of currents between storm centres in the atmosphere and the ionosphere (taken from E. A. *Bering*, 1995).

systems use large arrays of electric field instruments deployed over the region of interest (or the whole globe in the case of WWLLN) to determine time of arrival information about lightning strikes. Current systems report detection efficiencies greater than 90% with location errors below 250 metres (*Cummins* et al., 2009).

Global lightning is concentrated in centres near land masses at the equator, particularly in South Africa, Central and South America, and South East Asia, especially as storms on these land masses are powered as they traverse the local afternoon. On average, 2000 storms are consistently in progress around the world at one time, resulting in an average global flash rate of 100 per second.

1.6.3 The Schumann Resonator

The global electric circuit contains resonant modes which are electric modes that encompass the Earth and are trapped in the insulating atmosphere between reflections at the ground and from the D-region ionosphere, called the Schumann resonances (SR) (*Schumann*, 1952). The Schumann resonances are
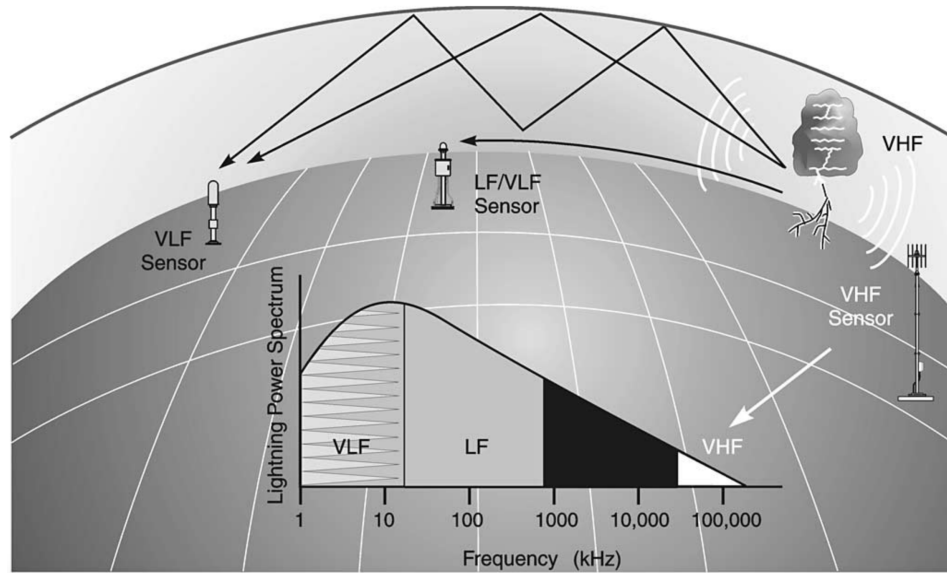
Figure 1.7: An illustration of different instruments used for lightning location and a plot of the distribution of energy from lightning in the different frequency ranges (taken from *Cummins* et al., 2009). Note, these ranges use the radio spectrum definitions, in magnetosphere science ultra-low frequency (ULF) ranges from approximately mHz to 10 Hz.

excited by global lightning, therefore they are constantly activated. The fundamental frequency of the SR is approximately 7.8 Hz, corresponding to the time for a signal to travel the circumference of the Earth at the speed of light. The presence of the SR is a foundational basis for the topic of this thesis. As will be shown, the Alfvén wave modes trapped in the Ionospheric Alfvén Resonator (IAR) and the Schumann Resonances are closely related as we show for the first time here they are in fact both excited by lightning. Chapter 4 details the discovery reported here that lightning excitation of the IAR provides a new paradigm for interactions between atmospheric weather and space weather.

1.7   Magnetohydrodynamics

Magnetohydrodynamics is the fluid theory for plasmas, which are based on the dynamics of highly conducting ionised plasma fluids and their interaction with magnetic fields. The theory is a close parallel to hydrodynamic theory,

including the use of the Navier-Stokes equation, with the added complexity of calculating the effect of an electromagnetic Lorentz force acting on the charged particles in the plasma. This is accomplished by pairing Maxwell's equations with the Navier-Stokes equation. In order for magnetohydrodynamic theory to hold, the time scale of variations of the plasma fluid and the electric and magnetic fields it interacts with must be longer than the time scale of variation of the heaviest particles in the plasma; ie., the ion cyclotron frequency ω_i. Further, the length scales of the plasma must be larger than the ion gyroradius r_{gi} (e.g., *Baumjohann* et al., 1996).

The topic of this thesis deals specifically with the excitation and propagation of waves through plasmas near Earth. In these hot plasmas, the atoms are ionised, the charged particle dynamics being strongly coupled to the magnetic fields generating collective effects and allowing their treatment as a highly conducting fluid using a magnetohydrodynamic approach. Due to the high temperatures involved, plasma particles are in fast motion and thus give the plasma body a baseline thermal fluctuation level (e.g., *Baumjohann* et al., 1996). Waves in the plasma result from external disturbances that exceed this baseline thermal fluctuation or excite resonances in the plasma that exceed the baseline. These waves must also obey the magnetohydrodynamic equations defining the plasma, thus imposing a discrete set of modes for any wave propagation. Chapter 2 provides an in-depth analysis of the dispersion relations for Alfvén and other magnetohydrodynamic plasma waves in the ionosphere, building the theoretical foundation for the experimental results in Chapters 4 and 5, showing that lightning is an important driver for waves in the coupled atmosphere-ionosphere-magnetosphere system, and in particular for the excitation of ULF Alfvén waves trapped in the ionospheric Alfvén resonator.

Chapter 2

Alfvén and Magnetohydrodynmanic Wave Theory for the IAR

2.1 Magnetohydrodynamic Theory

A plasma is a conducting fluid, therefore it is defined by a combination of electromagnetic equations, specifically Maxwell's equations, and fluid equations. Applied to magnetohydrodynamics, Maxwell's can be simplified and presented as follows:

$$\nabla \times \mathbf{B} = \mu_0 \mathbf{j} \tag{2.1}$$

$$\nabla \cdot \mathbf{B} = 0 \tag{2.2}$$

$$\nabla \cdot \mathbf{E} = 0 \tag{2.3}$$

$$\nabla \times \mathbf{E} = -\frac{\partial \mathbf{B}}{\partial t} \tag{2.4}$$

where the displacement current term in Ampère's law (equation 2.1) can be ignored because the large scale variations of the plasma in time and the characteristic length scale of the plasma are much larger than the variations in the period of the ion gyrofrequency and the length scale of the ion gyroradius. In other words, the plasma is non-relativistic, and it can be shown that the $\frac{1}{c^2}\frac{\partial E}{\partial t}$ term is proportional to $\frac{v^2}{c^2} \ll 1$ (*Kulsrud*, 1980). Additionally, since the plasma is quasi-neutral the charge density ρ is essentially zero, therefore Gauss's law (equation 2.3) is also simplified.

The fluid equations to define a plasma are the continuity equation

$$\frac{\partial n}{\partial t} + \nabla \cdot (n\mathbf{v}) = 0 \qquad (2.5)$$

where n is the number density of charged particles in the plasma, and $\mathbf{v}$ is their velocity; the momentum equation

$$mn\frac{d\mathbf{v}}{dt} = \mathbf{j} \times \mathbf{B} - \nabla P + n\mathbf{F_g} \qquad (2.6)$$

where m is the proton mass, $\mathbf{j} \times \mathbf{B}$ is the Lorentz force term, $-\nabla P$ is the force per unit volume, associated with the pressure gradient, and $n\mathbf{F_g}$ is the gravitational force per unit volume; and the pressure P is determined by the equation of state for an ideal gas

$$P = nkT \qquad (2.7)$$

where k is the Boltzmann constant and T is the temperature of the plasma. Expanding the Lorentz force term by substituting for the $\mathbf{j}$ term with equation (2.1) gives

$$\mathbf{j} \times \mathbf{B} = -\frac{1}{\mu_0}\mathbf{B} \times (\nabla \times \mathbf{B}) \qquad (2.8)$$

which can then be re-written as

$$\mathbf{j} \times \mathbf{B} = -\nabla\left(\frac{B^2}{2\mu_0}\right) + \frac{1}{\mu_0}(\mathbf{B} \cdot \nabla)\mathbf{B} + \frac{1}{\mu_0}(\nabla \cdot \mathbf{B})\mathbf{B}. \qquad (2.9)$$

The first term on the right is the pressure term, where the magnetic pressure is given inside the parentheses. The second term on the right is the divergence of the magnetic stress tensor, which results from the tension and torsion the magnetic field exerts on the plasma. This term provides the restoring force for the oscillations of the Alfvén waves discussed in section 2.2.1 below. The third term is zero due to Gauss's law for magnetism (equation 2.2).

2.2 Magnetohydrodynamic Waves

As shown for example in *Baumjohann* et al. (1996), the magnetohydrodynamic equations can be linearised to establish equations for the linear wave modes in

the magnetohydrodynamic plasma. To provide a brief but appropriate background for the study of Alfvén waves in the ionospheric Alfvén resonator, here we present the details of the dispersion relations for these linear magnetohydrodynamic wave modes in a uniform plasma by assuming plane wave solutions of the complex exponential form

$$U(\mathbf{r}, t) = A_0 e^{i(\mathbf{k} \cdot \mathbf{r} - \omega t)} \tag{2.10}$$

where A_0 is the real valued amplitude, $\mathbf{k}$ is the 3D wave vector:

$$\mathbf{k} = k_x \hat{\mathbf{x}} + k_y \hat{\mathbf{y}} + k_z \hat{\mathbf{z}} \tag{2.11}$$

$\mathbf{r}$ is the position, ω is the angular frequency, and t is time.

This is the basis for defining magnetohydrodynamic wave dispersion in a uniform plasma.

2.2.1 Shear Alfvén Waves

Shear Alfvén waves are similar to simple harmonic oscillations along a string, however in this case the string is a magnetic field line and the restoring force for the propagation of the Alfvén wave is magnetic tension. Shear Alfvén waves propagate parallel to the magnetic field lines with a purely transverse displacement. Setting the background magnetic field B_0 in this case along the $\hat{\mathbf{x}}$ axis, the transverse displacement along $\hat{\mathbf{y}}$ and $\hat{\mathbf{z}}$ perpendicular to the field, we can replace k_x with $k_\parallel$. Then the dispersion relation for Alfvén waves is

$$\omega = \pm k_\parallel V_A \tag{2.12}$$

where ω is the angular frequency of the Alfvén wave, and $k_\parallel$ is the wavenumber along the field line, and V_A is the Alfvén speed. In a plasma with a background mass density ρ_0 and magnetic field strength B_0,

$$V_A^2 = \frac{B_0^2}{\mu_0 n m_i} \tag{2.13}$$

This can also be written as

$$\omega = \pm k \cos(\theta) V_A \tag{2.14}$$

where θ is the angle between the wave vector and the magnetic field. The Alfvén wave mode has a phase speed $\frac{\omega}{k}$ which is maximum at $\theta = 0$. In fact, for $\theta = 0$ both the group and phase velocities equal the Alfvén speed V_A.

The Alfvén speed is a characteristic speed in the solar-terrestrial magnetohydrodynamic system as it represents the propagation speed of Alfvénic disturbances along magnetic field lines. The latter is a fundamental concept in this thesis, the focus of which is the excitation of Alfvén waves along geomagnetic field lines by lightning in the Earth's atmosphere.

2.2.2   Slow and Fast Mode Waves

In the presence of the restoring forces of magnetic and thermal pressure, in addition to magnetic tension, there are two other wave modes which propagate in a magnetohydrodynamic plasma. Two compressional fast and slow magnetoacoustic wave modes develop with the dispersion relation

$$\omega^2 = \frac{k^2}{2} \left\{ c_{ms}^2 \pm \left[\left(V_A^2 - c_s^2 \right)^2 + 4 V_A^2 c_s^2 \frac{k_\perp^2}{k^2} \right]^{1/2} \right\} \tag{2.15}$$

where $c_{ms}^2 = (c_s^2 + V_A^2)$, c_s is the sound speed, and $k_\perp$ is the component of the wave vector perpendicular to the field line. As with the case of Alfvén waves, these magnetoacoustic modes can propagate along the field line. However, they can also propagate perpendicular to the field line as well. For the case where $k = k_\perp$ (i.e., $\theta = 90°$) equation 2.15 can be simplified to

$$\omega^2 = \frac{k^2}{2} \left\{ c_{ms}^2 \pm \left(V_A^2 + c_s^2 \right) \right\} \tag{2.16}$$

however, since $c_{ms}^2 = V_A^2 + c_s^2$ the relation finally simplifies to

$$\omega^2 = \frac{k^2}{2} (c_{ms}^2 \pm c_{ms}^2). \tag{2.17}$$

The positive case is called the *fast mode*, which propagates at c_{ms}, perpendicular to the field line. The negative case is the slow mode, which does not propagate in the perpendicular direction. For $k = k_\parallel$, equation 2.15 simplifies to the relation

$$\omega^2 = \frac{k^2}{2} \left[c_s^2 + V_A^2 \pm \left(c_s^2 - V_A^2 \right) \right]. \tag{2.18}$$

with the fast mode given by the positive relation, the slow mode given by the negative relation.

2.3   Alfvén Wave Reflection

The variations in density within the ionospheric layers identified in section (1.5) above can lead to Alfvén wave reflection and the formation of a resonant cavity known as the ionospheric Alfvén resonator. Under the appropriate conditions, shear Alfvén waves are strongly reflected by the current sheet at the bottom of the cavity, with imperfect reflection at the upper boundary depending on how the Alfvén speed (equation 2.13) varies with altitude (z) along the field line (e.g., R. *Lysak*, 1991)

$$V_A^2(z) = \frac{V_{AI}^2}{\epsilon^2 + e^{\frac{-z}{h}}} \tag{2.19}$$

where V_{AI} is the Alfvén speed just above the assumed thin sheet E-layer, ϵ is the ratio of V_{AI} to the Alfvén speed at the top boundary V_{AM} (e.g., R. *Lysak*, 1991)

$$\epsilon = \frac{V_{AI}}{V_{AM}}, \tag{2.20}$$

and h describes the ionospheric electron density profile (*Ram* et al., 2009). Following the assumption of a thin sheet E-layer (introduced in section 1.5.3), then the boundary condition for incident Alfvén waves can be derived from the height-integrated sheet Pedersen conductance Σ_P. Specifically, at the lower boundary the reflection coefficient is defined as (e.g., R. *Lysak*, 1991)

$$R_L = \frac{\Sigma_{AI} - \Sigma_P}{\Sigma_{AI} + \Sigma_P} \tag{2.21}$$

where

$$\Sigma_{AI} = \frac{c^2}{4\pi V_{AI}} \tag{2.22}$$

At the upper boundary the reflection coefficient is obtained as the ratio A^-/A^+ from the general solution for the upper boundary condition given by (e.g., R. *Lysak*, 1991)

$$A^+[iJ'_{ix_0\epsilon} + \alpha J_{ix_0\epsilon}] + A^-[iJ'_{-ix_0\epsilon} + \alpha J_{-ix_0\epsilon}] = 0 \tag{2.23}$$

where J are Bessel functions evaluated at x_0, $\alpha = \frac{\Sigma_P}{\Sigma_{AI}}$. Therefore,

$$R_U = \frac{A^-}{A^+} = -\frac{iJ'_{ix_0\epsilon} + \alpha J_{ix_0\epsilon}}{iJ'_{-ix_0\epsilon} + \alpha J_{-ix_0\epsilon}} \tag{2.24}$$

For the low frequency limit, this simplifies to (e.g., R. *Lysak*, 1991)

$$R_U = \frac{\Sigma_{AM} - \Sigma_P}{\Sigma_{AM} + \Sigma_P} \tag{2.25}$$

where

$$\Sigma_{AM} = \frac{c^2}{4\pi V_{AM}}. \tag{2.26}$$

When the two conductivities are similar or matched, $R = 0$ and there is little to no reflection. In many cases the Pedersen conductance dominates, so reflection occurs and the reflection coefficient is negative, indicating the incident and reflected electric fields of the Alfvén waves are opposite. In the cases where the Alfvén conductance dominates, reflection occurs and the incident and reflected electric fields of the Alfvén waves are in the same direction (e.g., R. *Lysak*, 1991).

Wave Reflection and Transmission

The transmission and reflection of shear Alfvén waves at these boundaries is akin to waves along a string reaching a boundary where the linear density of the string changes. The relative densities on the string determine how much incidence wave energy is reflected and how much is transmitted. In the case of a traditional cavity with constant excitation, when the reflection condition is met at both boundaries, shear Alfvén waves travelling upward will interfere with ones travelling downward. The frequencies that match the resonance of the cavity will interfere constructively to form standing wave modes, while other frequencies will interfere destructively and be cancelled out. *Hebden* et al. (2005) proposes that half-integer and integer standing wave modes can form in the ionospheric Alfvén resonator cavity, depending on the ionospheric conductivity of the lower boundary, if it is high (node, semi-integer wavelength) or low (antinode, integer wavelength). This is illustrated in Figure (2.1).

However, as will be discussed later, the excitation of the ionospheric Alfvén resonator cavity due to lightning may represent a short impulsive driver resulting in a short pulse entering into, and propagating within, the cavity corresponding to the resonant frequency of the cavity. In this case the travel time between the reflecting boundaries might be much longer than the duration of the pulse. Standing waves do not hence necessarily form as a result of this pulsed excitation.
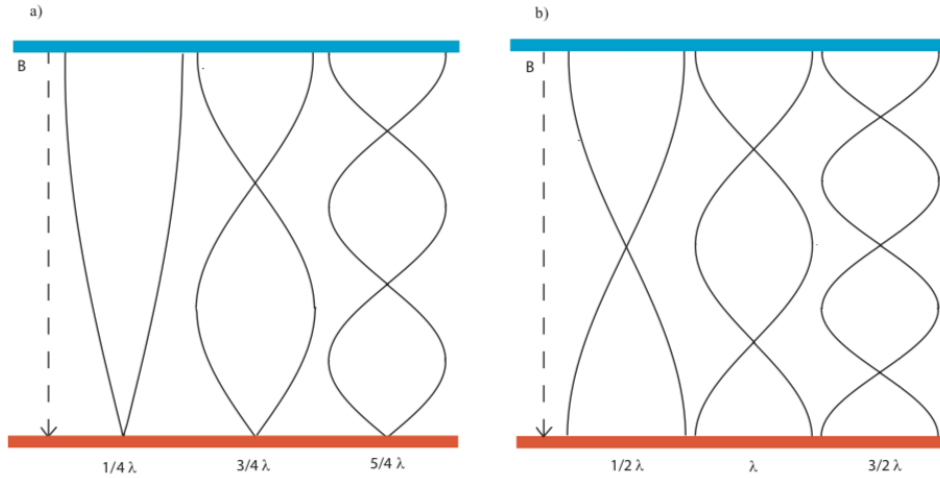
Figure 2.1: Illustration of Alfvén wave modes formed in the IAR cavity. a) demonstrates the case where there is high ionospheric conductivity, thus Pedersen conductivity is large, and this results in a node reflection at the lower boundary. This causes half integer wavelength standing wave modes. b) demonstrates the case where there is low ionospheric conductivity, thus Pedersen conductivity is small, and this results in a antinode reflection at the lower boundary. This causes integer wavelength standing wave modes. The upper boundary forms an antinode due to the lower density of the plasma.) (taken from *Hebden* et al., 2005).

2.4   Ionospheric Alfvén Resonator

Resonances pointing to the existence of cavities in the magnetohydrodynamic environment of the Earth have been a topic of interest for over 50 years (*Field* et al., 1965). The ionospheric Alfvén resonator was first proposed, and its properties first investigated and presented, by *Polyakov* (1976). Since then, the properties of harmonic Alfvén modes trapped inside the ionospheric Alfvén

resonator (often called spectral resonance structures, or SRS - e.g., *Belyaev* et al., 1990) have been documented and analysed in detail, and substantial work has contributed to developing theoretical models of the IAR and its excitation mechanisms (e.g., *Lysak*, 1993, *Knudsen* et al., 1992).

2.4.1 IAR Harmonics

Figure (2.2) - a power spectral density plot of magnetometer data collected August 24, 2009 from the Ministik Lake magnetometer station near Edmonton, Alberta - shows evidence for several discrete harmonic modes in the form of SRS and which are believed to be signatures of the Alfvén modes trapped inside the ionospheric Alfvén resonator. Other relevant phenomena such as the Schumann resonances can also be seen in Figure (2.2). Beginning at 3:00 UTC (Coordinated Universal Time), a series of ~ 10 upward sloping bands coloured yellow to turquoise appear until about 11:00 UTC corresponding to the SRS of the ionospheric Alfvén resonator harmonics. The bands have frequency separations which vary between 1.0 to 2.5 Hz in this interval, following the variation in the frequencies of the fundamental and higher frequency modes as expected if they are signatures of the resonant modes of the ionospheric Alfvén resonator. At 7.8 Hz, 14 Hz, and 20 Hz there are bands spanning the whole 24 hour period. These are the Schumann resonances resulting from global lightning activity resonating in the Earth-Ionosphere waveguide. Finally, note that frequencies below 0.3 Hz are cut off with a high pass filter, which is discussed in detail in Chapter 3.

Section 2.3 describes the formation of standing waves resonating in the ionospheric Alfvén resonator cavity. Each standing wave mode represents a harmonic of the fundamental, and as proposed for the IAR in *Hebden* et al., 2005 (based on previous work by R. *Lysak*, 1991), depending on the presence of a node or anti-node at the lower reflection boundary, these harmonics sit at half-integer or integer intervals above the fundamental. A simplified approximation of this relation is given by

$$f = \frac{(N + \Phi)V_A}{2L} \tag{2.27}$$

23
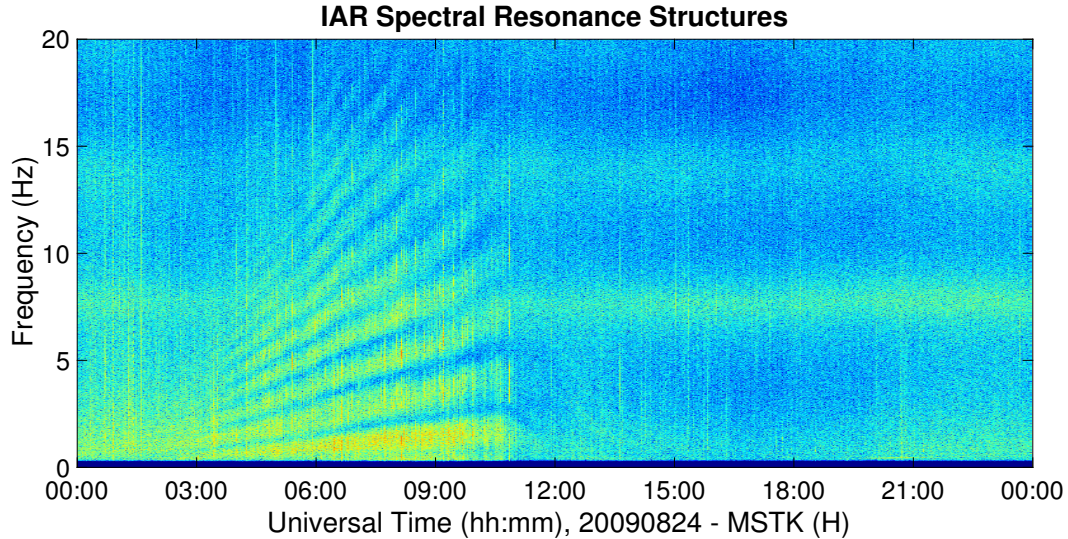
Figure 2.2: Power spectral density plot (arbitrary units) for H (North-South) component induction coil magnetometer data from Ministik Lake on August 24, 2009, exhibiting IAR spectral resonance structures and Schumann Resonances.

(*Hebden* et al., 2005), where f is the harmonic frequency, $N = 0, 1, 2...$ is the harmonic number, L is the length of the IAR cavity, and Φ is the wave "phase factor" defined by the presence of a node ($\Phi = 1$) or anti-node ($\Phi = 0.5$) at the lower boundary.

2.4.2 Excitation of the IAR

The constant presence of the Schumann resonances at fixed frequencies is a result of continuous global lightning activity and the constant geometry of the Earth-Ionosphere waveguide. The ionospheric Alfvén resonator, however, is not continuously observed in the form of the SRS in ground-based magnetometer data. Though it does occur frequently and exhibits variations linked to the diurnal cycle, seasons, and the eleven year cycle of solar activity (*Belyaev* et al., 2000, *Yahnin* et al., 2003). Two hypotheses have been suggested as the most likely cause for Alfvén wave excitation in the ionospheric Alfvén resonator - excitation from above by magnetospheric sources such as incident Alfvén waves or ion cyclotron instabilities (R. *Lysak*, 1991, *Trakhtengerts* et al., 1991) and/or excitation from below by atmospheric lightning (*Belyaev* et al.,

1990, *Bösinger* et al., 2002, *Schekotov* et al., 2011).

Significant research has been conducted and extensive theoretical models developed to investigate the role of atmospheric lightning as an excitation mechanism of the ionospheric Alfvén resonator (*Belyaev* et al., 1990, *Fedorov* et al., 2006, *Surkov* et al., 2006, *Fedorov* et al., 2014). However, due partly to restricted access to lightning datasets, thorough experimental analysis to verify the proposed theoretical connection to excitation by lightning have not been conducted. This thesis presents that analysis, using multi-point measurements from the CARISMA magnetometer array (e.g., *Mann* et al., 2008) and WWLLN (e.g., *Hutchins* et al., 2012) that shows a statistically significant correlation to support the excitation of the ionospheric Alfvén resonator caused by lightning strikes. The results presented in Chapters 4 and 5 further demonstrate that the structure of the modes excited inside the ionospheric Alfvén resonator are governed by local conditions of the ionospheric Alfvén resonator cavity. Furthermore, the results demonstrate that lightning pulses which are far away from the local ionospheric Alfvén resonator cavity can still excite modes there by ducting through the Earth-Ionosphere waveguide. Even at very large distances, e.g. thousands of kilometers, electromagnetic pulses excited in the Earth-ionosphere waveguide can continuously excite Alfvén waves up the field lines and into the ionospheric Alfvén resonator cavity. Overall, this reveals that lightning pulses can continuously leak energy into the ionospheric Alfvén resonator, and potentially all the way into the magnetosphere when wave reflection from the top of the ionosphere is weak, in addition to continuously driving the well-known Schumann resonances. This shows that the global electric circuit, in which lightning strikes act as short circuits to transfer charge across the insulating layer of the atmosphere, couples into the ionosphere because the energy released by the lightning strikes propagate and excite the Alfvén waves that cross the conductive lower boundary in the E-layer to excite the ionospheric Alfvén resonator.

Chapter 3

Data and Methodology

3.1 Overview

Investigating the hypothesis that lightning can be responsible for the spectral resonance structures (SRS) that are characteristics of waves propagating in the ionospheric Alfvén resonator (IAR) was the overall goal of this thesis. This was achieved by identifying and isolating the signature of lightning strikes and the subsequent echoes of the Alfvén waves from the top boundary of the IAR. Two types of datasets were used in the analysis: magnetic field data collected by induction coil magnetometers in the Canadian Array for Real-time Investigations of Magnetic Activity (CARISMA; http://www.carisma.ca/; *Mann* et al., 2008), and lightning data from the World Wide Lightning Location Network (WWLLN; http://wwlln.net/; *Hutchins* et al., 2012). The two datasets were analysed in MATLAB, making use of the *datetime* variable identity for accurate matching of the two time series. The magnetometer data required filtering to facilitate identification of the lightning magnetic signature in the time domain. Finally, the Fast Fourier Transform function was used to analyse the spectra of these responses. Once the signatures were isolated, superposed epoch analysis was applied to determine the statistical significance of the unique features of the pulse-echo signals associated with wave propagation, reflection, and trapping inside the IAR.

3.2 Data

3.2.1 CARISMA

Magnetic field data from induction coil magnetometers (ICM) in the CARISMA network was used in this analysis. CARISMA currently consists of 9 induction coil magnetometers at locations ranging from near Dawson City in Yukon, to near Thief River Falls in Minnesota, USA. Data from 7/9 stations was analysed, with most analysis conducted on data collected at the Ministik Lake station in Alberta.

Induction coil magnetometers detect magnetic fields using the inductive response of a coil with a large number of turns wrapped around a core with high permeability. Fluctuations of the Earth's magnetic field along the winding axis of the coil result in an induced voltage, as defined by Faraday's law. The relationship of the measured voltage to the magnetic field fluctuations is expressed as (e.g., *Frandsen* et al., 1969; http://carisma.ca/backgrounder/carisma-induction-coils):

$$V = -\mu_r \cdot n_c \cdot A \cdot \frac{dB}{dt} \tag{3.1}$$

where V is the voltage, μ_r is the relative permeability of the core, n_c is the number of turns in the coil, A is the cross sectional area of the coil and $\frac{dB}{dt}$ is the changing magnetic field. A single ICM can only measure fluctuations in one dimension, thus each CARISMA ICM station is equipped with two induction coil magnetometers aligned orthogonally in the horizontal plane each measuring the magnetic North/South (H component) and East/West (D component), respectively. Measurements are taken at 100 samples/second, time tagged by GPS timing. Detailed specifications are given in table (3.1)

The data is organized by date into 1-hour files (24 files for each day), and each CARISMA ICM file contains the following information/data:

- 4-letter site identification label

- Latitude and longitude of the site

- Date and time in Coordinated Universal Time (UTC)

27

Frequency band of measured signals	0.001 - 30 Hz
Transformation factor	
Below 1 Hz	20 * freq.mV/nT
Above 1 Hz	20 mV/nT
Magnetic noise level at:	
0.01 Hz	$\leq$20 pT$\sqrt{Hz}$
0.1 Hz	$\leq$2 pT$\sqrt{Hz}$
1 Hz	$\leq$0.2 pT$\sqrt{Hz}$
10 Hz	$\leq$0.04 pT$\sqrt{Hz}$
Noise rejection on (60 ± 0.2) Hz	>60 dB
Outer dimensions	Length 870 mm
	Diameter: 85 mm
Weight	5.6 kg

Table 3.1: Specifications of the CARISMA induction coils (taken from http://carisma.ca/backgrounder/carisma-induction-coils).

- H-component coil data

- D-component coil data

- Unit (pT)

- Sampling frequency

3.2.2 WWLLN

Global lightning location data from WWLLN was also used in this analysis. As of 2012 WWLLN contained 60 measurement stations across the globe. These stations use VLF radio wave receivers to identify the time of group arrival (TOGA) for the electromagnetic wave packets associated with individual lightning strikes. Measurements from multiple stations are processed to identify the source location and time (*Hutchins* et al., 2012).

The data is organized by date into 1-day .mat files and each file contains the following information/data:

- Date and time in UTC

- Latitude and longitude of the strike

- A time residual fit error in microseconds for the time of group arrival (TOGA) data, which indicates the quality of the fit to the data (*Abreu et al.*, 2010)

- Number of WWLLN stations which detected the stroke

- RMS energy in joules from 7-18 kHz at 1.3 ms sample time

- Energy uncertainty in joules

- Subset of number of stations within the range 1000-8000 km from the stroke to give a power estimate

More details about WWLLN are available in Appendix A.

3.2.3 Data Processing

MATLAB is a very powerful tool for manipulating and visualising datasets and it was used to analyse the magnetometer time series data. For the lightning data, the interest was in the time that the strikes occurred, their location, and their energy, and this was used to order the magnetometer data which detected both the initial lightning strike as well as reflections and signals arising from the effect of the IAR.

Filtering

The CARISMA induction coil magnetometers can measure fluctuations down to frequencies of $\sim$0.1 Hz. The signals relevant to reflections inside the IAR are in the 0.1 Hz-20 Hz range, are typically bipolar, and in many cases are only slightly larger in amplitude than the background RMS (root mean square) noise. Removing low frequency signals simplifies the identification of lightning related IAR excitation signatures since a threshold (the RMS level during a quiet period of the day, see section 3.3.2) can be set in the filtered data, removing effects of lowest frequency noise.

In addition, on certain days, or for certain induction coil magnetometers, unwanted tones from the background environment can exist in the data at

higher frequencies, for example a 20 Hz tone across the entire day. In these situations it is also necessary to remove the tone.

A two step process using the MATLAB functions *fir1* and *filtfilt* was implemented to remove the low frequency noise, and when necessary remove unwanted tones at higher frequencies in the data. *fir1* generates filter coefficients using the finite impulse response method with a windowed filter design, which are then input to *filtfilt* with the data to be filtered, generating the filtered output. *fir1* takes as inputs the desired filter order, N_{order}, a character string to select a high-pass or low pass filter, the pass frequency, and a window of length N_{order}+1 to window the impulse response. Following some trial and error, a filter order of N_{order}=2000 (20 times the sampling frequency of 100 sps) was selected to remove the frequencies below 0.3 Hz (the pass frequency), with the character string set to 'high' for high-pass filtering. Alternatively, when working with down-sampled 20 samples per second data, an order of N_{order}=200 was sufficient. In the case a tone needed to be removed, the pass frequency was set as a vector of two values, the high-pass frequency (0.3 Hz) and the low-pass frequency (e.g., 20 Hz), with the character string left empty. This applied a band-pass filter. For the analysis presented here a Hanning window of length N_{order}+1 was also used.

An important consideration in the spectral analysis of discrete time series data is the Nyquist sampling theorem. Though the induction coil magnetometers sample at 100 samples per second, due to the conversion of analog signals to digital, the maximum frequency that can be reproduced is half the sampling frequency, in this case 50 Hz, and this is called the Nyquist frequency. The MATLAB *fir1* takes the pass frequencies as a fraction of the Nyquist frequency (the values must be between 0 and 1, where 1 corresponds to the Nyquist frequency). Therefore, when setting the high and low pass frequencies, the values must be corrected by dividing the intended pass frequency (e.g., 0.3 Hz) by the Nyquist frequency (e.g., 50 Hz for 100 sample per second data).

Once the coefficients have been generated, they can be input together with the ICM dataset into the *filtfilt* function, which implements a zero-phase forward and reverse digital infinite impulse response (IIR) filter.

Datetime Arrays

The time arrays for the induction coil magnetometer data and the lightning data are natively imported as character strings and as double-precision floating point, respectively. The MATLAB *datetime* function was used to create standardized data vectors in which each element carries the full time information of each data point: date, time, and timezone. This enables standard operations to be applied between the datasets and simplifies the plotting process for time series data. Section 3.3 explains the steps used to match events in time between the magnetometer and lightning datasets, and this requires operations on the time series vectors.

Power Spectral Density Plots and Fast Fourier Transforms

Power spectral density plots are an effective tool to visualize the changing frequency dependence of the magnetic field, as measured by the induction coil magnetometers. Figure 2.2 gives an example showing the variation measured over 24 hours, revealing the Schumann resonances and the spectral resonance structures of the ionospheric Alfvén resonator. It is generated by taking the Fourier transform of small windows of the full dataset, with each window overlapping a set number of data points, then producing a graph of frequency (Hz) in the y axis versus time in the x axis, with the Fourier spectra amplitude represented with a chosen colour scale.

The MATLAB *spectrogram* function takes as input the time series magnetometer data, a window function of length N_{PSD} points, the number of points of overlap, the window length N_{PSD}, and the sample frequency. In this analysis, the magnetometer data vector was the 24 hour H-component or D-component magnetic field data, a Hanning window was used, the overlap was set as 30% of the window length N_{PSD}, the window length N_{PSD} was set to 2^{12} points for 20 sample per second data, or 2^{14} points for 100 sample per second data. The outputs are an array containing the spectral data, a frequency vector and a time vector. However, the time vector is relative, therefore a new time vector was generated by identifying the midpoint of each spectral window

in the *datetime* vector discussed in section 3.2.3.

The MATLAB *fft* function was used to compute the discrete Fourier transform of the individual or superposed (see section 3.4 below) pulse-echo signatures matched to the times of lightning. Taking the Fourier transform of these signals generates their spectra, which are used to verify the presence of, and correlation to the spectral resonance structures that are characteristic of IAR excitation. Note, in all FFT plots, the vertical axis is in arbitrary units.

3.3   Event Selection Criteria

Two criteria were established to identify the pulse-echo signatures characteristic of waves inside the IAR cavity in the induction coil magnetometer data, and match them to lightning strikes. The first is a minimum absolute amplitude threshold for the initial lightning strike associated pulse. The second is a causal time delay between the occurrence of a lightning strike in one location and the lightning associated pulse measured remotely some distance away at the induction coil magnetometer station. Additionally, a system was implemented to reject the cases where multiple events matched the criteria within the same superposed time interval, to remove features associated with multiple strikes and to ensure a superposition of the signatures of isolated strikes.

3.3.1   Lightning Distance Limit

In order to reduce processing time, as well as study the effect of distance between the lightning strike and the magnetometer which measured the related magnetic pulse, the code pre-selects within each time interval only lightning that occurs within a user defined distance away from the magnetometer station. Chapter 4 presents cases for lightning within 2000 km of the magnetometer stations chosen. Chapter 5 explores the effect of lightning occurring across a range of distances from 0 km to 10,000 km away from the magnetometer station.

3.3.2 Magnetic Amplitude Threshold

The root mean squared (RMS) value of the induction coil magnetometer data in a defined time period of data was selected as the base-like threshold to compute amplitudes of lightning and IAR related pulses in the time domain. Taking the RMS of the full 24 hour dataset was deemed inappropriate due to event driven variations in intensity (e.g., arising from the IAR SRS itself). Instead a function calculates the RMS value for shorter individual time intervals in the 24 hour period. The time intervals are user configurable, however all results presented in this thesis used 24 1-hour intervals. The lowest RMS value in any 1-hour bin is chosen as the *quiet time RMS* for that 24-hour dataset, denoted as σ_{quiet} throughout the next 2 chapters and their accompanying appendices.

The σ_{quiet} value is input into the MATLAB *findpeaks* function, together with the vector of the time series of the magnitude of the magnetometer data, $|B|$. The output is a vector of all values with magnitudes above the σ_{quiet} level together with their element location, which is used to pair the values with the time they occurred. These are the magnetic pulses subsequently analysed and which are associated with lightning strikes.

It is still valuable to vary the threshold level to identify and analyse signals that have a higher signal-to-noise ratio. This was accomplished by selecting different quantiles of all the magnetic pulses with the MATLAB *quantile* function. The top panel of Figure 3.1 demonstrates an example of the variation in number of magnetic pulses in each 1-hour interval, from all the magnetic pulses greater than σ_{quiet} (N~50,000) to the largest 10% of the magnetic pulses (N~5,000). The lowest threshold σ_{quiet}, results in the greatest number of magnetic pulse events identified. As the quantile value above σ_{quiet} is increased, the threshold increases accordingly and the number of selected magnetic pulses drops. The 0.9 quantile results in 1/10 the number of magnetic pulses; in other words only the top 10% largest magnetic pulses are retained. The bottom panel of Figure 3.1 then demonstrates the effect when the magnetic pulses for a given threshold are matched to the lightning strikes occurring within a certain dis-

tance of the magnetometer (in this case 0-2000 km). The number of matched cases will vary as a result of the different thresholds. In the case shown here, numbers increase with increased threshold (quantiles 0.1-0.7) because fewer magnetic pulses above the threshold results in fewer rejections due to multiple strikes in a given window for the same number of lightning strikes (see section 3.3.4). However, beyond quantile 0.8 the numbers drop as expected.
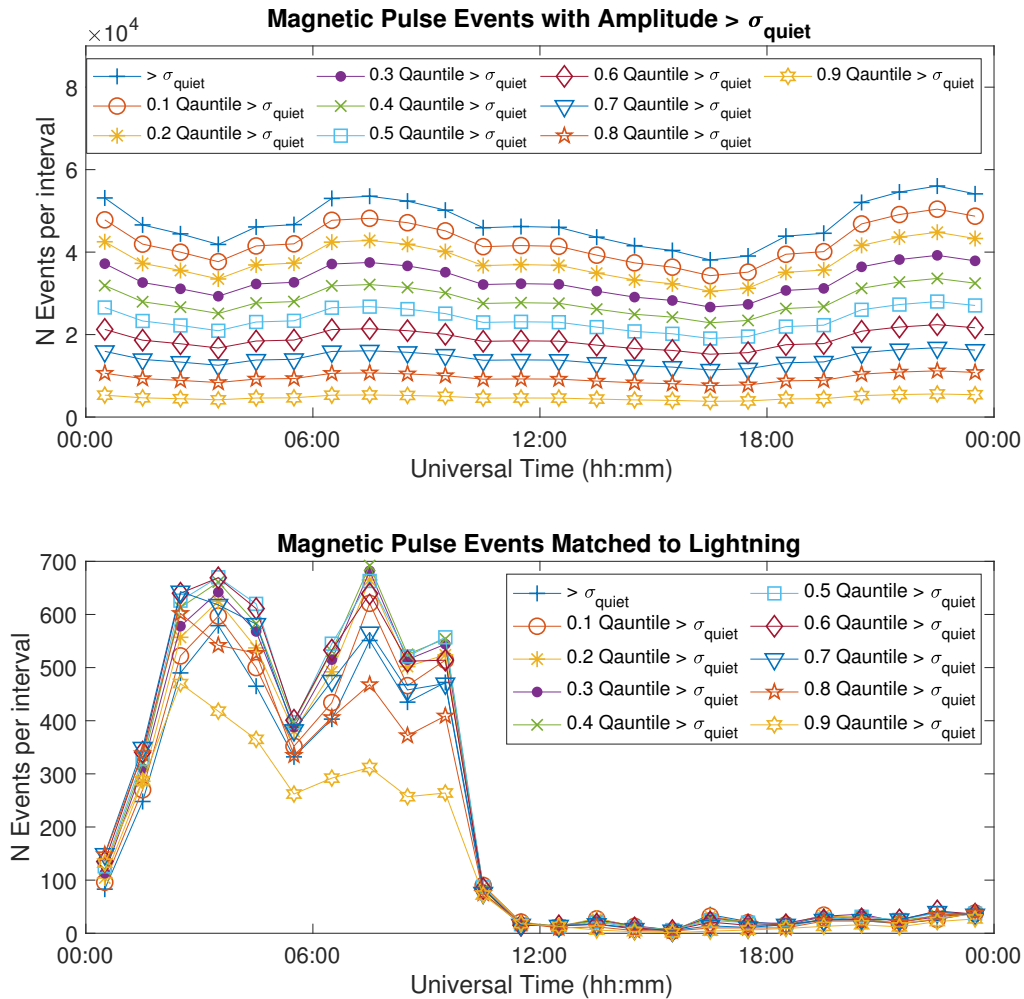
Figure 3.1: The effect of setting different thresholds for magnetic pulse selection. (Top) The number of magnetic pulse events identified above each quantile threshold from 0-0.9. (Bottom) The number magnetic pulses matched to lightning strikes for different quantile threshold from 0-0.9. See text for more details.

3.3.3 Timed Matching to Lightning

A vector of lightning strike occurrence times (from WWLLN) and magnetic pulse times (from the analysis of CARISMA data) has been created for each time interval. Taking the vector subtraction of the time of the magnetic pulses from the time of the lightning strike occurrences from WWLLN generates a matrix of propagation times between the i'th lightning strike time t_{l_i} and the j'th magnetic pulse time t_{B_j}. To maintain causality, all negative propagation times (i.e., $t_{propagation_{ij}} = t_{B_j} - t_{l_i} < 0$) are rejected, as these are the values for magnetic pulses occurring before the causative lightning strikes. For clarity, it is just that combination of lightning strike time t_{l_i} and magnetic pulse time t_{B_j} that is rejected. The same lightning strike time t_{l_i} generates causal $t_{propagation}$ with other magnetic pulse times, and likewise for the magnetic pulse time t_{B_j} with other lightning strike times. Next, the MATLAB *arclen* and *km2deg* functions are used to calculate the distance of each strike location (from WWLLN) from the location of the magnetometer station. Using the speed of light, $c = 300,000$ km·s^{-1}, a vector of distance dependent minimum propagation times $t_{min}(d)$ is specified for each lightning strike. The upper limit for propagation time, t_{max}, is user-defined. However results presented in Chapter 5 show that the typical matching propagation time, $t_{propagation}$, ranges from 0.04 seconds to 0.06 seconds. Thus, 0.1 seconds was usually chosen as the upper limit for propagation from the strike to the time it is identified as the peak of the magnetic pulse in the magnetometer data.

Matched cases are those where the propagation time $t_{min}(d) < t_{propagation} < t_{max}$. Figure 3.2 demonstrates these timing criteria. The threshold is set as the minimum, $\sigma_{quiet} \sim 2$ pT, and the maximum propagation time, $t_{max} = 0.1$ s. The lightning strike for this event occurs at 00:08:05.6674 UT, at 943.988 km from the Ministik Lake magnetometer station. Therefore, the minimum propagation time is $t_{min} = 0.0031$ s. Four magnetic pulses above σ_{quiet} occur after the strike. The first occurs at 00:08:05.67, only 0.0026 s after the strike. This is too fast, therefore this lightning strike event is rejected from the analysis. Had the magnetic pulse threshold been higher than the amplitude of the first

magnetic pulse observed, only the next three magnetic pulses would have been considered. But the event would still be rejected because there are multiple valid magnetic pulses above the threshold in the window. Only with the magnetic pulse threshold set higher than all but the second magnetic pulse, with amplitude $|B| = 30.8173$ pT, or a lower t_{max}, would this event then have been included in the analysis. This section of the code has room for improvement in future work, as there are cases where the value of the magnetic pulse matched to the strike is above the noise threshold, but only just, and that magnetic pulse value happens too soon after the lightning strike, but another magnetic pulse, much higher above the threshold and a few data points later such that it occurs within the time constraint, is ignored because the lightning strike is rejected. Thus, the number of matched cases in the current version of the code is conservative.
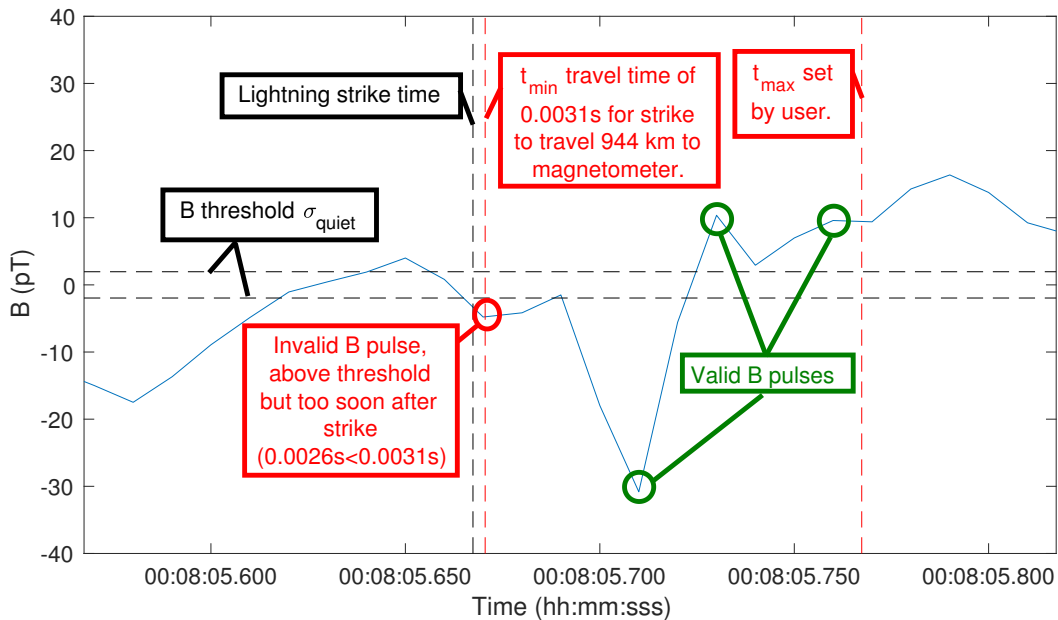
Figure 3.2: An example of the thresholds and timing criteria for selecting magnetic pulses in the magnetometer data and matching them to a lightning strike. See text for more details.

3.3.4 Rejection Due to Multiple Matches

Due to the large number of magnetic pulses and lightning strikes, it is possible for multiple $t_{propagation}$ between different pulses and strikes to overlap. In some cases, one strike has valid $t_{propagation}$ with multiple magnetic pulses - which is the case in Figure 3.2 - and vice versa. All such cases are rejected from the analysis as this prevents, for example, multiple lightning strikes matching to a sequence of magnetic pulses occurring within a few samples of each other. In which case the superposition of multiple signals could artificially amplify or attenuate the resulting response in the magnetic field data. The downside is that some valid events can also be rejected, such as the first valid magnetic pulse in Figure 3.2 and this reduces the statistics of the superposed epoch analysis. The impact on the statistics of these rejections also depends on the size of the chosen threshold. At the lowest threshold the large number of magnetic pulses increases the number of rejected cases. This is shown in the lower panel of Figure 3.1, where all but the two highest thresholds produce greater numbers of matches than the lowest threshold (represented by the symbol -+-).

3.4 Superposed Epoch Analysis

The purpose of the superposed epoch analysis is to identify whether, in a large number of independent signal events, there are common characteristics that appear in the ensemble. The mean, median, and quartiles of the superposed signals reveal these characteristics and give an indication of their significance.

Thus far, the data treatment has identified a number, say N, of magnetic pulse data points each matched to a single lightning strike in each user-defined time interval of the 24 hour induction coil magnetometer dataset. The fundamental frequency of the IAR is in the range 0.5 Hz to 1.5 Hz, therefore the pulse-echo signal associated with the spectral resonance structures of the IAR occur on a time scale of ∼1-2 seconds. In this analysis, the time span of the superposed epoch window is user-defined as a value in seconds. The code then pulls 20% of the points in the superposed window from before the

matched magnetic pulse point, and the remaining 80% from after the point of the peak of the magnetic pulse (this ratio is also easily modifiable). For example, if the superposed window is set to 4 seconds, with 100 sample per second data that generates a window of 400 data points for each event. 0.2*400 = 80 points/100 points/second = 0.8 seconds of time which precedes the matched magnetic pulse, and the remaining 320 points (3.2 seconds) following the magnetic pulse. Then a N x 400 matrix is generated for each time interval. The mean, median, and quartiles of each column are calculated using the MATLAB *mean* and *quantile* functions. These form new 400 point (4 second) signals, superposed using the time of the peak of the magnetic pulse of each event.

3.4.1   Signal Polarity

The signatures of the pulse and the subsequent echo for the IAR can vary in polarity for not yet fully explored reasons (see future work in Chapter 6). As mentioned in section 3.3.2, both are identified in the matching step in event selection by taking the absolute value of the magnetometer data. However, the polarity has a substantial impact on the superposed epoch analysis. Thus, the code was developed to allow the user to select to superpose the matched signals as is, with their original polarity, or to multiply by -1 all the data points in superposed windows (e.g. 4 seconds, 400 points per window) with initial negative polarity magnetic pulses, thereby inverting the polarity of the negative windows so that all initial pulses were superposed with the same polarity. Figures 3.3 and 3.4 give an example to illustrate the impact of the signal polarity. The top panel of figure (3.3) breaks down the number of matched initial magnetic pulses (red) into those with a positive (brown) and negative polarity (cyan). The result is similar numbers of each polarity type.

The bottom left panel of Figure (3.3) shows that for 9-10 UT, 107 magnetic pulses have a positive polarity, 79 have negative polarity. The mean superposed epoch analysis signature of that 1-hour interval for the original polarity, mixing positive and negative, is shown in blue, and that from reversing the polarity of the initial negative magnetic pulse events to make them positive is shown in red. The blue signal reveals the pulse-echo signature, however it has a lower
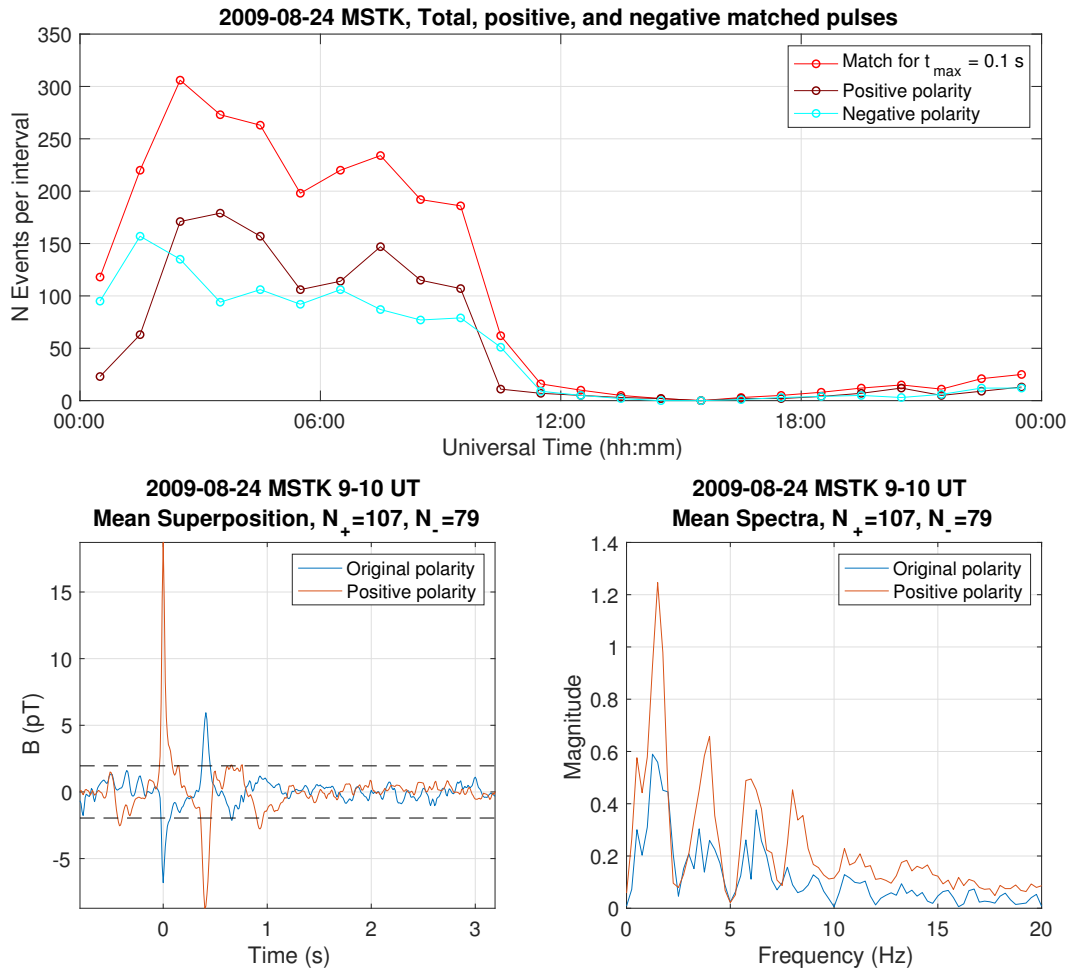
Figure 3.3: An example of the effect of signal polarity on mean superposed epoch analysis from August 24, 2009. See text for more details. (Top) The number of matched initial magnetic pulses (red) that are positive (brown) and negative polarity (cyan). (Bottom left) The mean superposed epoch analysis of 186 magnetic pulses with their original polarity (blue) and with all initial magnetic pulses having a positive polarity (red). (Bottom right) The spectra of the enforced positive polarity (red) cases is stronger and sharper than that derived using the original polarity (blue).

amplitude than the red, resulting from the interference of positive and negative values in the superposition. The same analysis with the negative magnetic pulses (including all the datapoints in each 4 second window) multiplied by -1 (red) such that the polarity of the first magnetic pulse of all 186 events is positive reveals much more clearly the pulse-echo signature. This is further

reinforced by observing the median and quartiles of the superposed signatures in the top left panel of Figure (3.4), where the 0.25 quartile (blue), median (red), and 0.75 quartile (yellow) signatures are shown. Notably, in the top left panel of Figure (3.4) the echo signal is only strongly visible in the 0.75 quartile (yellow). This result is the same for its accompanying spectra in the top right panel of Figure (3.4). Conversely, the analysis with positive polarity for all the first pulses in each event reveals one signature in all three curves, as shown in the bottom left panel of Figure (3.4) and its accompanying spectra in the bottom right panel.However, this does demonstrate that for this time interval, initial negative polarity magnetic pulses dominate, despite there being fewer of them, and thus they must have greater amplitudes. On the other hand, the red signal where all polarities of the initial pulse are positive has a much larger magnitude, revealing the signatures of the pulse and the echo from inside the IAR. This is made very clear in the bottom left panel of Figure (3.4), where now the median and both quartiles all show the same pulse-echo characteristic.

The lower panels on the right of Figure 3.3 and 3.4 show the spectra of the mean superposed signals, and the median and quartiles respectively. Just as superposing the signals onto a common initial magnetic polarity improves the signal in the time domain, it also increases and better resolves the spectral resonance structures in the frequency domain as well.

3.4.2   Quiet Period Schumann Resonances

The Schumann resonances, with fundamental frequency ∼7.8 Hz and harmonics at ∼14 Hz, ∼21 Hz, and so on, are driven by global lightning activity (E. A. *Bering*, 1995). The signal shown in Figure 3.5 shows the result of superposed epoch analysis on magnetic pulse events during periods of low activity in the induction coil magnetometer data, when the IAR is not active. 323 magnetic pulse events matched to lightning strikes at distances between 0-10,000 km away from the Ministik Lake magnetometer station were superposed. The mean SEA reveals a clear sinusoidal wave packet shown in the top left panel of Figure 3.5 with spectra matching the expected ∼7.8 Hz fundamental frequency and subsequent ∼14 Hz and ∼21 Hz harmonics of the Schumann resonances,
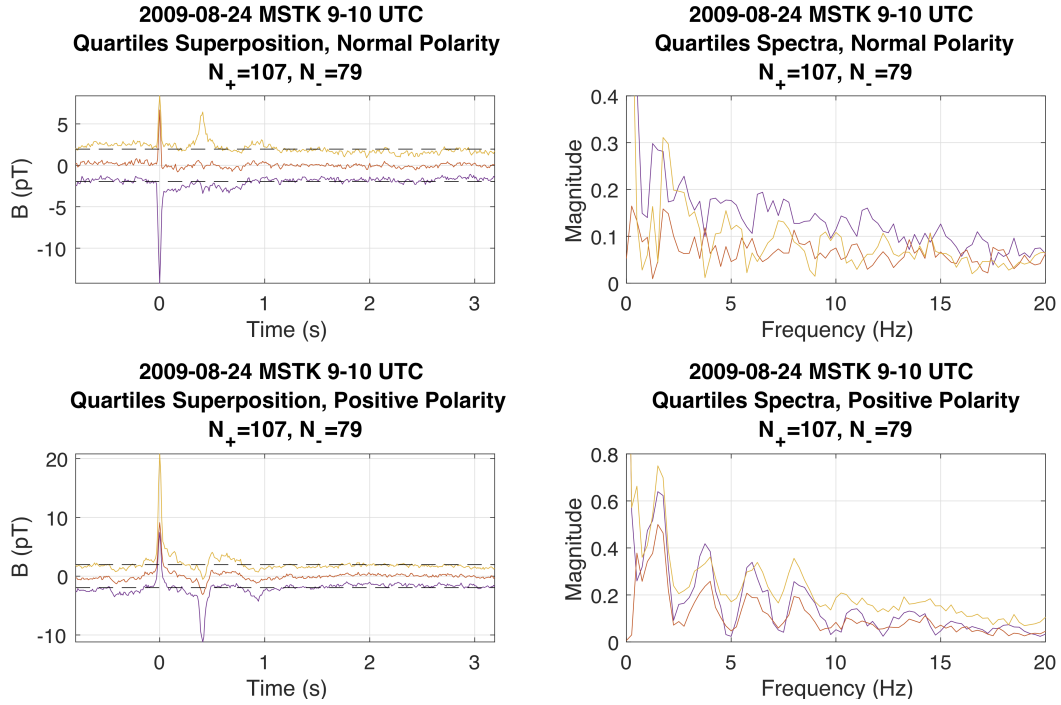
Figure 3.4: An example of the effect of signal polarity on median and quartiles superposed epoch analysis on August 24, 2009. See text for more details. (Top left) The 0.25 quartile (blue), median (red), and 0.75 quartile (yellow) superposed epoch analysis for 186 magnetic pulses with their original polarity maintained. (Top right) Accompanying spectra to the quartile SEA time series signatures. (Bottom left) The same analysis with the polarities of the initial pulse all changed to positive. (Bottom right) The spectra associated to the superposed time series in the bottom left clearly show the SRS of the IAR in the data for all three quartiles.

as shown in the top right panel. The median and quartiles of the superposed epoch analysis in the bottom left panel and the accompanying spectra in the bottom right panel very clearly show the expected Schumann resonance harmonics. All magnetic pulses were superposed with the same positive polarity and the magnetic threshold was chosen as σ_{quiet}. The superposition returns a signal confined to approximately 0.5 seconds either side of the initial strike-related pulse superposed epoch time (0 seconds). The spectra confirm this signal is the time domain characteristic of the Schumann resonances. Knowing this aids in interpreting the pulse-echo signal of the IAR, as the Schumann characteristics are always present and could otherwise be mistaken for echoes.
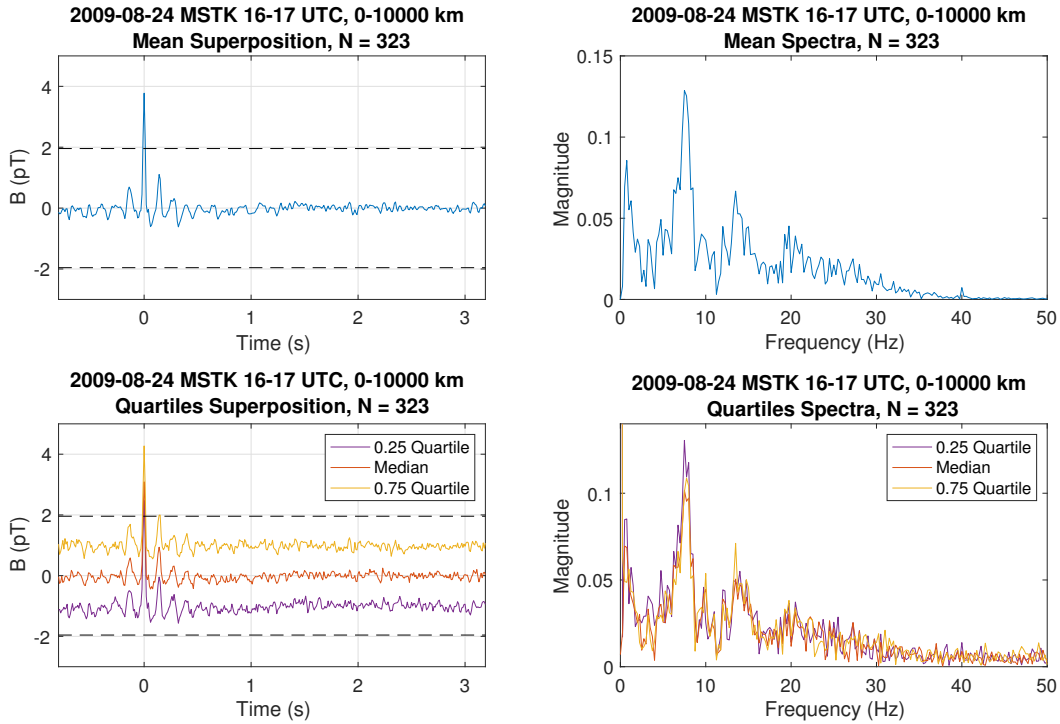
Figure 3.5: Example of superposed epoch analysis for August 24, 2009 clearly revealing the Schumann resonance signals in the magnetometer data during periods when the IAR is inactive. See text for more details. (Top left) The mean superposed epoch analysis of 323 magnetic pulse events matched to lightning strikes at distances between 0-10,000 km away from the Ministik Lake magnetometer station. (Top right) Accompanying spectra matching the expected ∼7.8 Hz fundamental frequency and subsequent ∼14 Hz and ∼21 Hz harmonics of the Schumann resonances. (Bottom left) The median and quartiles of the superposed epoch analysis. (Bottom right) Accompanying spectra showing the Schumann resonance harmonics.

3.5 Universal and Local Time Characteristics of the IAR SRS

Figure 4.4 in Chapter 4 and Figure 4.5 in Appendix B demonstrate that the characteristics of the waves trapped in the IAR, and therefore likely the local Alfvén speed conditions inside the IAR cavity, differs from one magnetometer station to the next. These variations highlight the dominant impact of the local ionospheric conditions and IAR on the measured signal. The data plotted in Figure (4.4) and Figure (4.5) comes from two separate analyses of the magnetometer data. The first source is generated using a function that

down samples the spectral density plot by averaging across data points in the vertical and horizontal axes to produce a smoothed spectral density plot. The peaks of the smoothed curves are then identified using the MATLAB *findpeaks* function and then plotted as points that highlight the brightest characteristics. This facilitates plotting a fit of the variation of frequencies of the harmonics of the SRS as a function of time. The second source are the peaks of the FFT spectra derived from the superposed epoch analysis time series at different time intervals. These were recorded manually by selecting the peaks in the FFT with MATLAB due to time constraints but could easily be identified using the MATLAB *findpeaks* function as well. For example, the peaks of the mean spectra in the panels of the right hand column of Figure (4.2) are plotted with diamond markers in the top panel of Figure (4.4).

3.6   Occurrence Density Plot

The superposed epoch analysis of the events where the lightning strike is matched to a magnetic pulse clearly revealed the pulse-echo signal characteristic of reflection inside the IAR cavity in the magnetometer data. There are many other characteristics of that matched dataset worth exploring, for example the propagation time of a lightning strike to a matched initial magnetic pulse, and the distance between the strike and the matched magnetic pulse allowing an assessment of the propagation of the EM signal from the strike to the initial magnetic pulse at the magnetometer location. The MATLAB *histogram* function generates a histogram that can reveal trends in multiple individual vectors. Running *histogram* on the vector of propagation times revealed a peak in the range 0.04 seconds to 0.06 seconds, and the histogram of the matched distances reveals multiple peaks that correlate to storm centres at different distances from the magnetometer station.

By combining these two vectors into a scatter plot and identifying the regions with the highest density of points can reveal more complex trends in propagation. The MATLAB function *dscatter* (this function is not originally in the standard MATLAB toolbox, but can be downloaded online and is based

on work by *Eilers* et al., 2004) creates histograms of two vectors, for example the matched propagation time and the distance between the matched strikes and the magnetometer station. The histograms are then accumulated and smoothed together to create a matrix of values representing the density of points in each axis, with higher values representing occurrence density. The index of each number in the matrix relates back to its position in the X axis (e.g. propagation time) and Y axis (e.g. distance). A linear indexing function is used to create an index vector from which a colour vector is produced. The three vectors, X, Y, and colour can then be plotted as scatter plot, contour plot, or surface plot used to analyse the statistical details of the relationship between the proximity of the strikes and the time of propagation to the magnetometer.

The MATLAB *max* function can be used to identify the peak occurrence density of points, which can then be plotted with a line of best fit to describe the trend. Chapter 5 presents the results of the comparison of propagation time to distance, confirming that the lightning strike travels at near the speed of light to reach the magnetometer station. The MATLAB *fitlm* function was used to calculate the linear line of best fit and standard error of the coefficients presented in Table 5.1. Other trends, such as the amplitude of the matched initial magnetic pulses versus the distance can also be studied, and is part of the future work discussed in Chapter 6.

3.7   Individual Lightning Strikes

Thus far all the analysis has focussed on trends in large numbers of events. Using data from 7 induction coil magnetometer stations spread across North America in the CARISMA array means the regional impact of single lightning strike events can be explored. The time vectors (in *datetime* format) of the matched initial magnetic pulse datasets for multiple stations were compared to identify individual measurements at each station but which could be related to the same lightning strike. Figure 4.6 in Chapter 4 presents the magnetic signature and their spectra at four stations ranging from 532 km away from a lightning strike to 2618 km away from the same lightning strike. This

demonstrates that as the lightning energy is ducted in the Earth-Ionosphere waveguide, it continuously excites Alfvén waves that enter the ionosphere, and when conditions are suitable for reflection inside the IAR, excite waves reflected inside the cavity.

3.8   A Null Hypothesis to Test the Matching of Lightning to Magnetic Pulses

Appendix C presents the results of a null hypothesis used to test the validity of the proposed causal connection matching lightning strikes to magnetic pulses in the magnetometer data. The null hypothesis is as follows:

The matching analysis assumes that a lightning strike must be followed by a pulse in the signal measured by an induction coil magnetometer, such that this process is sequentially ordered and time-dependent, not random. Therefore, conducting the same matching and superposed epoch analysis for lightning data on a date that does not correspond to the date of the magnetometer data should result in random noise signals in the superposed time series and which do not reveal the characteristic pulse-echo signal which we associate with both the initial lightning strike related magnetic pulse and its reflection inside the IAR.

This null hypothesis was tested by selecting magnetometer data for August 25, 2009, a day when the IAR is active, as the SRS are visible in the spectral density plot, and comparing it to the WWLLN lightning data for August 24, 2009. A copy of the lightning dataset was created and all the dates were changed from August 24 to August 25, as this modification was simple and did not require any changes in the analysis codes. The figures in Appendix C show this comparison results in disorder and no clear pulse-echo signal, validating the null hypothesis and confirming the causal connection between the magnetic signals and their ordering by the time of lightning strikes. See Appendix C for more discussion of the results.

Chapter 4

Excitation of the IAR by Lightning[1]

4.1 Abstract

The existence of the IAR was first proposed in 1976 (*Polyakov*, 1976). However, the mechanism that excites the ionospheric Alfvén resonator is still actively debated, having been suggested as related to either excitation from waves incident from above in the magnetosphere (e.g., R. *Lysak*, 1991, *Trakhtengerts* et al., 1991) or from below by lightning (e.g., *Belyaev* et al., 1990, *Bösinger* et al., 2002, *Schekotov* et al., 2011). Here we focus on the lightning hypothesis. A number of theoretical models have been developed to investigate the role of atmospheric lightning as a possible excitation mechanism of the IAR (*Fedorov* et al., 2006, *Surkov* et al., 2005). However, thorough experimental analyses to verify model predictions of possible connections between lightning and the IAR have not been conducted, due in part to restricted access to lightning datasets. Here we provide an analysis using multi-point measurements from the CARISMA magnetometer network and WWLLN, that shows an unprecedented, statistically significant correlation to support the excitation of Alfvén waves inside the IAR by lightning strikes. Our results demonstrate that the structure of the Alfvén waves inside the IAR is governed by the local conditions inside the IAR. Moreover, lightning pulses can be ducted large distances through the Earth-Ionosphere waveguide, continuously exciting Alfvén waves

---

[1]Results from this chapter are being prepared for publication.

along the magnetic field that leak energy into the IAR in addition to driving the expected Schumann resonances in the atmosphere. This introduces a new paradigm for coupling atmospheric lightning and the global electric circuit and space weather, with major implications for ionospheric and magnetospheric physics, and potentially the coupled climate system.

4.2   Introduction

Since the discovery of the ionospheric Alfvén resonator (IAR), the processes which may be responsible for generating the spectral resonance structures (SRS; *Belyaev* et al., 1990) characteristic of Alfvén waves trapped inside the IAR has been debated. It is established that the IAR is a cavity within the ionosphere bounded by sharp gradients in Alfvén speed at the lower ($\sim$100 km) and more gradual gradients at the upper ($\sim$400-4000 km) boundaries of the IAR. These Alfvén speed gradients result in wave reflection. *Fedorov* et al. (2014), showed that observed magnetic pulses above a large threshold, which they associated with putative lightning strikes, can be followed by a pulse assumed to correspond to a reflection from the upper boundary of the IAR, thereby forming the IAR SRS observed in the frequency domain. However, the pulses used in their analysis were limited to those with a signal-to-noise level large enough to meet their criteria, and without lightning data the connection of the IAR SRS to a lightning source could not be made. The conclusion advanced by these authors was that the echo occurs local to the lightning strike, arguing that the potential of that strike energy to excite waves in the IAR was limited to within 1000-2000 km of where the strike occurred. This suggestion is potentially sensible for IAR near the equator, where global storm centres might provide near-constant excitation, but fails to explain the potential excitation of the IAR by lightning at higher latitudes.

The atmosphere in the Earth-ionosphere waveguide is the insulating layer of the global electric circuit between the conductive ground and the conductive E-layer of the ionosphere (e.g., E. A. *Bering*, 1995). Lightning strikes cause a short circuit that closes the global electric circuit, enabling the transport of

charge and current across the insulating layer of the atmosphere. Electromagnetic wave energy, excited by lightning, also travels around Earth, trapped in the Earth-ionosphere waveguide. This causes the Schumann Resonances, which are well-known resonances with a fundamental frequency of ~7.8 Hz, which is related to the time it takes an electromagnetic wave excited by the strike to travel the circumference of the globe at the speed of light, (i.e., ~0.128 s). The global electric circuit and the Schumann resonances are typically understood to be systems operating strictly inside the atmosphere. However, a new proposition, which we advance with our analysis, is that lightning also excites Alfvén waves inside the IAR, and that such excitation can be associated with the lightning strike. As electromagnetic wave energy is ducted in the Earth-ionosphere waveguide, it appears that there can be continual excitation of Alfvén waves inside the IAR, even relatively far from the initial lightning strike. Since the ducting effect is the source of the Schumann resonances, this effect could explain the excitation of the IAR at higher latitudes if the electromagnetic waves in fact also excite Alfvén waves as they travel around the globe.

Here we present an in depth analysis of the connection between lightning strikes and IAR SRS, arguing that this clearly excites waves in the IAR. We investigated IAR signatures in magnetometer data measured at 7 induction coil magnetometer stations in the CARISMA magnetometer array (*Mann* et al., 2008). These signatures were identified using a combination of threshold criteria with timing correlation to real lightning data from WWLLN (*Hutchins* et al., 2012). This technique allowed for the identification of large numbers of magnetic signatures of lightning associated IAR, including those with signal levels just above the background noise. When combined using a superposed epoch analysis our results show a clear correlation of individual lightning strikes to the excitation of the spectral resonance structures of the IAR. In some cases SRS can be seen at multiple magnetometers but which are excited by the same strikes, including at distances greater than the 2000 km. Our results clearly demonstrate that lightning can excite Alfvén waves in the IAR and present a new paradigm that couples energy in the global electric

circuit into the ionosphere and potentially the magnetosphere.

4.3   Results

The objective of this analysis is to verify that lightning strikes excite Alfvén waves in the IAR, and further that the characteristics of the SRS are defined by the local conditions inside the IAR (i.e., local to the magnetometer taking the measurement). The approach to verify the excitation of the IAR by lightning strikes was to identify pulse-echo signatures in magnetometer data matched to lightning, and to verify that the spectra of these signatures matched the spectral resonance structures of the IAR.

Figure 4.1 presents an overview of the magnetic field activity on August 24, 2009 and the lightning strikes measured by WWLLN that occur within 2000 km of the Ministik Lake magnetometer station in CARISMA (*Mann* et al., 2008). Between 4 UT and 11 UT (Universal Time) there is clear excitation of the IAR with spectral resonance structures (SRS) present from 1 Hz to just over 14 Hz in the power spectral density plot generated from the H (North-South) component induction coil magnetometer data as shown in the top panel of Figure 4.1. As shown in the middle panel of Figure 4.1, it is also clear that the SRS coincide with peak lightning strike activity, presented for each 1-hour interval, during the same time period. Next, all magnetic pulses in the magnetometer data above the root mean square (RMS) noise level, $\sigma_{quiet} = 2$ pT, were identified for each 1-hour interval. σ_{quiet} was determined between 16 UT and 17 UT, and this is shown by the black curve in the middle panel of Figure 4.1. This was the 1-hour interval with the lowest/quietest noise level for this 24 hour dataset, and where background noise level is unaffected by the presence of SRS. Those magnetic pulses in the magnetometer data that appeared less than 0.1 seconds after the WWLLN defined time of the single lightning strike occurrence are considered matched, the red curve in the middle panel of Figure 4.1 revealing hundreds of matched cases in each 1-hour interval, and with the peak in occurrence also coinciding approximately in time with the period where the SRS are observed. Note that as described in detail in
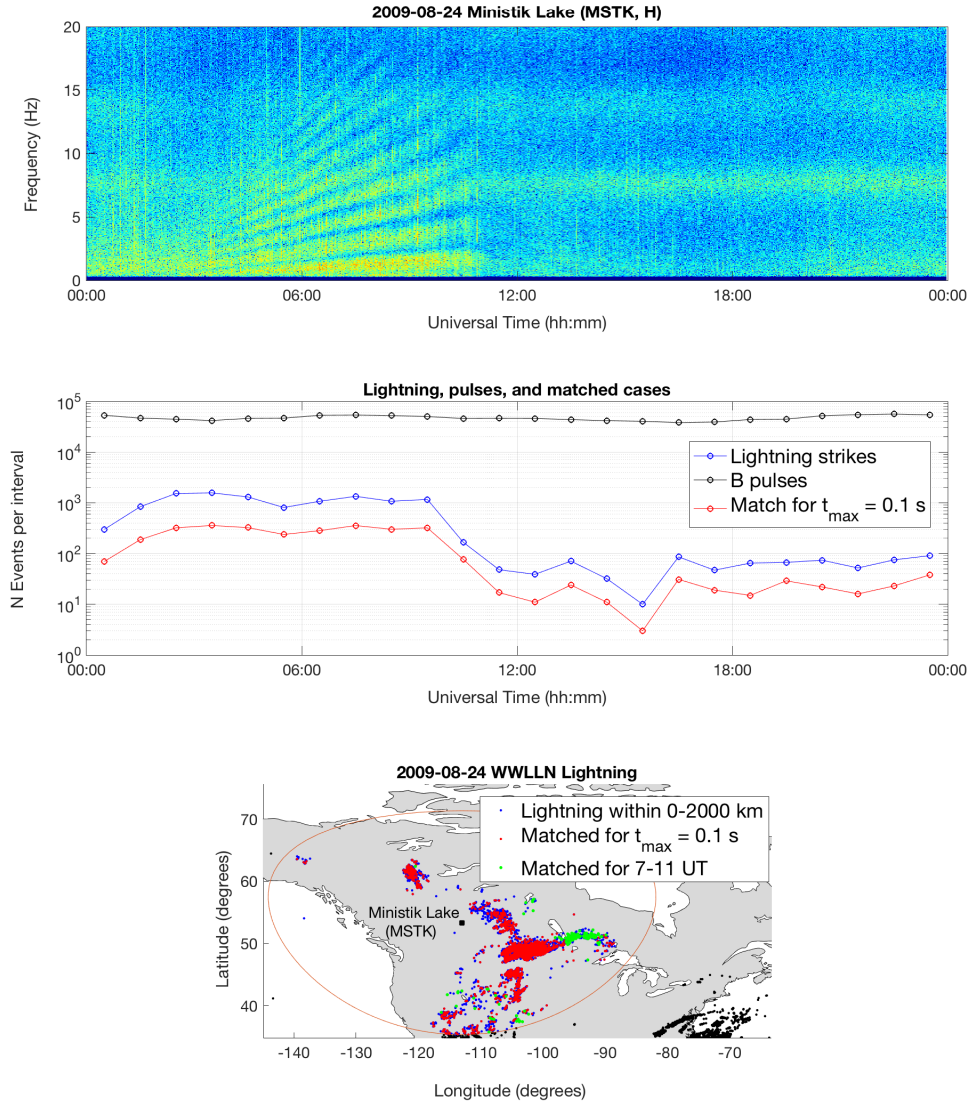
Figure 4.1: A case study of lightning strikes matched to magnetic pulses in the Ministik Lake induction coil magnetometer data on August 24, 2009. (Top) The power spectral density plot of the H-component magnetic field data. (Middle) Log scale plot of the number of lightning strikes (blue) within 0-2000 km from the Ministik Lake magnetometer station for each UT hour, the number of magnetic pulses (black) with amplitudes above σ_{quiet}, and of those magnetic pulses the subset of ones that occur within 0.1 s after a lightning strike (red). (Bottom) A map showing the location of WWLLN lightning strikes relative to the Ministik Lake magnetometer station.

Chapter 3 our analysis rejected cases when multiple matches occur within the same 0.1 second delay interval, resulting in the matched (red) curve reflecting only approximately one third of the total number of lightning strikes shown

50

in blue. Finally, the bottom panel of Figure 4.1 shows the location within the 2000 km radius from the magnetometer station where the matched lightning strikes occur. Blue dots are lightning strikes that occurred within 0-2000 km but did not match to a magnetic pulse and red dots are lightning strikes that matched to magnetic pulses. The dots highlighted in green represent those matched cases during the most active IAR period from 07 UT to 11 UT.

Rather than study the individual time domain characteristics and spectra of thousands of lightning-IAR related pulse-echo signatures, the matched events were processed using superposed epoch analysis to generate a single mean, median, and quartiles signature in the time domain in each hour-long time interval. The mean signatures of the four 1-hour intervals with the cleanest IAR signatures - those occurring from 07 UT to 11 UT - are shown in Figure 4.2 together with the spectra of the mean time domain superposed response, the median time domain superposed response, and the quartile time domain superposed responses. The time domain superposed responses for the mean, median, and quartiles themselves, from which the associated spectra in Figure 4.2 are obtained, are shown in Figure 4.3. The first notable result is the number of events identified each hour. The first three pairs of panels in Figure 4.2 and Figure 4.3 show signatures for the superposition of over 300 events in each 1-hour interval. The fourth panel had 77 cases, which we know from the middle panel of Figure 4.1 is due to the steep drop in the number of lightning strike occurrences within the 2000 km radius of the Ministik Lake station for that time interval. Notably, the median time domain response of the first three panels in Figure 4.3 clearly shows the echo signature from reflection of the Alfvén wave inside of the IAR. The fact that the echo amplitude is below the threshold of σ_{quiet} reinforces the importance of having lightning data to match the magnetic signatures to, in addition to demonstrating that the echo happens across all the events, even those with very low signal to noise. The spectra in the right hand panels of Figure 4.2 show the time domain superposed responses produce the SRS of the IAR, and the consistency across the mean, median, and quartiles demonstrate this is statistically consistent for every lightning strike associated magnetic pulse signal identified in each inter-

val. Figure 4.3 reinforces this conclusion because it shows the relationship is statistically significant in the time domain responses.

The next key feature is the time delay between the initial lightning associated magnetic pulse and the first echo from the reflection off the top boundary of the IAR, which can be assessed in the left panels of Figure 4.2 or in all the panels of Figure 4.3. The superposition of the initial magnetic pulse, all of which were processed to have positive polarity, occurs at epoch time $T = 0$ s. The magnetic threshold for the initial pulse was set at $\sigma_{quiet} = 2$ pT. The Alfvén wave reflection from the upper boundary of the IAR generates an echo pulse signal which is seen at $T = 0.52$ s, $T = 0.47$ s, $T = 0.41$ s, and $T = 0.37$ s after the initial lightning strike related pulse in each hour interval 07 to 11 UT, respectively. The progressively shorter time elapsed between the initial pulse and the echo correlates to the sloping of the frequency with time seen in the SRS shown in the top panel of Figure 4.1. This was verified by taking the reciprocal of the four time delays and comparing them to the SRS maxima seen in the power spectral density plot for the corresponding time interval, and comparing them to the first peak of in the spectra. Examining the Fourier spectra of these superposed epoch time domain signatures, (Figure 4.2, panels in the right hand column) reveals clearly the spectral peaks of the SRS. As noted above, for the first three hours the number of lightning strike occurrences is essentially constant, and then in the fourth interval the number of lightning strikes drops. However, the pattern of changing time delay and the sloping of the frequency with time seen in the SRS is not affected by the number of lightning occurrences. The variation in the time delay corresponds to the hypothesis proposed above that the local characteristics of the IAR defines the response measured in the magnetometer. The variation across these four time intervals show that the properties of the IAR cavity, most likely the Alfvén speed profile, are changing throughout the four hours. The unavoidable and significant conclusion is therefore that lightning excites waves inside the IAR.
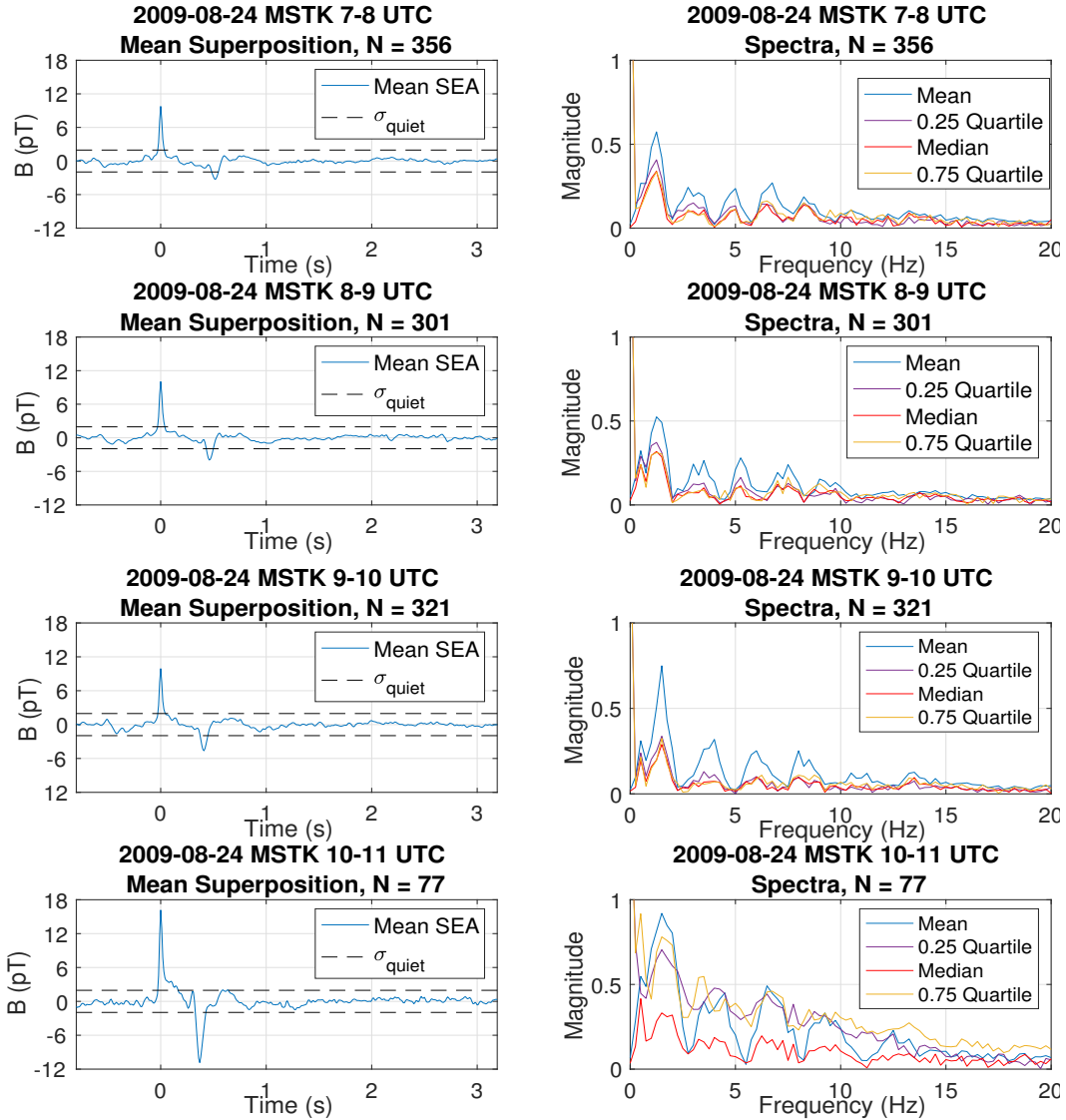
Figure 4.2: Mean superposed epoch time series (left column) and associated frequency spectra (right column) of data from the Ministik Lake magnetometer station matched to WWLLN lightning strikes for four 1-hour time intervals when the IAR is active, from 07-11 UT on August 24, 2009. The first echo from inside the IAR is clearly visible as a negative polarity pulse at $T = 0.52$ s (top left), $T = 0.47$ s (second left), $T = 0.41$ s (third left), and $T = 0.37$ s (bottom left) for each hour from 07-11 UT, respectively. The accompanying spectra clearly show that the pulse-echo signal generates the spectral resonance structures of the IAR in the frequency domain, for the mean, median and quartiles in the superposed epoch time series. See text and Appendix B for more details.
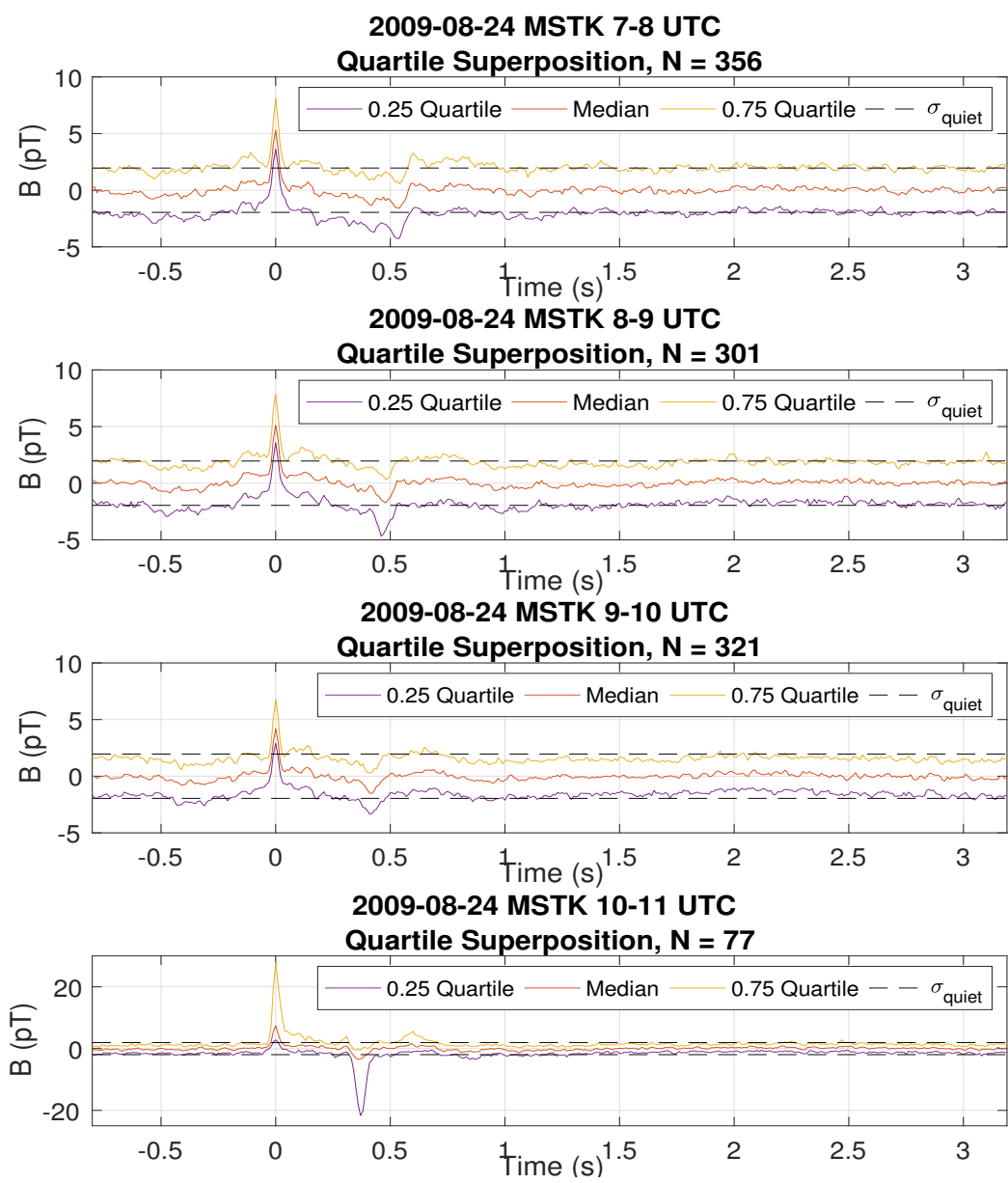
Figure 4.3: Median and quartiles time series signals from the superposed epoch analysis of data from the Ministik Lake magnetometer station matched to WWLLN lightning strikes for four 1-hour time intervals when the IAR is active, 7-11 UT on August 24, 2009. All initial lightning associated magnetic pulses were superposed with enforced positive polarity at superposed epoch 0 seconds in each 4-second window, and the initial magnetic pulse threshold was selected to be $\sigma_{quiet} = 2$ pT. The first echo from inside the IAR is clearly visible as a negative polarity pulse at $T = 0.52$ s (top), $T = 0.47$ s (second), $T = 0.41$ s (third), and $T = 0.37$ s (bottom) for each hour from 07-11 UT, respectively. The number of events superposed, N, is above each panel.

The event shown in Figures (4.1) to (4.3) is presented as a single case study for a single magnetometer station, therefore further analysis is required to verify that the characteristics of the resonance are defined by the local conditions inside the IAR. Figures (B.1) - (B.12) in Appendix B show results of the same analysis for another day when this occurs, August 25, 2014, and demonstrate that IAR excitation by lightning originating from the same source occurs simultaneously across the North American continent.

Figure (4.4) shows the frequency of the spectral maxima of the SRS visible in power spectral density plots (here that is Figure 4.1a) derived from the raw time series together with the spectral peaks from the time series of the SEA mean spectra from four CARISMA stations shown in Figures (B.2), (B.5), (B.8), and (B.11) in Appendix B. The different response of the spectral peaks at the IAR harmonics across the four stations demonstrates that the characteristics of the IAR excited by lightning are determined by local effects, presumably local variations in Alfvén speed in the IAR. Figure 4.5 shows the harmonics of the spectral maxima at each station from Figure (4.4) organized by UT in the top panel and then organized by magnetic local time (MLT) in the bottom panel, in order to consider the time dependent diurnal change in local conditions of the IAR across the stations. These two plots demonstrate that the SRS do not organize either in UT or in MLT, the SRS differs from station to station. Therefore the stations are measuring spatial and temporal variations in the local ionosphere that determine the characteristics of the SRS

Finally, Figure 4.6 provides further evidence supporting the excitation of the IAR by lightning, the control of the SRS spectra by local effects in the IAR, as well as excitation of the IAR by lightning occurring at distances well beyond 2000 km. Specifically, Figure 4.6 shows how a magnetic impulse associated with a single lightning strike can be measured at four different magnetometer stations, this lightning strike happening in the WWLLN data at 06:28:22 UT on August 24, 2009 (the day of the event in Figure (4.1)). Below the map showing the strike and the four stations, the left panels show the time domain signatures at each station, in which the time of the lightning strike is marked by the dashed vertical line. The right panels show the accompanying spectra

derived from the time domain signals at each station, in which the peaks correspond to the SRS of the IAR. The SRS characteristics at each station differ noticeably in amplitude, the lowest being Dawson City, which is the furthest from the strike, and slightly in frequency at each station, and this points to local variations in IAR characteristics. The initial electromagnetic pulse excited by the same lightning strike reaches each station almost simultaneously, propagating at the speed of light in the Earth-ionosphere waveguide. This single electromagnetic pulse appears to continuously excite Alfvén waves as it propagates, which travel up into the IAR, reflecting off the upper boundary and returning as the first echo. The lag time, polarity, amplitude, and spectra of that echo varies from station to station, as expected if the observed SRS at each station are being determined by different local Alfvén speed characteristics inside the IAR above each station. For example, the time domain superposed responses at the Pinawa and the Thief River Falls magnetometer stations very nearly identical in shape, polarity, amplitude, and time delay between the initial lightning associated pulse and the echo from inside the IAR, as expected since those two stations are quite close to each other. The response at the Ministik Lake station provides an interesting contrast. The signal is very similar generally, but has many more small time scale variations and the time delay of the echo from inside the IAR is slightly longer at Ministik Lake. The similarity of the signals is likely because relative to the location of the lightning strike, the distance travelled to the three stations at Ministik Lake, Pinawa, and Thief River Falls, is very similar; 760 km, 532 km and 558 km respectively. The differences are likely because the electromagnetic pulse travels West (and slightly North) to Ministik Lake, and East (and slightly South) to Pinawa and Thief River Falls, and the conditions in the IAR are probably different in those two regions at that time. Another detail of note is the clear signature of the Schumann resonance in the time domain shortly after epoch time 0 seconds, which corresponds to the characteristic signature analysed in detail in section 3.4.2.
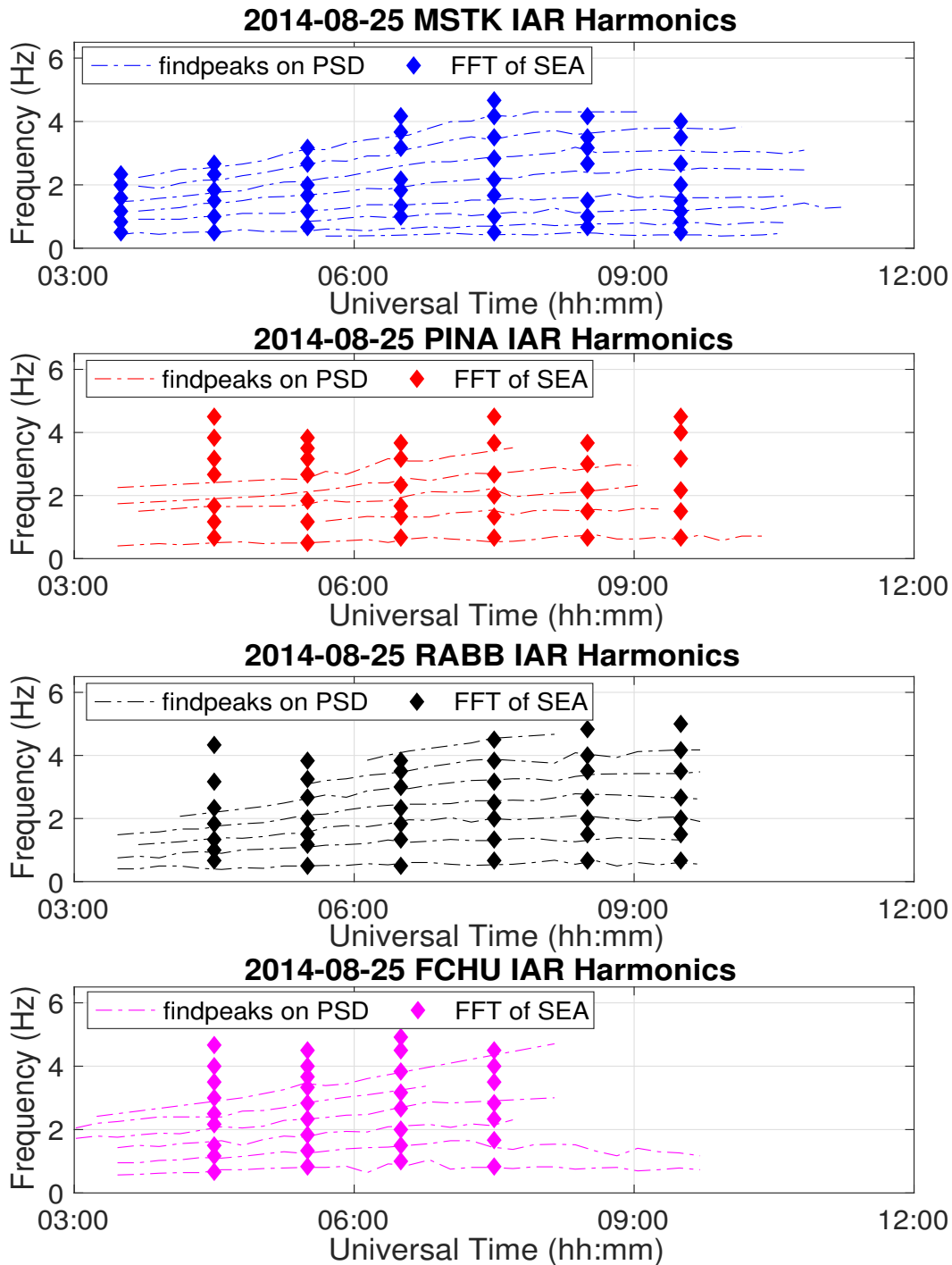
Figure 4.4: Characteristics of the frequencies at peak power in IAR spectral resonance structures from four different magnetometer stations, compared with the spectral peaks from mean superposed epoch analysis (SEA) of magnetic pulse signals matched to lightning on August 25, 2014 (see text for details). The stations are (top) Ministik Lake station, (second) Pinawa station, (third) Rabbit Lake station, and (bottom) Thief River Falls station (see www.carisma.ca for details of station locations).

2014-08-25 IAR Harmonics Organized UTC

2014-08-25 IAR Harmonics Organized by MLT
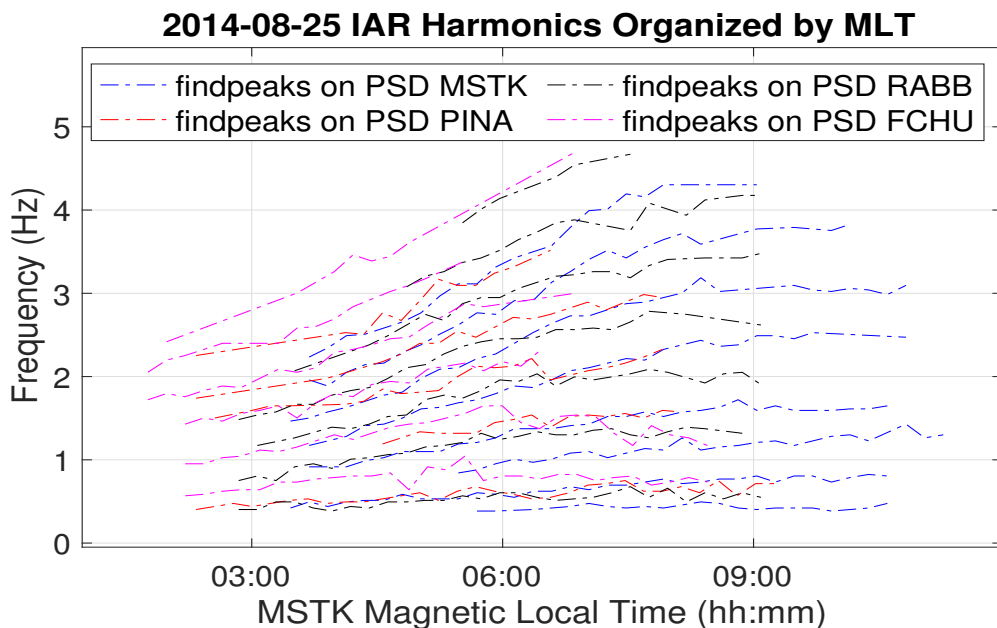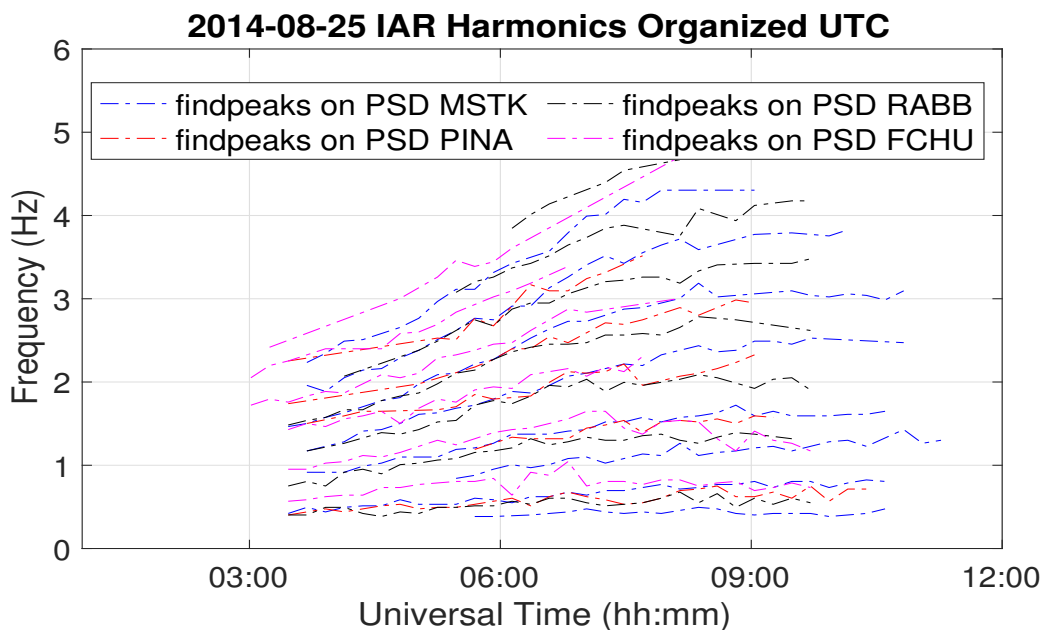
Figure 4.5: Characteristics of the frequencies at peak power in IAR spectral resonance structures from four different magnetometer stations, plotted all together as a function of UT (top) and magnetic local time (MLT) relative to Ministik Lake (bottom) on August 25, 2014 (see text for details). The stations are (blue) Ministik Lake station, (red) Pinawa station, (black) Rabbit Lake station, and (magenta) Thief River Falls station (see www.carisma.ca for details of station locations).
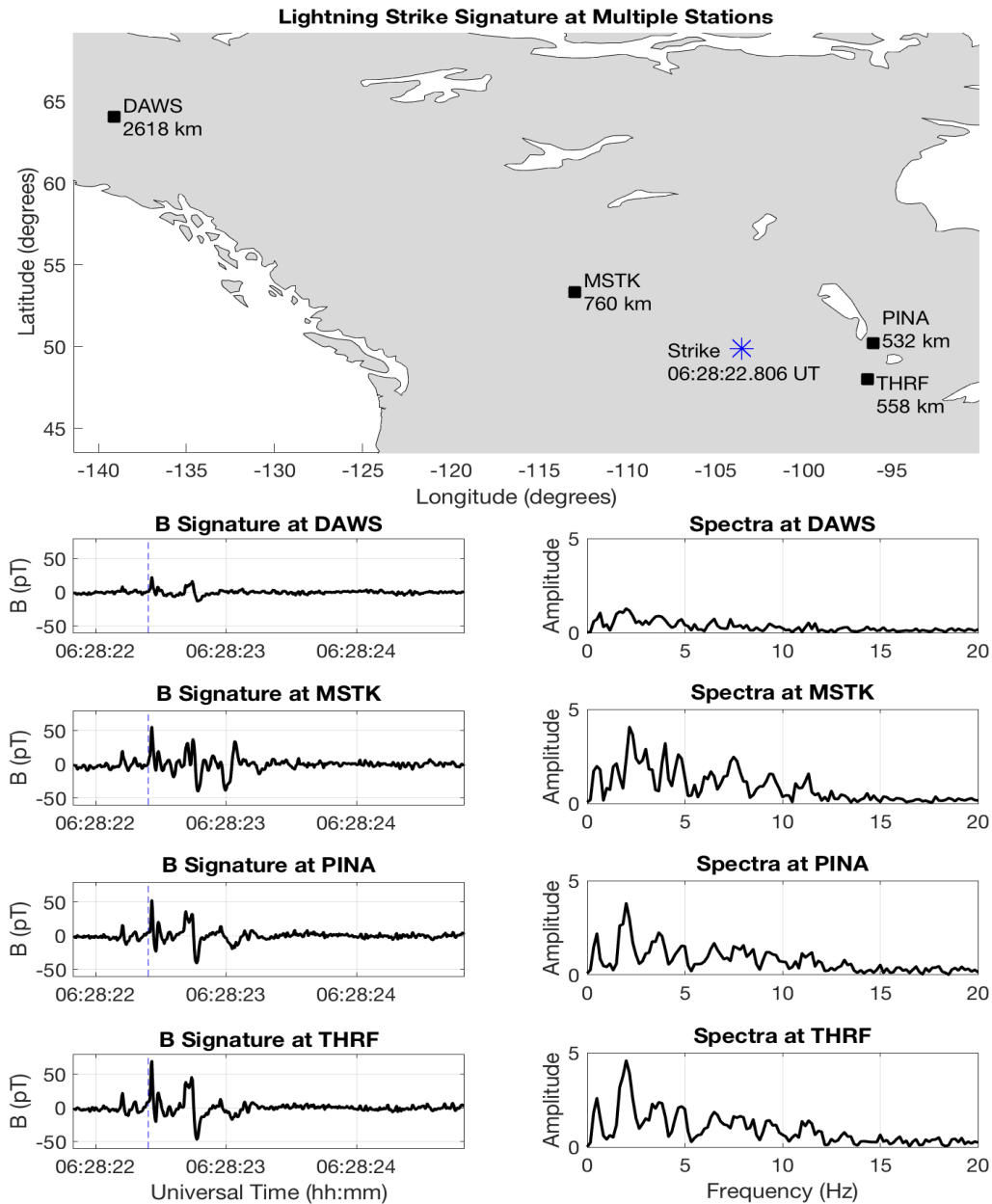
Figure 4.6: An example case of individual time domain signatures showing initial lightning associated magnetic pulses followed by echoes due to Alfvén waves reflecting from the top boundary of the IAR, simultaneously at four magnetometer stations across the CARISMA network, all triggered by the same single lightning strike (blue star) on August 24, 2009. (Top) Map showing the location of the lightning strike and the magnetometer stations, the time of the of the lightning strike, and the distance between the strike and the four stations. (Left panels) Time domain signatures at each station. (Right panels) Accompanying spectra derived from the time domain signals at each station. See text for more details.

4.4 Discussion and Conclusions

The results presented here demonstrate that lightning strikes play a crucial role in the excitation of Alfvén waves inside the ionospheric Alfvén resonator at latitudes far from the equator. Although this was first suggested nearly 30 years ago (e.g., *Belyaev* et al., 1990), the lack of experimental data from both magnetometers and lightning detectors has prevented prior experimental confirmation of this link. As Figure (4.6) demonstrates, clearly the characteristic frequencies present in the SRS due to lightning excitation are controlled by local effects presumably due to the local Alfvén speed conditions inside the IAR at any specific location. The effect in Figure 4.6 is for a single lightning strike, and using the superposed epoch analysis to study this in large numbers of events shows the pulse-echo signature is significant across this large number of events. This link to local effects is further supported when comparing the peaks of the spectra calculated from the superposed time domain signatures with the characteristics of the frequencies at peak power in IAR SRS, as shown in Figures 4.4 and 4.5, where the mismatching of the peak SRS signatures also indicates variation in the conditions of the IAR. This discovery was made due to the installation of induction coil magnetometers across the North American continent, as part of the expanded CARISMA network.

The process of ducting a lightning triggered electromagnetic signal results in the continual excitation of Alfvén waves inside the IAR at continent scales, such dynamics represent an entirely new paradigm for atmosphere-ionosphere coupling with potential impacts on the global electric circuit. This new paradigm also introduces potential new and important implications for magnetospheric physics. For example, when resonance inside the IAR is inactive, what happens to Alfvén waves which enter the cavity and propagate up the field line? Presumably they continue to propagate into the magnetosphere, perturbing that environment. A prior study conducted by *Schekotov* et al., 2011 presented a similar superposed epoch analysis using data from a single magnetometer station and in the absence of lightning data. This approach could hence not unequivocally associate the excitation of the IAR with

lightning nor elucidate that local characteristics of the IAR are a key factor that defines the SRS response. As a result those authors underestimated the impact of non-local lightning strikes, stating that *"in our opinion, the SRS can be excited by regional thunderstorms, within thousand km."* In contrast, the results in Figure (4.6) show that lightning can have a significant impact from much further away at distances much greater than 2000 km. Further studies of the lightning induced IAR signatures should seek to link specific features in the signature to specific characteristics of the IAR, perhaps by combining with diagnosis of the density inside the IAR cavity, perhaps using ionosondes to remote-sense the electron densities as was done by *Parent* et al. (2010). Overall, this chapter clearly shows that there is no doubt not only that lightning excites Alfvén waves in the IAR, but also that this process likely introduces important coupling between terrestrial and space weather, and could have significant impacts on the global electric circuit.

Chapter 5

Local and Non-Local Excitation of the IAR by Lightning[1]

5.1 Abstract

Lightning is a near-constant global phenomena, however most activity is concentrated in storm centres near the equator (*Williams*, 1992). If lightning is a significant source of excitation for the ionospheric Alfvén resonator, which appears at both low and at high latitudes, then pulse-echo signatures of the ionospheric Alfvén resonator in ground magnetometer data measured at high latitudes might be causally linked to lightning strikes far away. Here we present an analysis of pulse-echo signals in induction coil magnetometer data from CARISMA which have been matched to lightning strikes using data from WWLLN at distances of 0 km to 10,000 km away from the magnetometer. We find that matched initial lightning-related magnetic pulses occur within a time $t_{propagation}$ defined by a linear relationship to the distance of the strike away from the station, demonstrating propagation speeds derived based on the WWLLN strike timing and the time of the peak of the magnetic signal of between 0.7 to 0.93 times the speed of light. Echoes in the time series corresponding to the Alfvén wave reflection off the top boundary of the ionospheric Alfvén resonator were identified in magnetic signals matched to lightning strikes up to 10,000 km away. However, the amplitude of the echoes from within the IAR drop below the quiet time noise level for distances be-

---

yond 6000 km. The results further verify the process in which lightning strikes excite electromagnetic waves which duct in the Earth-ionosphere waveguide, travelling at speeds near the speed of light, and show that Alfvén waves in the IAR can be excited by local as well as non-local lightning strikes. Our results contradict previous studies which have suggested that 2000 km was the furthest distance from which a lightning strike could contribute to excitation of Alfvén waves inside the IAR.

5.2   Introduction

Lightning strikes occur at a rate of $\sim$100 strikes each second across the entire Earth (e.g., *Surkov* et al., 2006). However, the majority of lightning occurs in storm centres at tropical latitudes, as shown in Figure 5.1 and which was taken from *Williams* (1992). This presents a challenge for lightning excitation of Alfvén waves inside the IAR at higher latitudes, because the atmosphere attenuates the electromagnetic energy of lightning strikes as they propagate in the Earth-Ionosphere waveguide, such that the energy in the frequency range of the IAR drops off with distance (e.g., *Surkov* et al., 2006). *Surkov* et al. (2006) and *Schekotov* et al. (2011) highlight this point to argue that lightning power is not sufficient to act as a mechanism to excite the IAR at mid-latitudes and higher. These authors support their argument with experimental data from a single magnetometer station in the Kamchatka peninsula (52.94°N, 158.25°E) paired with a stocastic lightning model and data for lightning within a small radius of only 300 km from the magnetometer station. These authors point out they were unable to obtain data for lightning at greater distances and this limited their analysis.

A more in depth analysis of the effect of non-local lightning is possible using data from WWLLN, since these datasets contain lightning strike occurrence data for the whole globe. This analysis is what is presented here. The following analysis and results (with additional figures presented in Appendix D) demonstrate that the magnetic pulse-echo response associated with lightning excitation of the IAR cavity can occur for lightning at distances from 0

km up to ∼10,000 km from the magnetometer measuring the IAR response. Furthermore, by using measurements from multiple magnetometer stations, the electromagnetic wave propagation time from the strike location to the magnetometers is determined to be near light speed. Ultimately, the major advantage of pairing the magnetometer signals with WWLLN lightning data spanning the whole world is that the identification of the magnetic pulse-echo signals is not solely dependent on a threshold for the initial electromagnetic pulse associated with the lightning strike as measured at the magnetometer station. Without the world-wide lightning data, a carefully selected threshold above the background noise needs to be set to ensure sufficient signal to noise ratio of the echo pulse resulting from the reflection of the Alfvén wave in the IAR, while also maintaining large enough statistics. This was the challenge encountered in prior studies by *Surkov* et al. (2006), *Schekotov* et al. (2011), and *Fedorov* et al. (2014). For example, in *Fedorov* et al. (2014) a threshold of 3-4 standard deviations was implemented for identification of the relevant lightning associated magnetic pulses and which only to generated around 30-40 pulses per hour. In our analysis, pulses just above the background noise can be confidently selected as long as they meet the lightning matching criteria, described in detail in Chapter 3, enabling the analysis of much larger numbers of events, in the results we show here sometimes exceeding 500 events per hour.

5.3 Results

The objective of this analysis is to establish how far away lightning strikes can occur from an induction coil magnetometer and still cause a local excitation of the ionospheric Alfvén resonator. An additional goal is to better understand the process of how the strike energy is coupled into the IAR; our working hypothesis being that this could occur via the intermediary of the propagation of electromagnetic waves which are ducted in the Earth-ionosphere waveguide. The analysis used in Chapter 4 was applied to magnetometer data from Ministik Lake induction coil magnetometer station on August 24, 2009, and matched to WWLLN identified lightning strikes occurring from between 0-10,000 km
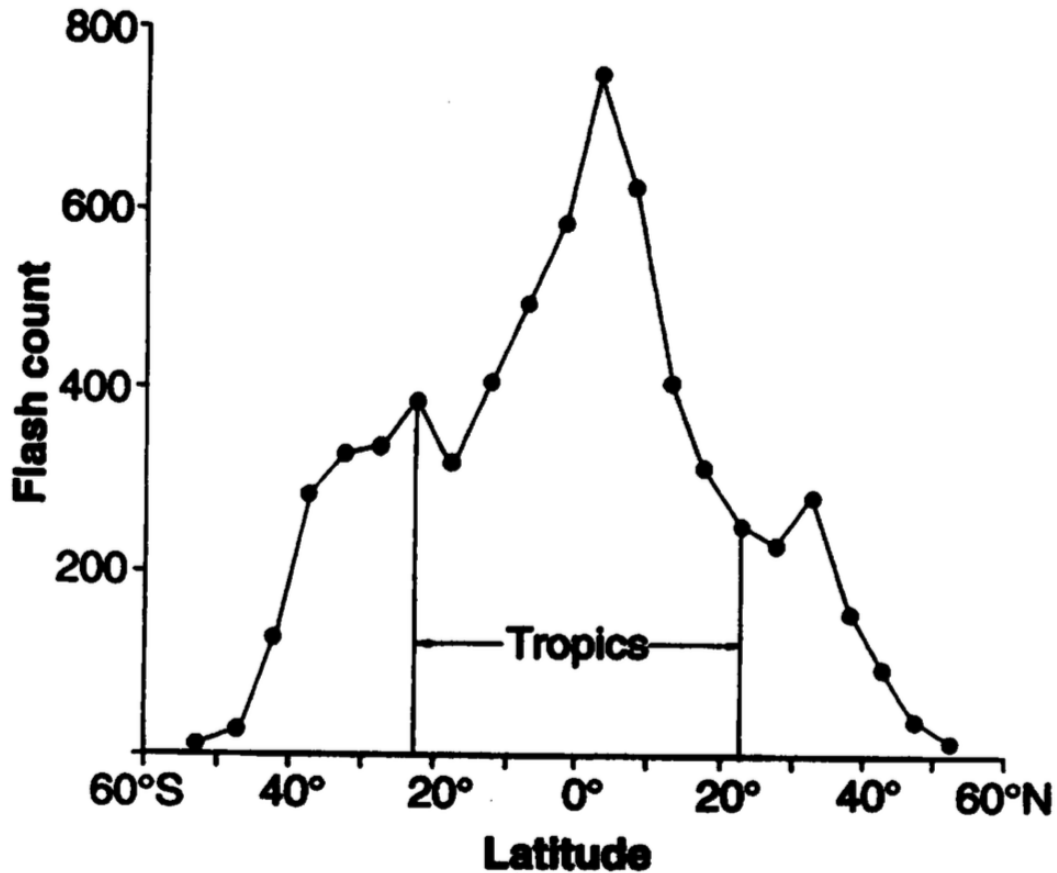
Figure 5.1: Global distribution of lightning by latitude (taken from *Williams*, 1992).

away from the station. Figure 5.2 presents the relationship between the strike to magnetometer distance and the propagation time between the strike, as determined by WWLLN, and the time of the magnetic peak in the corresponding lightning-related magnetic pulse. For the four 1-hour periods shown in Figures (5.2a), (5.2b), (5.2c), and (5.2d), the areas of peak density for the propagation time, marked by yellow x's, lies between 0.04 seconds and 0.06 seconds. The different concentrations of event occurrence clearly demonstrate the expected connection to storm centres concentrated at different distances from the station. It is interesting to further note that the panels in Figure 5.2 show the storms are moving from hour to hour, which is most clearly evident with the nearest storm centre at the bottom of each panel.

The increased propagation time at the more distant storm centres in Figure

65

5.2 suggests a linear relationship for strike distance versus the propagation time between the WWLLN strike timing and the time of the peak in the lightning-related initial magnetic pulse. To examine this further, the same analysis was carried out for data at three other stations, Dawson City, Pinawa, and Thief River Falls and the locations of peaks in occurrence density plotted together with those for Ministik Lake in Figures (5.2e), (5.2f), (5.2g), and(5.2h), demonstrating a linear relationship for each magnetometer station. The slopes of the best fits provide a estimate of propagation speed and range from 210,000 km s^{-1} to 280,000 km s^{-1}, on the order of the speed of light. The parameters of the linear fit for each panel, with standard error for the coefficients, are given in table 5.1. This result demonstrates that the lightning associated initial magnetic pulses from distances up to 10,000 km away from the magnetometer can be identified, and that the propagation time of the strike to the matched magnetic pulse is defined by a relation that implies a propagation speed close to the speed of light, just as expected. However, the subsequent signals which follow the initial magnetic pulse must also be analysed to assess whether non-local lightning strikes also excite the ionospheric Alfvén resonator local to the monitoring magnetometer.

$$D = (2.5 \pm 0.3) \times 10^5 \text{ km/s} * t - (10 \pm 2) \times 10^3 \text{ km}$$

$$D = (2.8 \pm 0.6) \times 10^5 \text{ km/s} * t - (11 \pm 3) \times 10^3 \text{ km}$$

$$D = (2.1 \pm 0.5) \times 10^5 \text{ km/s} * t - (8 \pm 2) \times 10^3 \text{ km}$$

$$D = (2.7 \pm 0.2) \times 10^5 \text{ km/s} * t - (10 \pm 1) \times 10^3 \text{ km}$$

Table 5.1: Equations of linear fit for lightning strike to magnetometer distance versus the matched propagation time of the strike to the initial magnetic pulse on August 24, 2009 for the UT hours of 4-5, 6-7, 8-9, and 10-11, respectively. These equations correspond to the lines of best fit from the panels in the right column in Figure (5.2), with standard error of the coefficients calculated using the MATLAB *fitlm* function. See text for details.
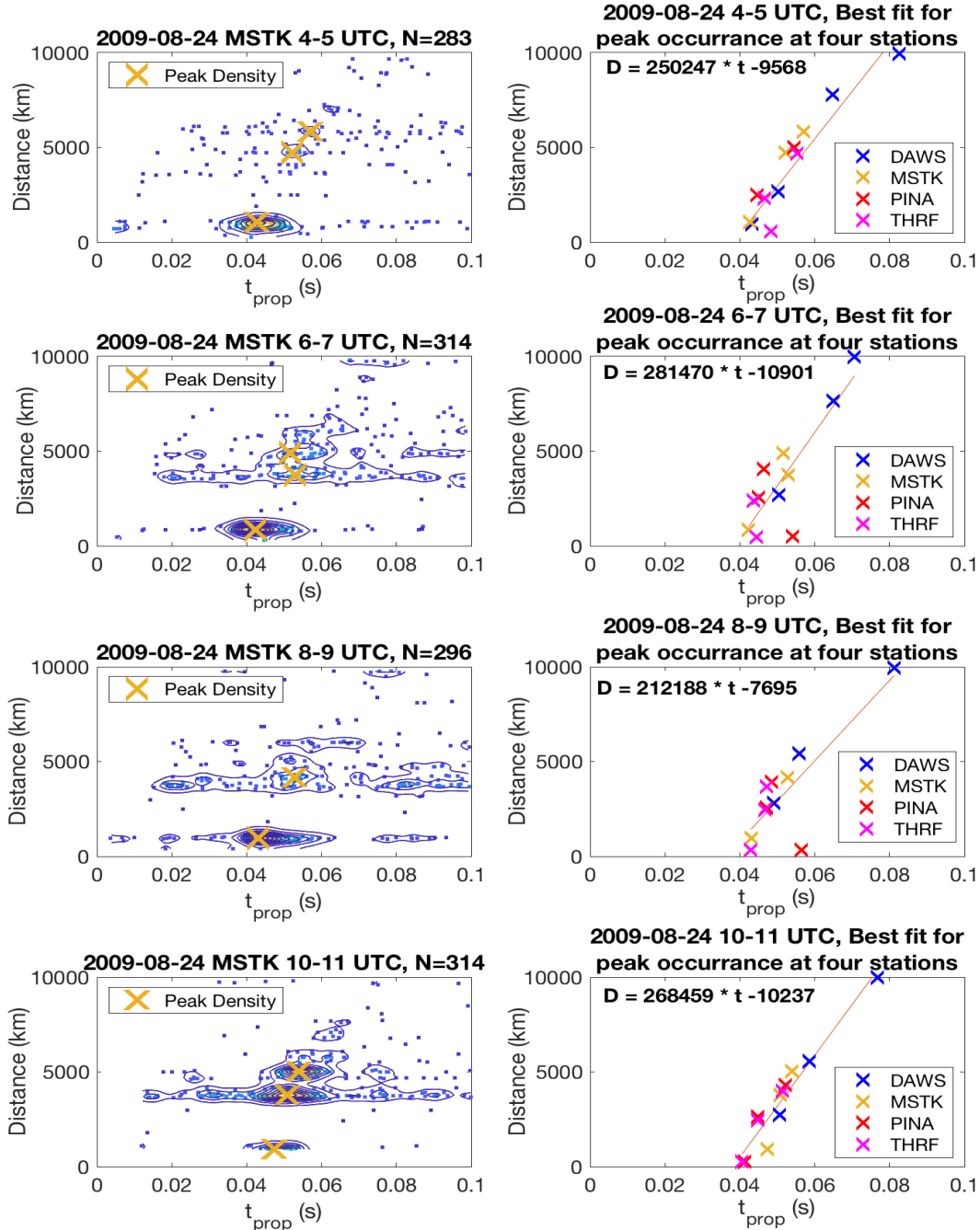
Figure 5.2: A case study of the relationship between the lightning strike to magnetometer distance and the propagation time of the strike to the peak of the initial magnetic pulse on August 24, 2009. The left column shows the scatter plot with density contours identifying the areas of largest occurrence where most data points occur for the Ministik Lake (MSTK) station. The peak occurrence densities are marked by an X. The right column shows the linear fit for the peak density points at Ministik Lake as well as that from similar analysis from three other stations at Dawson City (DAWS), Pinawa (PINA), and Thief River Falls (THRF).

67

Figures 5.3 to 5.7 provide a comparison of the superposed time series response and the frequency spectra of the SEA mean, median, and quartile time series for signals originating from lightning strikes at different distances from the Ministik Lake magnetometer station. For consistent comparison, a quantile threshold of 0.9 was applied to event selection, such that only the 10% largest signals are included in each superposed interval (see section 3.3.2 for a detailed explanation). In the first case shown in Figure 5.3, lightning strikes from between 0 to 2000 km away from the station result in mean responses with magnetic pulse amplitudes $\sim \pm$10-20 pT and IAR echo amplitudes $\sim \pm$5-15 pT. In addition, the spectra of the mean pulse-echo signals show very clear spectral resonance structures (SRS) of the IAR. Figure 5.4, which shows the same analysis for lightning strikes for between 2000-4000 km away from the station, shows the pulse-echo signal is still present. However, the mean response amplitude of the initial magnetic pulse has dropped to $\sim \pm$5-15 pT, and the IAR echo amplitude has dropped to $\sim \pm$2 pT. At between 4000-6000 km from the station, shown in Figure 5.5, the pulse-echo signal is still very strong, stronger than between 2000-4000 km from the station, and typically shows a greater number of matched cases. The mean response amplitude of the initial magnetic pulse has dropped to $\sim \pm$5-10 pT, and the IAR echo amplitude is between $\sim \pm$2-4 pT. The same analysis is shown for between 6000-8000 km and between 8000-10,000 km in Figures 5.6 and 5.7, respectively. The spectra for the non-local response still show signatures consistent with the expected spectral resonance structures of the IAR, but they are approximately half the amplitude of the spectra for signals produced by lightning strikes nearest to the station.

Overall, these results demonstrate that lightning at distances greater than 2000 km can and do excite Alfvén waves that travel across the lower ionospheric boundary and into the IAR. Waves can also reflect off the upper IAR boundary, producing the echo signal in the magnetometer. However the signals are attenuated significantly compared to the signals associated with lightning strikes within 2000 km. Appendix D presents the SEA time series results together with the quartiles of the superposed responses. All of which confirm

the earlier conclusion that local and non-local lightning can well excite Alfvén waves inside the IAR.

Figure 5.3: (Top) A map showing Ministik Lake magnetometer station, where blue dots are lightning strikes that occurred within a radius of between 0-2000 km away from but did not match to a magnetic pulse, red dots are lightning strikes that matched to magnetic pulses, and green dots are the matched magnetic pulses occurring during four 1-hour time intervals when the IAR is active, between 7-11 UT. (Bottom 8 panels) Mean superposed epoch analysis (left column) and spectra of the SEA mean, median, and quartile time series (right column). Data are from the Ministik Lake magnetometer station, matched to WWLLN lightning strikes up to 0-2000 km away, for four 1-hour time intervals when the IAR is active, from 7-11 UT on August 24, 2009.

Figure 5.4: (Top) A map showing Ministik Lake magnetometer station, where blue dots are lightning strikes that occurred within a radius of between 2000-4000 km away from but did not match to a magnetic pulse, red dots are lightning strikes that matched to magnetic pulses, and green dots are the matched magnetic pulses occurring during four 1-hour time intervals when the IAR is active, between 7-11 UT. (Bottom 8 panels) Mean superposed epoch analysis (left column) and spectra of the SEA mean, median, and quartile time series (right column). Data are from the Ministik Lake magnetometer station, matched to WWLLN lightning strikes up to 2000-4000 km away, for four 1-hour time intervals when the IAR is active, from 7-11 UT on August 24, 2009.

Figure 5.5: (Top) A map showing Ministik Lake magnetometer station, where blue dots are lightning strikes that occurred within a radius of between 4000-6000 km away from but did not match to a magnetic pulse, red dots are lightning strikes that matched to magnetic pulses, and green dots are the matched magnetic pulses occurring during four 1-hour time intervals when the IAR is active, between 7-11 UT. (Bottom 8 panels) Mean superposed epoch analysis (left column) and spectra of the SEA mean, median, and quartile time series (right column). Data are from the Ministik Lake magnetometer station, matched to WWLLN lightning strikes up to 4000-6000 km away, for four 1-hour time intervals when the IAR is active, from 7-11 UT on August 24, 2009.
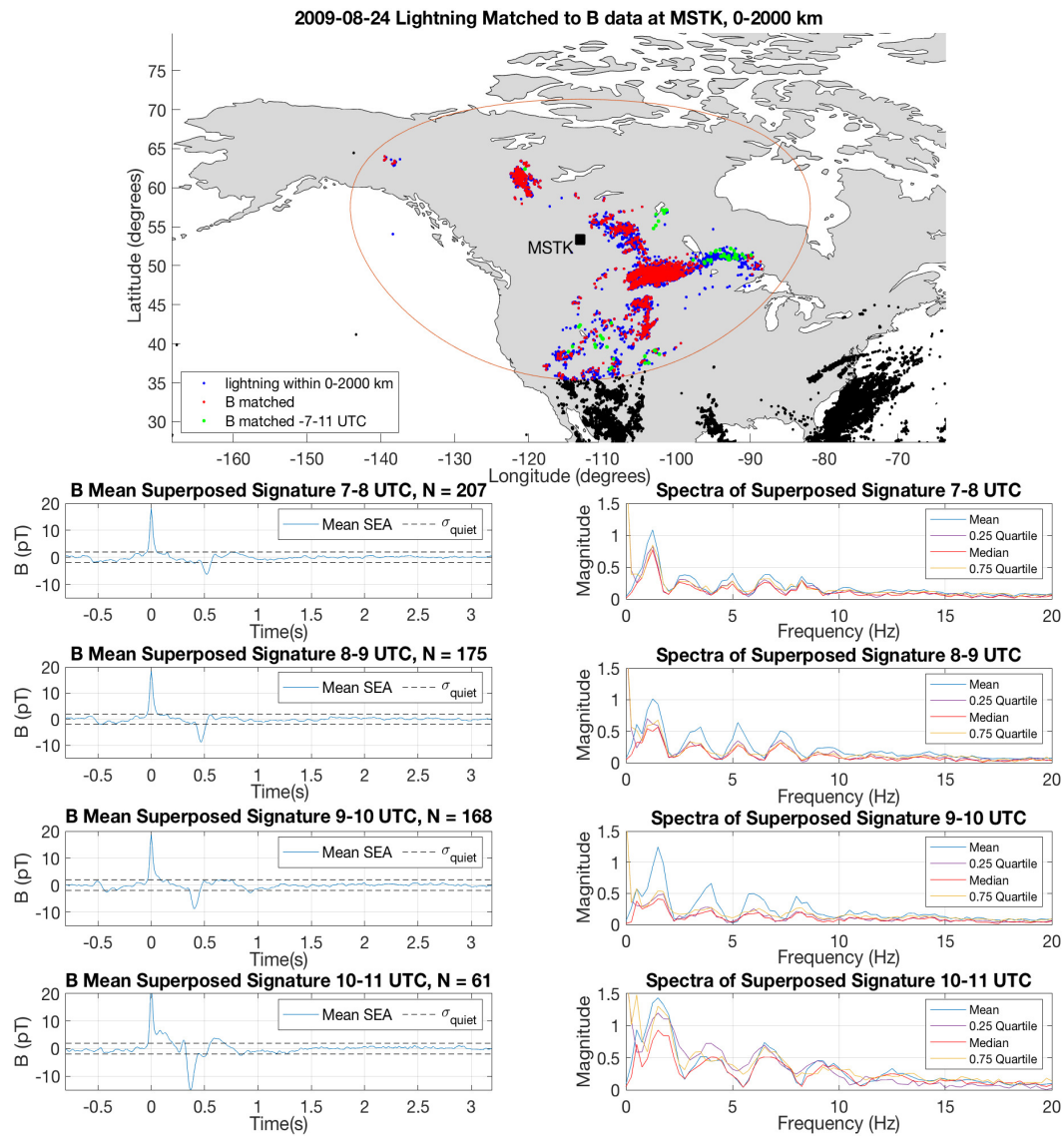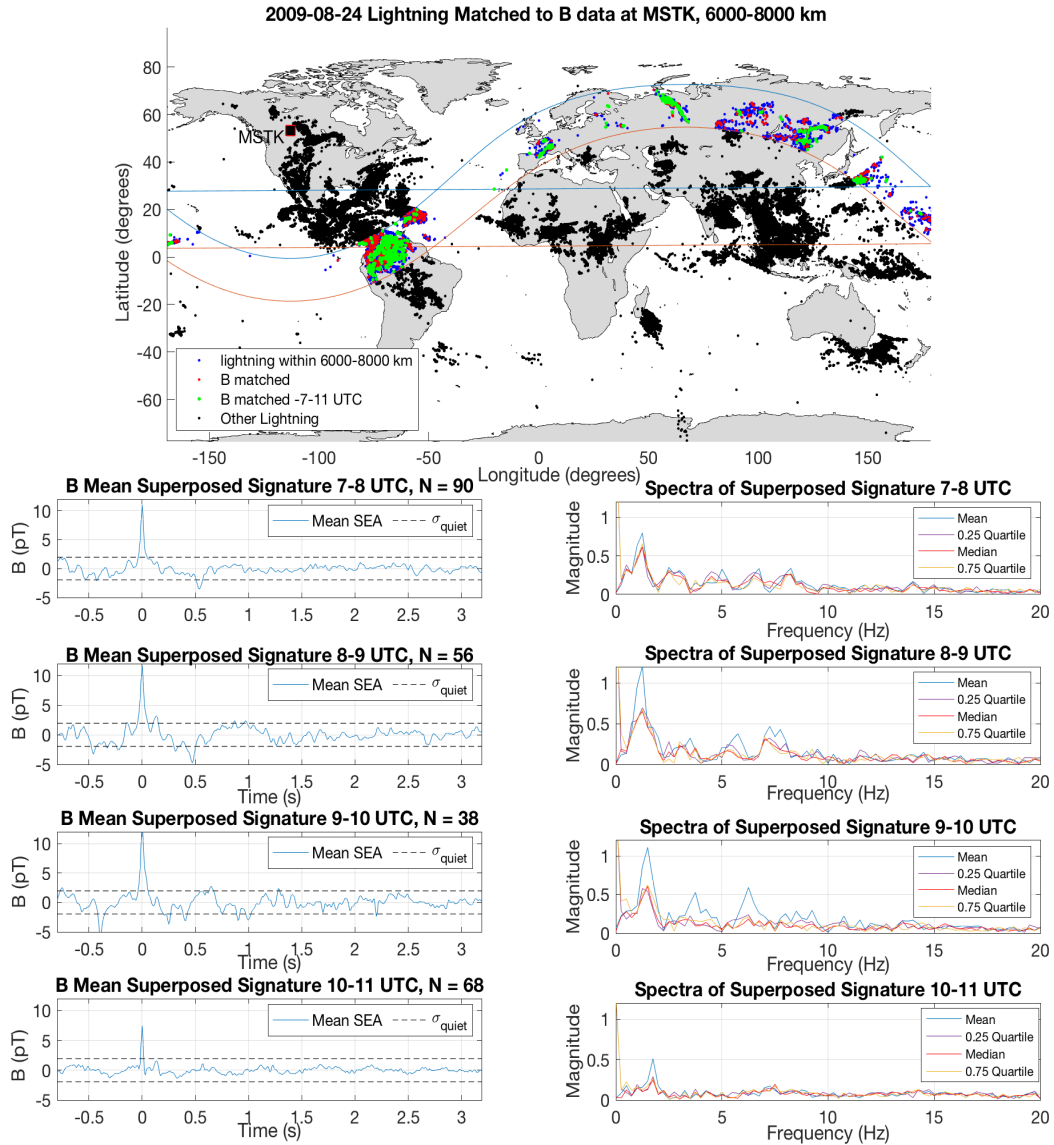
Figure 5.6: (Top) A map showing Ministik Lake magnetometer station, where blue dots are lightning strikes that occurred within a radius of between 6000-8000 km away from but did not match to a magnetic pulse, red dots are lightning strikes that matched to magnetic pulses, and green dots are the matched magnetic pulses occurring during four 1-hour time intervals when the IAR is active, between 7-11 UT. (Bottom 8 panels) Mean superposed epoch analysis (left column) and spectra of the SEA mean, median, and quartile time series (right column). Data are from the Ministik Lake magnetometer station, matched to WWLLN lightning strikes up to 6000-8000 km away, for four 1-hour time intervals when the IAR is active, from 7-11 UT on August 24, 2009.
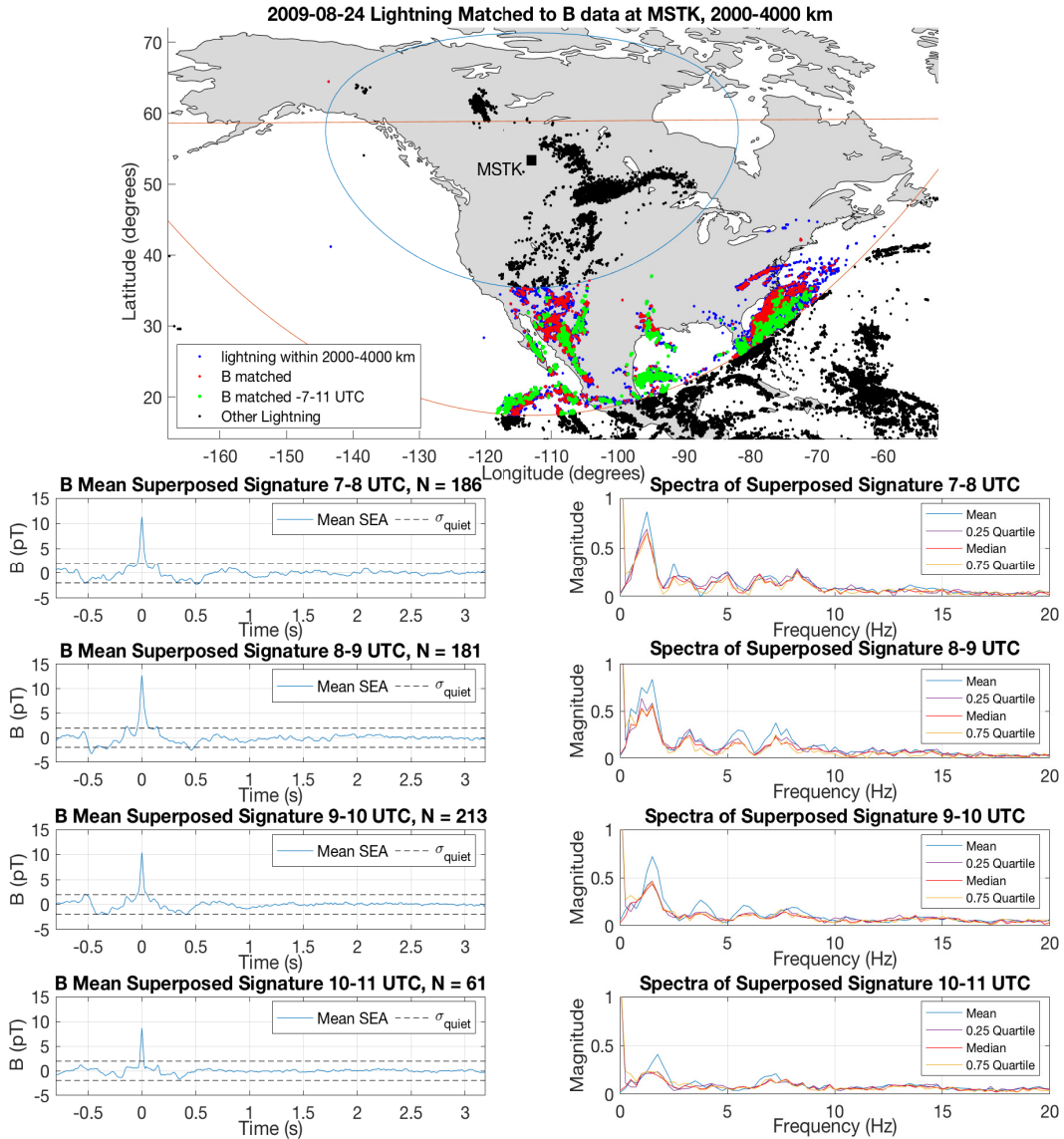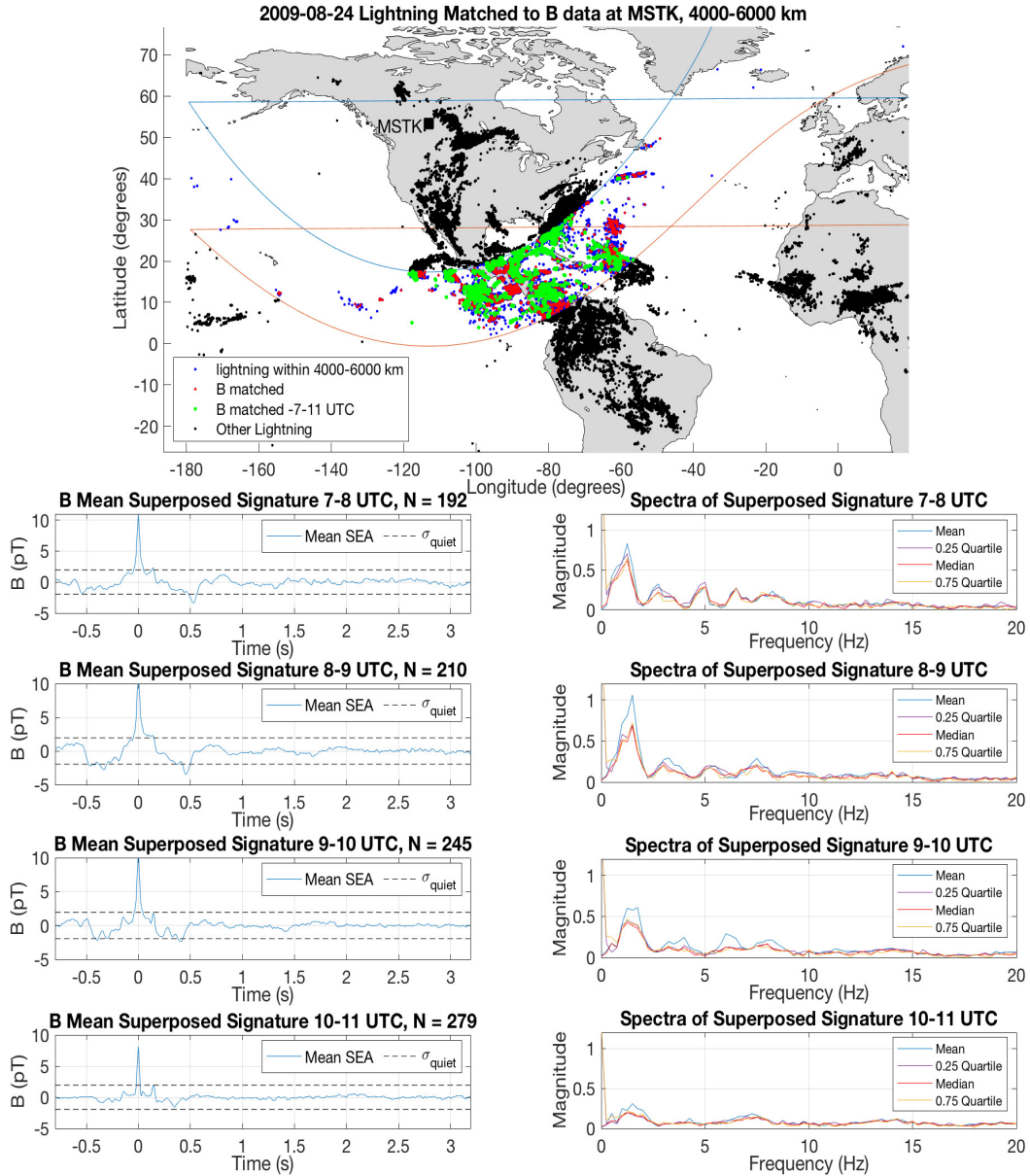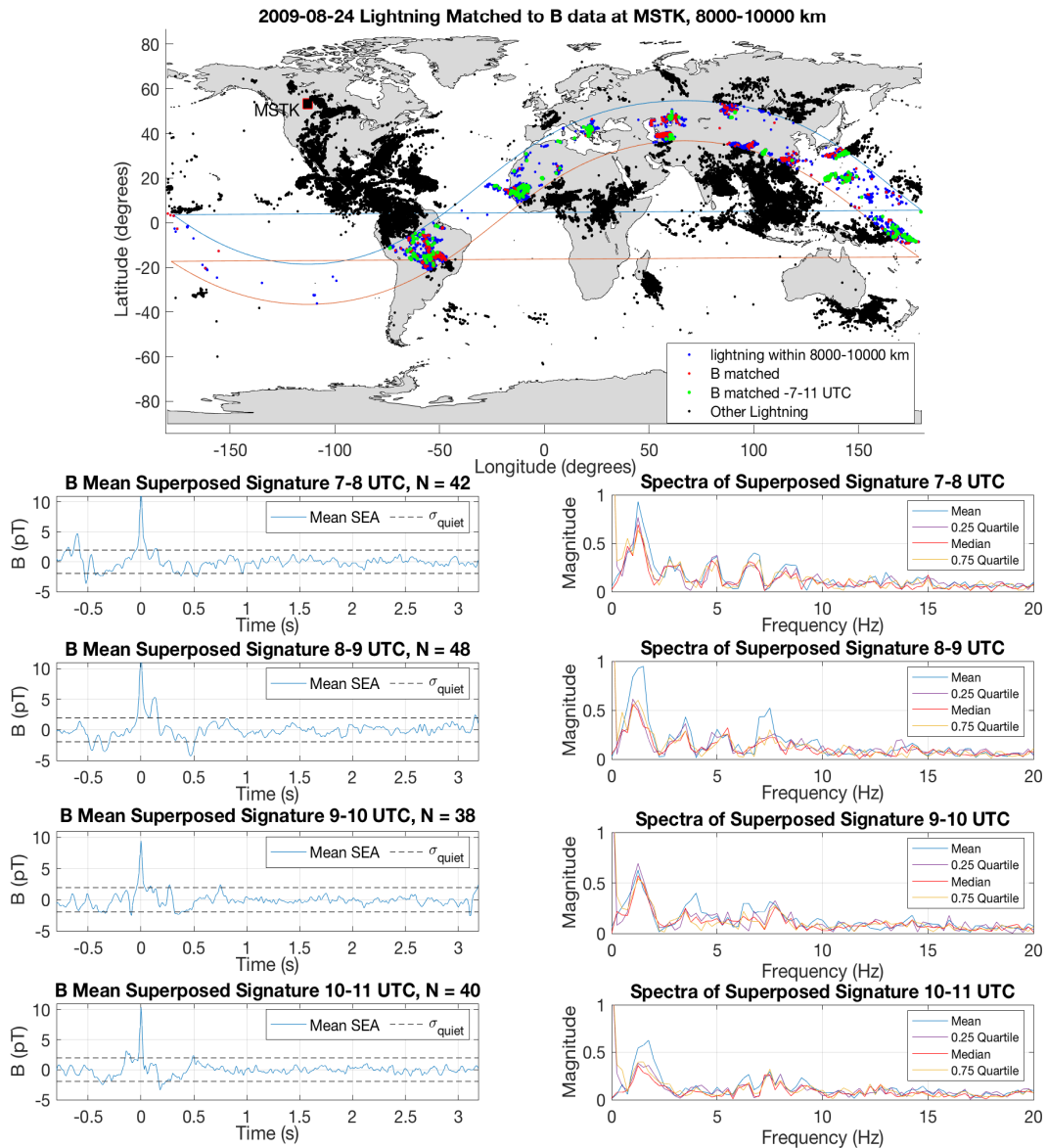
Figure 5.7: (Top) A map showing Ministik Lake magnetometer station, where blue dots are lightning strikes that occurred within a radius of between 8000-10,000 km away from but did not match to a magnetic pulse, red dots are lightning strikes that matched to magnetic pulses, and green dots are the matched magnetic pulses occurring during four 1-hour time intervals when the IAR is active, between 7-11 UT. (Bottom 8 panels) Mean superposed epoch analysis (left column) and spectra of the SEA mean, median, and quartile time series (right column). Data are from the Ministik Lake magnetometer station, matched to WWLLN lightning strikes up to 8000-10,000 km away, for four 1-hour time intervals when the IAR is active, from 7-11 UT on August 24, 2009.

5.4 Discussion and Conclusions

The results presented in this chapter not only verify the causal nature of lightning excitation for waves in the IAR, but also show that lightning-IAR pulse-echo signatures identified in ground magnetometer data are associated with electromagnetic signals that propagate at nearly the speed of light from the location of the lightning strike to the magnetometer. Based on our results, it is now clear that non-local lightning strikes have sufficient energy to excite and register IAR signals above the noise threshold of the induction coil magnetometers in the CARISMA network. By conducting a superposed epoch analysis (SEA) on these magnetic signals, matched to causal lightning strikes at distances 0-10,000 km away from the station, the echo signal of the Alfvén wave travelling up the field line and reflecting off the top boundary of the IAR was also identified. With greater distance the signal amplitude does drop, yet the response on the frequency domain still shows the SRS of the IAR. Previous attempts to verify the contribution of lightning at various distances to the excitation of the SRS of the IAR were hampered by limited access to global lightning data. Our analysis has verified definitively that the echo-pulse IAR signature seen in magnetometer data is a result of lightning excitation at distances ranging from 0 to 10,000 km. Nearby lightning, within 2000 km of the magnetometer station, results in a larger amplitude response, however, the number of strikes at distances between 2000-10,000 km from the magnetometer is much greater and thus provide a significant contribution. The propagation time of the electromagnetic pulse emitted from the lightning strike is near the speed of light, as expected.

Future work is required to determine the source of the constant offset of the propagation time. The most significant factor contributing to the time offset is most likely related to our timing the electromagnetic pulse arrival time using the time of the peak amplitude in the pulse. The group and phase velocity characteristics of the electromagnetic wave propagation in the Earth-ionosphere waveguide could be a contributing factor. The ICM instrument response could also be a factor. These results corroborate the calculated re-

sponse in Figure 7 of (*Surkov* et al., 2006) for modelled lightning strikes at distances from 0 to 10,000 km. Ultimately, we have shown that the electromagnetic pulse from lightning strikes between 0-10,000 km excites Alfvén waves along its path as it is ducted within the Earth-ionosphere cavity at speeds close to the speed of light. Local as well as non-local lightning strike pulses excite Alfvén waves that enter the IAR, reflect and produce an echo signature defined by the local characteristics of the IAR at the measuring magnetometer. This is further evidence pointing to the existence of coupling between terrestrial and space weather, involving lightning across the world which is a critical component of the global electric circuit.

Chapter 6

Conclusions and Future work

The results presented in this thesis contribute to the development of a new paradigm in the domain of space physics research that describes a mechanism for coupling atmospheric physics and the global electric circuit with ionospheric and magnetospheric physics. Through the analysis of induction coil magnetometer data from the Canadian Array for Real-time Investigations of Magnetic Activity together with lightning occurrence data from the World Wide Lightning Location Network, we demonstrated that lightning strikes around the globe transfer energy across the ionosphere, exciting the ionospheric Alfvén resonator (IAR) when the top of the resonator is strongly reflective, and potentially leaking energy into the magnetosphere when it is not. These findings are detailed in Chapters 4 and 5 of this thesis, and augmented by additional material presented in Appendix B and D.

Chapter 4 presented definitive evidence for lightning excitation of Alfvén waves in the ionospheric Alfvén resonator. Electromagnetic waves, excited by lightning strikes and propagating in the Earth-Ionosphere waveguide can perturb the ionosphere and create Alfvén waves that travel up into the IAR. Figure (6.1) provides a schematic illustration of this phenomenon. Combining the magnetometer data with lightning occurrence data greatly simplified the identification of the characteristic pulse-echo signals corresponding to an initial magnetic pulse excited by lightning followed by a second signal arriving from a reflection from the top boundary of the ionospheric Alfvén resonator. Our results further demonstrate that individual strikes provide a rather continuous

- if pulsed - excitation mechanism which drives Alfvén waves inside the cavity of the ionospheric Alfvén resonator.
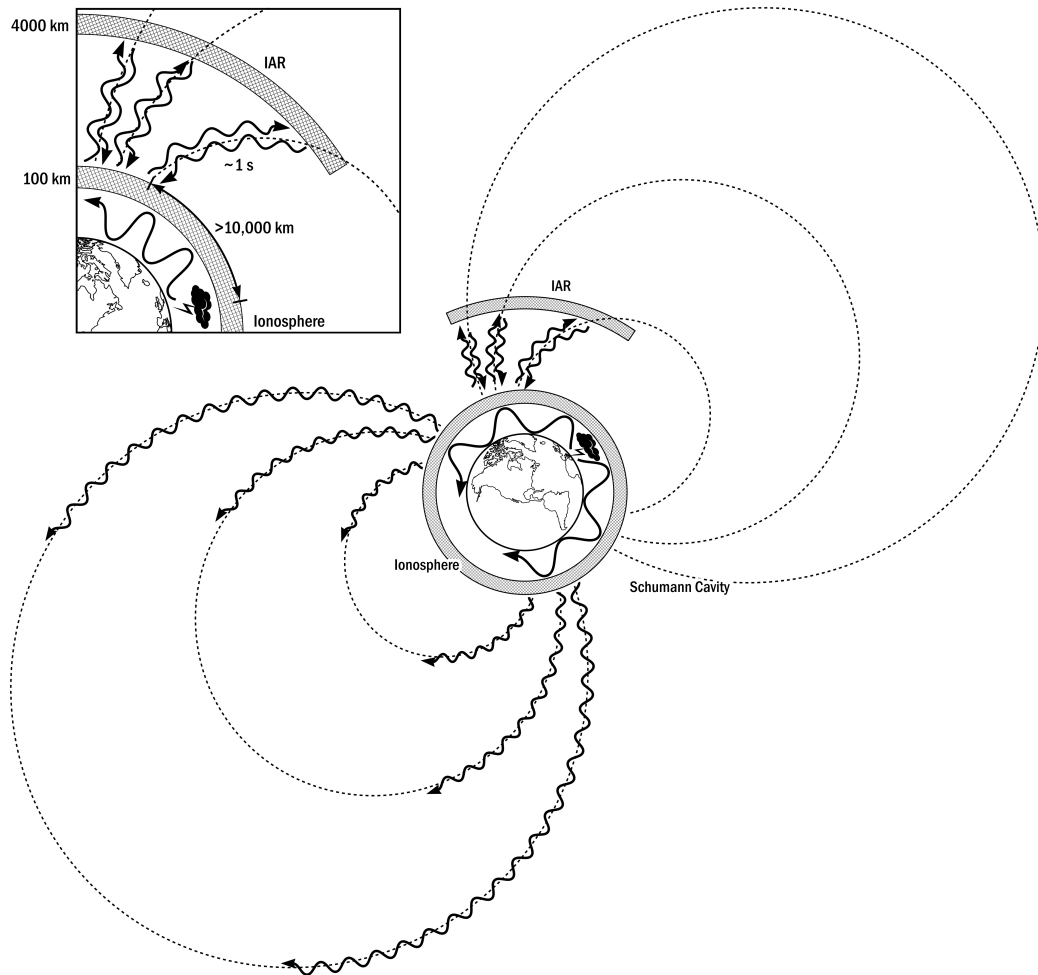
Figure 6.1: A schematic showing the lightning excitation of the ionospheric Alfvén resonator. See text for more details. Credit: Andy Kale.

Chapter 5 demonstrated that ionospheric Alfvén resonator excitation due to lightning is not limited to local lightning within a range of 2000 km, but also allows for non-local lightning - over 8000 km away - to provide the excitation. Our observations support a explanation based on a physical mechanism whereby lightning energy is first ducted as a electromagnetic wave in the Earth-Ionosphere waveguide, even over great distances, at speeds nearing the speed of light, exciting as it propagates, Alfvén waves which travel upwards from the ionosphere into the IAR. This is also illustrated in Figure (6.1).

Our results highlight the importance of studying the impact of atmospheric weather systems, specifically lightning activity and the global electric circuit, on space weather systems in the ionosphere and the magnetosphere. Significant advances as presented in this thesis were made due to access to global lightning data from WWLLN, which was not used in previous work by other researchers (e.g., *Schekotov* et al., 2011). Access to lightning occurrence datasets is critical to building on our work and continuing to improve the analysis and explore the physical processes by which lightning energy escapes into the ionosphere and magnetosphere.

The pulse-echo signatures associated with lightning strike excitation of the Alfvén waves inside the ionospheric Alfvén resonator exhibit a wide variety of characteristics. Explanations for some of these distinct features have been proposed here. However more work is needed to further characterise the nature of lightning excited modes in the IAR. For example, Figure (6.2) presents a case study of the correlation of the pulse-echo signals generated by the superposed epoch analysis to the spectral resonance structures of the IAR in the power spectral density plot derived from the time domain data. The reciprocal of the time delay, dt, between the initial magnetic pulse triggered by a lightning strike and the first reflection from the upper boundary of the ionospheric Alfvén resonator - found using the MATLAB *findpeaks* function - provides a data point for time of flight, from which an estimate can be made of the fundamental frequency of the IAR cavity, f_A.

The top panel of Figure (6.2) shows the solution curves for model IAR harmonic solutions for half-integer ($\Phi = 0.5$) and integer ($\Phi = 1$) harmonics of f_A (see Equation 2.27 in chapter 2) in the time intervals 4-11UT for the fundamental frequency (n=0) and the subsequent 8 harmonics (n=1,2,...8). In this event, the half-integer ($\Phi = 0.5$) harmonics correspond most closely to the power peaks in the spectral resonance structure, and the integer ($\Phi = 1$) harmonics correspond most closely to the spectral resonance structure power minima, though this overlap worsens as the harmonic number increases. As discussed in section 2.3, harmonic modes form in the resonating cavity, creating the spectral resonance structures seen in the spectral density plots. The
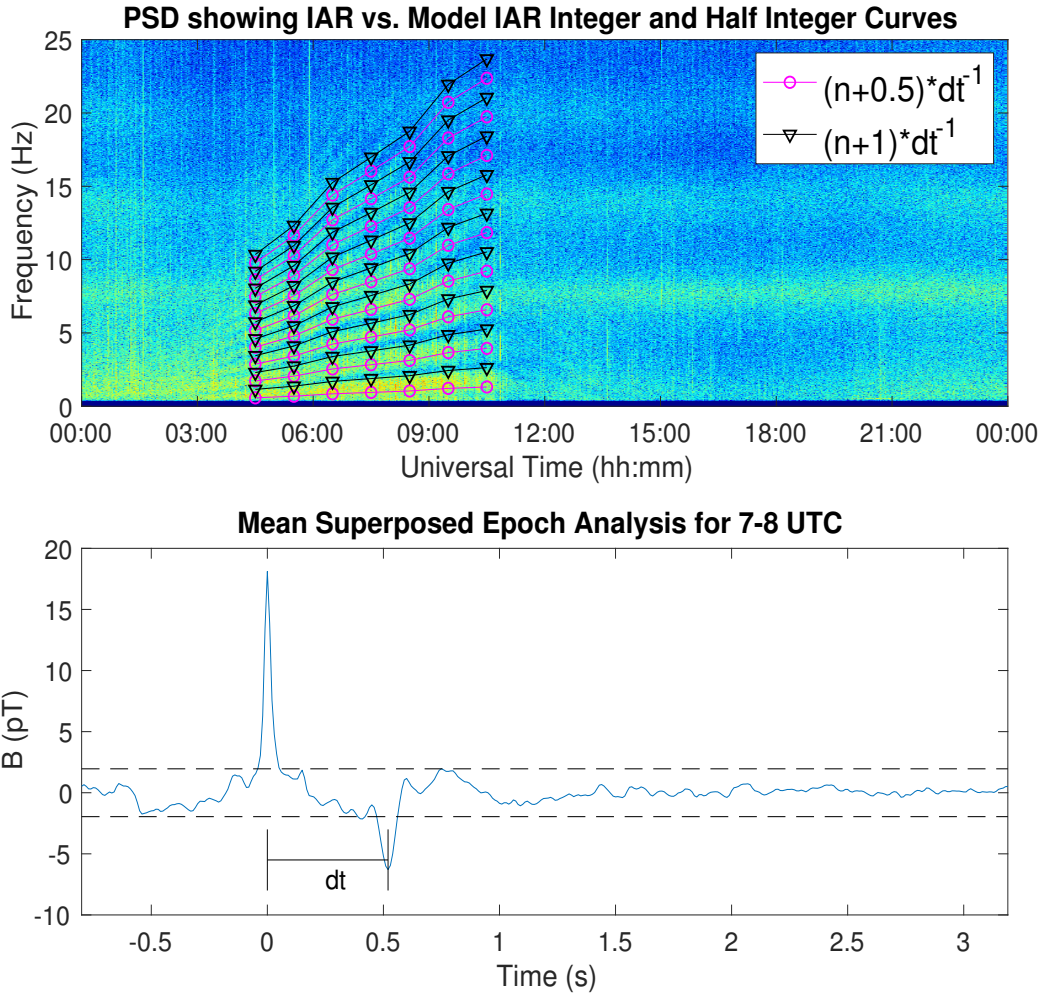
Figure 6.2: A case study of the connection between lightning excited IAR pulse-echo signals, generated by the superposed epoch analysis, to the spectral resonance structures observed using magnetometer data from Ministik Lake on August 24, 2009. (Top) 24-hour power spectral density plot of H-component (colour scaled). (Bottom) Time delay, dt, between initial lightning associated magnetic pulse and IAR echo for SEA for 7-8 UT. See text for more details.

frequencies of these harmonics, with respect to the fundamental frequency, depend on whether the fundamental mode is quarter-wave (n+0.5) or half-wave (n+1), as described by Equation (2.27) and both are overplotted in the top panel. This is an interesting area for future work. *Fedorov* et al. (2014) proposed this correlation could be tied to the polarity of the IAR echo, such that echos with the same polarity as the lightning triggered initial magnetic pulse result in the integer ($\Phi = 1$) harmonics corresponding to SRS power maxima

and half-integer ($\Phi = 0.5$) harmonics corresponding to SRS power minima. Conversely, echos with opposite polarity to the initial lightning triggered magnetic pulse result in the reverse, e.g., half-integer ($\Phi = 0.5$) harmonics corresponding to SRS power maxima and integer ($\Phi = 1$) harmonics corresponding to SRS power maxima.

This relationship can be further studied by building upon the results presented in this thesis. Doing so will shed more light on the detailed characteristics of the coupled atmosphere-ionosphere-magnetosphere system. For instance, *Hebden* et al. (2005) proposed that the conductivity of the lower boundary of the ionospheric Alfvén resonator determines the mode characteristics of standing waves inside the cavity,either being defined by a nodal or anti-nodal lower boundayr condition depending upon the conductivity. Similarly, the variation in echo polarity relative to the initial lightning related magnetic pulse polarity could be linked to the boundary conditions and nature of the modes in the cavity, and thus the conductivity of the lower boundary. This hypothesis could be tested by comparing the magnetic pulse-echo signatures identified with the analysis in this thesis to ionospheric conductivity models and experimental data, perhaps including that from the ionosondes (e.g., *Parent* et al., 2010).

Analysing the ratio of the magnitude of the echo to the initial pulse could also provide further insights about the conditions in the ionosphere. A lower ratio, corresponding to a lower echo magnitude, could point to lower reflection at the upper boundary, perhaps suggesting a larger fraction of the incident Alfvén wave energy is leaking into the magnetosphere. Another interesting characteristic, especially evident in the Schumann resonance signature in Figure 3.5, is the presence of fluctuations before the main pulse in the superposed epoch analysis. This could be due to the wave packet nature of the electromagnetic disturbance excited by lightning. However, the SEA magnetic pulse-echo signatures associated with the IAR do not exhibit this characteristic. Clearly this is worth further study. The delayed arrival of the main pulse in the magnetometer data will also be affected by the instrument response time, as well as dispersion in the Earth-ionosphere waveguide, which have not

been incorporated into the analysis thus far.

Further improvements to the analysis code could also be made with respect to the lightning matching and event rejection criteria. As noted in sections 3.3.3 and 3.3.4, the current version of the code disregards many potentially valid events due to the thresholding and timing criteria, which can result in many cases where the lightning and its corresponding magnetic pulse are rejected. One immediate improvement could be to implement timing and threshold criteria that selects the best match rather than rejecting the entire event.

Overall, the excitation of the ionospheric Alfvén resonator by lightning has been an important research topic since it was first theoretically proposed in 1990 (*Belyaev* et al., 1990). The results of this thesis experimentally demonstrate the validity of the hypothesis that lightning can act as a driver for Alfvén waves in the IAR. The results only begin to elucidate the details of the processes through which lightning and the fair weather global electric circuit couple to the ionospheric Alfvén resonator. Our results show very clearly that they are coupled and this has important implications for atmospheric, ionospheric, and magnetospheric physics and potentially for space weather impacts on the Earth's climate system.

References

Abreu, D., D. Chandan, R. H. Holzworth, and K. Strong (2010). "A Performance Assessment of the World Wide Lightning Location Network (WWLLN) via Comparison with the Canadian Lightning Detection Network (CLDN)." In: *Atmospheric Measurement Techniques* 3.4, pp. 1143–1153. ISSN: 1867-1381. DOI: `https://doi.org/10.5194/amt-3-1143-2010`. URL: `https://www.atmos-meas-tech.net/3/1143/2010/amt-3-1143-2010.html` (visited on 12/30/2018).   29

Baker, W. G. and David Forbes Martyn (1953). "Electric Currents in the Ionosphere - The Conductivity." In: *Phil. Trans. R. Soc. Lond. A* 246.913, pp. 281–294. ISSN: 0080-4614, 2054-0272. DOI: `10.1098/rsta.1953.0016`. URL: `http://rsta.royalsocietypublishing.org/content/246/913/281` (visited on 11/21/2018).   10, 11

Barr, R., D. Llanwyn Jones, and C. J. Rodger (2000). "ELF and VLF Radio Waves." In: *Journal of Atmospheric and Solar-Terrestrial Physics* 62.17, pp. 1689–1718. ISSN: 1364-6826. DOI: `10.1016/S1364-6826(00)00121-8`. URL: `http://www.sciencedirect.com/science/article/pii/S1364682600001218`.   12

Baumjohann, Wolfgang and Rudolf A Treumann (1996). *Basic Space Plasma Physics*. PUBLISHED BY IMPERIAL COLLEGE PRESS AND DISTRIBUTED BY WORLD SCIENTIFIC PUBLISHING CO. URL: `https://www.worldscientific.com/doi/abs/10.1142/p015`.   4–6, 8, 9, 15, 17

Belyaev, P.P., S.V. Polyakov, E. N. Ermakova, and S. V. Isaev (2000). "Solar Cycle Variations in the Ionospheric Alfven Resonator 1985–1995." In: *Journal of Atmospheric and Solar-Terrestrial Physics* 62.4, pp. 239–248. ISSN: 1364-6826. DOI: `10.1016/S1364-6826(00)00009-2`. URL: `http://www.sciencedirect.com/science/article/pii/S1364682600000092`.   24

Belyaev, P.P., S.V. Polyakov, V. O Rapoport, and V. Yu Trakhtengerts (1990). "The Ionospheric Alfvén Resonator." In: *Journal of Atmospheric and Terrestrial Physics* 52.9, pp. 781–788. ISSN: 0021-9169. DOI: `10.1016/0021-9169(90)90010-K`. URL: `http://www.sciencedirect.com/science/article/pii/002191699090010K`.   23–25, 46, 47, 60, 81

Bering, E. A. (1995). "The Global Circuit: Global Thermometer, Weather by-Product or Climatic Modulator?" In: *Reviews of Geophysics* 33.S2, pp. 845–862. ISSN: 1944-9208. DOI: `10.1029/95RG00549`. URL: `http://`

onlinelibrary.wiley.com/doi/10.1029/95RG00549/abstract (visited on 11/22/2016).   12, 13, 40, 47

Bering, Edgar A., Arthur A. Few, and James R. Benbrook (2008). "The Global Electric Circuit." In: *Physics Today* 51.10, pp. 24–30. ISSN: 0031-9228, 1945-0699. DOI: 10.1063/1.882422. URL: http://scitation.aip.org/content/aip/magazine/physicstoday/article/51/10/10.1063/1.882422 (visited on 11/22/2016).   12

Bösinger, T., C. Haldoupis, P. P. Belyaev, M. N. Yakunin, N. V. Semenova, A. G. Demekhov, and V. Angelopoulos (2002). "Spectral Properties of the Ionospheric Alfvén Resonator Observed at a Low-Latitude Station (L = 1.3)." In: *Journal of Geophysical Research: Space Physics* 107.A10, p. 1281. ISSN: 2156-2202. DOI: 10.1029/2001JA005076. URL: http://onlinelibrary.wiley.com/doi/10.1029/2001JA005076/abstract.   25, 46

Cummins, K. L. and M. J. Murphy (2009). "An Overview of Lightning Locating Systems: History, Techniques, and Data Uses, With an In-Depth Look at the U.S. NLDN." In: *IEEE Transactions on Electromagnetic Compatibility* 51.3, pp. 499–518. ISSN: 0018-9375. DOI: 10.1109/TEMC.2009.2023450.   13, 14

Dungey, J. W. (1961). "Interplanetary Magnetic Field and the Auroral Zones." In: *Physical Review Letters* 6.2, pp. 47–48. DOI: 10.1103/PhysRevLett.6.47. URL: https://link.aps.org/doi/10.1103/PhysRevLett.6.47.   7

Eilers, Paul H. C. and Jelle J. Goeman (2004). *Enhancing Scatterplots with Smoothed Densities.*   44

Fedorov, E., A. Schekotov, Y. Hobara, R. Nakamura, N. Yagova, and M. Hayakawa (2014). "The Origin of Spectral Resonance Structures of the Ionospheric Alfvén Resonator. Single High-Altitude Reflection or Resonant Cavity Excitation?" In: *Journal of Geophysical Research: Space Physics* 119.4, pp. 3117–3129. ISSN: 2169-9402. DOI: 10.1002/2013JA019428. URL: http://onlinelibrary.wiley.com/doi/10.1002/2013JA019428/abstract (visited on 11/02/2016).   25, 47, 64, 79

Fedorov, E., A. Schekotov, O. A. Molchanov, M. Hayakawa, V. V. Surkov, and V. A. Gladichev (2006). "An Energy Source for the Mid-Latitude IAR: World Thunderstorm Centers, Nearby Discharges or Neutral Wind Fluctuations?" In: *Physics and Chemistry of the Earth, Parts A/B/C*. Recent Progress in Seismo Electromagnetics and Related Phenomena 31.4–9, pp. 462–468. ISSN: 1474-7065. DOI: 10.1016/j.pce.2006.02.001. URL: http://www.sciencedirect.com/science/article/pii/S1474706506000295 (visited on 11/02/2016).   25, 46

Field, E. C. and C. Greifinger (1965). "Transmission of Geomagnetic Micropulsations through the Ionosphere and Lower Exosphere." In: *Journal of Geophysical Research* 70.19, pp. 4885–4899. ISSN: 2156-2202. DOI: 10.1029/JZ070i019p04885. URL: https://agupubs-onlinelibrary-wiley-com.login.ezproxy.library.ualberta.ca/doi/abs/10.1029/JZ070i019p04885.   22

Frandsen, A. M. A., R. E. Holzer, and E. J. Smith (1969). "OGO Search Coil Magnetometer Experiments." In: *IEEE Transactions on Geoscience Electronics* 7.2, pp. 61–74. ISSN: 0018-9413. DOI: 10.1109/TGE.1969.271324.   27

Hargreaves, John Keith (1992). *The Solar-Terrestrial Environment: An Introduction to Geospace-the Science of the Terrestrial Upper Atmosphere, Ionosphere, and Magnetosphere.* Cambridge University Press.   9–11

Hebden, S. R., T. R. Robinson, D. M. Wright, T. Yeoman, T. Raita, and T. Bösinger (2005). "A Quantitative Analysis of the Diurnal Evolution of Ionospheric Alfvén Resonator Magnetic Resonance Features and Calculation of Changing IAR Parameters." In: *Annales Geophysicae* 23.5, pp. 1711–1721. URL: https://hal.archives-ouvertes.fr/hal-00317823.   21–24, 80

Hutchins, M. L., R. H. Holzworth, J. B. Brundell, and C. J. Rodger (2012). "Relative Detection Efficiency of the World Wide Lightning Location Network." In: *Radio Science* 47.6. ISSN: 1944-799X. DOI: 10.1029/2012RS005049. URL: http://agupubs.onlinelibrary.wiley.com/doi/abs/10.1029/2012RS005049 (visited on 11/09/2018).   25, 26, 28, 48

Iijima, T. and T. A. Potemra (1978). "Large-Scale Characteristics of Field-Aligned Currents Associated with Substorms." In: *Journal of Geophysical Research: Space Physics* 83.A2, pp. 599–615. ISSN: 2156-2202. DOI: 10.1029/JA083iA02p00599. URL: https://agupubs-onlinelibrary-wiley-com.login.ezproxy.library.ualberta.ca/doi/abs/10.1029/JA083iA02p00599.   7, 8

Kelvin, William Thomson Baron (1860). *On Atmospheric Electricity.*   12

Knudsen, D. J., M. C. Kelley, and J. F. Vickrey (1992). "Alfvén Waves in the Auroral Ionosphere: A Numerical Model Compared with Measurements." In: *Journal of Geophysical Research: Space Physics* 97.A1, pp. 77–90. ISSN: 2156-2202. DOI: 10.1029/91JA02300. URL: https://agupubs-onlinelibrary-wiley-com.login.ezproxy.library.ualberta.ca/doi/abs/10.1029/91JA02300.   23

Kulsrud, Russell M (1980). *MHD Description of Plasma.* Princeton University.   16

Lysak (1993). "Generalized Model of the Ionospheric Alfvén Resonator." In: *Auroral Plasma Dynamics* 80, pp. 121–128.   23

Lysak, R.L. (1991). "Feedback Instability of the Ionospheric Resonant Cavity." In: *Journal of Geophysical Research: Space Physics* 96.A2, pp. 1553–1568. ISSN: 2156-2202. DOI: 10.1029/90JA02154. URL: https://agupubs-onlinelibrary-wiley-com.login.ezproxy.library.ualberta.ca/doi/abs/10.1029/90JA02154.   20, 21, 23, 24, 46

Mann, I. R., D. K. Milling, I. J. Rae, L. G. Ozeke, A. Kale, Z. C. Kale, K. R. Murphy, A. Parent, M. Usanova, D. M. Pahud, E.-A. Lee, V. Amalraj, D. D. Wallis, V. Angelopoulos, K.-H. Glassmeier, C. T. Russell, H.-U. Auster, and H. J. Singer (2008). "The Upgraded CARISMA Magnetometer Array in the THEMIS Era." In: *Space Science Reviews* 141.1-4, pp. 413–451. ISSN: 0038-6308, 1572-9672. DOI: 10.1007/s11214-008-9457-6. URL:

http://link.springer.com/article/10.1007/s11214-008-9457-6
(visited on 11/22/2016).   25, 26, 48, 49

Parent, Adrienne, Ian R. Mann, and I. Jonathan Rae (2010). "Effects of
Substorm Dynamics on Magnetic Signatures of the Ionospheric Alfvén
Resonator." In: *Journal of Geophysical Research: Space Physics* 115.A2,
A02312. ISSN: 2156-2202. DOI: 10.1029/2009JA014673. URL: http://
onlinelibrary.wiley.com/doi/10.1029/2009JA014673/abstract (vis-
ited on 11/02/2016).   61, 80

Parker, Eugene (1959). "Extension of the Solar Corona into Interplanetary
Space." In: *Journal of Geophysical Research* 64.11, pp. 1675–1681. ISSN:
2156-2202. DOI: 10.1029/JZ064i011p01675. URL: https://agupubs-
onlinelibrary-wiley-com.login.ezproxy.library.ualberta.ca/
doi/abs/10.1029/JZ064i011p01675.   3

Polyakov, S. V. (1976). "On Properties of an Ionospheric Alfven Resonator."
In: *Symposium KAPG on Solar-Terrestrial Physics, Moscow, 1976. Nauka*
3, pp. 72–73. URL: https://ci.nii.ac.jp/naid/10016219826/en/.   1, 22, 46

Ram, S. Tulasi, S.-Y. Su, C. H. Liu, B. W. Reinisch, and Lee-Anne McKinnell
(2009). "Topside Ionospheric Effective Scale Heights (HT) Derived with
ROCSAT-1 and Ground-Based Ionosonde Observations at Equatorial and
Midlatitude Stations." In: *Journal of Geophysical Research: Space Physics*
114.A10. ISSN: 2156-2202. DOI: 10.1029/2009JA014485. URL: http://
agupubs.onlinelibrary.wiley.com/doi/abs/10.1029/2009JA014485
(visited on 11/21/2018).   20

Schekotov, A., V. Pilipenko, K. Shiokawa, and E. Fedorov (2011). "ULF Impul-
sive Magnetic Response at Mid-Latitudes to Lightning Activity." In: *Earth,
Planets and Space* 63.2, pp. 119–128. ISSN: 1880-5981. DOI: 10.5047/eps.
2010.12.009. URL: https://doi.org/10.5047/eps.2010.12.009.   25, 46, 60, 63, 64, 78

Schumann, WO (1952). "On the Free Oscillations of a Conducting Sphere
Which Is Surrounded by an Air Layer and an Ionosphere Shell." In: *Z.
Natutforschaftung* 7, pp. 149–154.   13

Surkov, V. V., M. Hayakawa, A. Y. Schekotov, E. N. Fedorov, and O. A.
Molchanov (2006). "Ionospheric Alfvén Resonator Excitation Due to Nearby
Thunderstorms." In: *Journal of Geophysical Research: Space Physics* 111.A1,
A01303. ISSN: 2156-2202. DOI: 10.1029/2005JA011320. URL: http://
onlinelibrary.wiley.com/doi/10.1029/2005JA011320/abstract (vis-
ited on 11/02/2016).   25, 63, 64, 75

Surkov, V. V., O. A. Molchanov, M. Hayakawa, and E. N. Fedorov (2005). "Ex-
citation of the Ionospheric Resonance Cavity by Thunderstorms." In: *Jour-
nal of Geophysical Research: Space Physics* 110.A4, A04308. ISSN: 2156-
2202. DOI: 10.1029/2004JA010850. URL: http://onlinelibrary.wiley.
com/doi/10.1029/2004JA010850/abstract.   46

Trakhtengerts, V. Yu. and A. Ya. Feldstein (1991). "Turbulent Alfven Bound-
ary Layer in the Polar Ionosphere: 1. Excitation Conditions and Energet-
ics." In: *Journal of Geophysical Research: Space Physics* 96.A11, pp. 19363–

19374. ISSN: 2156-2202. DOI: 10.1029/91JA00376. URL: http://onlinelibrary.wiley.com/doi/10.1029/91JA00376/abstract.   24, 46

Williams, Earle R. (1992). "The Schumann Resonance: A Global Tropical Thermometer." In: *Science* 256.5060, pp. 1184–1187. ISSN: 0036-8075, 1095-9203. DOI: 10.1126/science.256.5060.1184. pmid: 17795213. URL: http://science.sciencemag.org/content/256/5060/1184 (visited on 09/10/2018).   62, 63, 65

Yahnin, AG, NV Semenova, AA Ostapenko, Jorma Kangas, Jyrki Manninen, and T Turunen (2003). "Morphology of the Spectral Resonance Structure of the Electromagnetic Background Noise in the Range of 0.1-4 Hz at L= 5.2." In: *Annales Geophysicae* 21, pp. 779–786.   24

Yoshikawa, A. and M. Itonaga (2000). "The Nature of Reflection and Mode Conversion of MHD Waves in the Inductive Ionosphere: Multistep Mode Conversion between Divergent and Rotational Electric Fields." In: *Journal of Geophysical Research: Space Physics* 105.A5, pp. 10565–10584. ISSN: 2156-2202. DOI: 10.1029/1999JA000159. URL: http://agupubs.onlinelibrary.wiley.com/doi/abs/10.1029/1999JA000159 (visited on 11/21/2018).   11

Appendix A

WWLLN Data Readme

Dear WWLLN Hosts,

To unpack the compressed and tar'd files named AE2009.tgz use tar xzf AE2009.tgz to get the daily AE files.

The format of these files is similar to Afiles, with the addition of three extra parameters on each line the Energy in Joules, Energy uncertainty and Nstations used for energy:

The format for the AE files is:

YYYY/MM/DD, hh:mm:ss, lat, lon, resid, nstn, Energy (J), Energy uncertainty (J), nstn_energy

Where: Date/time in UTC

Lat, Lon in fractional degrees (geographic coordinated)

resid is the residual fit error in Microseconds (always ¡30)

nstn is the number of WWLLN stations participarting in the location fit

energy is the RMS energy (in Joules) of the stroke (from 1.3 ms waveform sampling between 7 and 18 kHz)

energy uncertainty (energy error of the fit in Joules)

nstn_eneregy is the subset of nstn stations between 1000 and 8000 km from the stroke whose energy data were used in the energy estimate.

Format of data files:

AE Files are ascii text files labeled with the date and time of the data such as

2012/4/23,00:00:00.149517, 26.5463, 135.4961, 13.2, 9, 2741.38, 332.49, 5

2012/4/23,00:00:00.834707, 10.7970, 125.8763, 06.2, 7, 1744.95, 131.47, 6

2012/4/23,00:00:00.943868, 19.4564, -070.9303, 17.2, 6, 298.00, 118.10, 4

2012/4/23,00:00:00.922768, 14.1879, -090.7451, 24.0, 16, 507.86, 136.14, 13

2012/4/23,00:00:00.943845, 19.3481, -070.9295, 16.4, 5, 212.37, 48.31, 4

2012/4/23,00:00:01.205949, 14.2636, -090.4189, 14.0, 11, 140.89, 33.33, 9

where (as above):

Date and time are in UTC

Lat, lon in Fractional Degrees

Resid is the residual fit error in micrfoseconds (always ¡ 30 microseconds)

Nsta is the number of WWLLN stations which detected the stroke (alway ¿=5)

Energy (J) - RMS energy from 7 to 18 kHz in 1.3 ms sample time

energy uncertainty (J)

nstn_energy - subset of Nsta within the range 1000 to 8000 km distant from strok and used for power estimate

In addition, every hour we determine the Relative Detection Efficiency for the entire globe, on a 5x5 degree or 1x1 degree grid. These deMaps are located in in matlab files. Each matlab file has 3 variables:

de_map - relative detection efficiency map in 5 bin

de_map_high - de_map that has been smoothed to 1 resolution

de_time - time of the 24 maps in matlab datenum format

The de_map file are centered so that the first entry, de_map(1,1,1), gives the detection efficiency for the bin that spans -180 E to -175 E, 85N to 90N for UTC hour 00:00 to 00:59.

The first index is increasing longitude (1 = -180 to -175, 2 = -175 to -170, etc) , the second index is decreasing latitude (1 = 90 to 85, 2 = 85 to 80, etc) and the third index is the UTC hour plus one (1 = 00:00 to 00:59, 2 = 01:00 to 01:59, etc).

As always, please contact me with any problems or requests. I am able to temporarily re-post data from previously in the year if you have lost something.

More Questions? Contact Prof. Robert Holzworth, Director of WWLLN, and Professor of Earth and Space Sciences, University of Washington, Box

351310, Seattle, WA 98195 (bobholz@uw.edu)

Appendix B

Chapter 4 Supplementary Materials

This appendix provides additional results in Figures B.1 to B.12, which provide the same analysis as Figures 4.1 to 4.3 in Chapter 4 for four stations on August 25, 2014. One important distinction is the high pass filter of the raw time series data. The figures presented here used a high pass cut-off of 0.84 Hz, whereas the data presented in Chapter 4 used 0.3 Hz. Due to time constraints, reproducing the results of this appendix with the high pass cut-off of 0.3 Hz was not possible, and is a relevant exercise for future work. The fundamental frequency of the SRS may be between 0.3 Hz and 0.84 Hz, and this would show in the superposed epoch analysis.

The four stations are Ministik Lake, Pinawa, Rabbit Lake, and Fort Churchill. The first figure for each station provides the power spectral density plot which shows the SRS of the IAR, the number of lightning strikes, number of initial magnetic pulses above the threshold σ_{quiet}, and the number of those initial magnetic pulses matched to lightning. The second figure for each station presents the mean signatures of the four 1-hour intervals with the cleanest IAR signatures - those occurring from 05 UT to 09 UT together with the spectra of the mean time domain superposed response, the median time domain superposed response, and the quartile time domain superposed responses. The time domain superposed responses for the mean, median, and quartiles themselves, from which the associated spectra the second figures are obtained, are shown in the third figure for each magnetometer station.
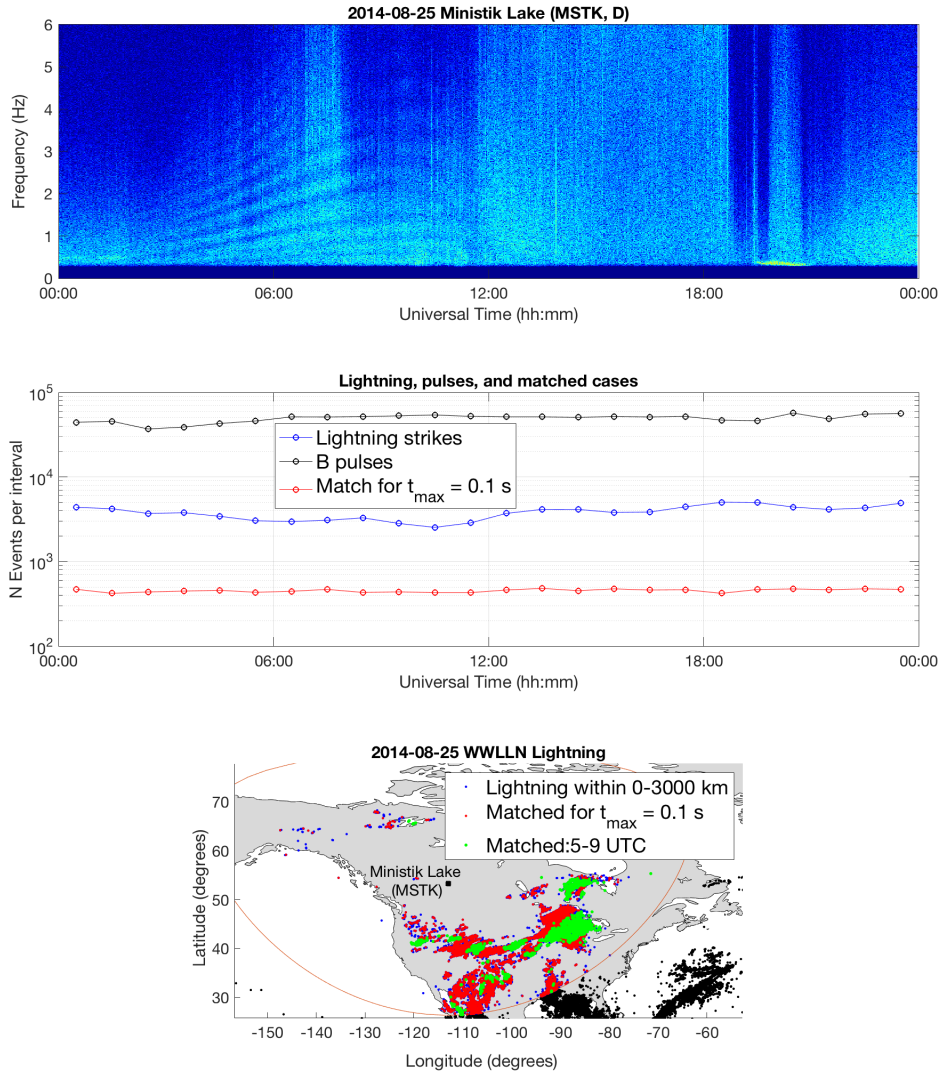
Figure B.1: A case study of lightning strikes matched to magnetic pulses in the Ministik Lake induction coil magnetometer data on August 25, 2014. (Top) The power spectral density plot of the D-component magnetic field data, showing the spectral resonance structures (SRS) of the ionospheric Alfvén resonator (IAR) from ~03-11 UT. (Middle) Log scale plot of the number of lightning strikes (blue) within 0-3000 km from the Ministik Lake magnetometer station for each UT hour, the number of magnetic pulses (black) with amplitudes above σ_{quiet}, and of those magnetic pulses the subset of ones that occur within 0.1 s after a lightning strike (red). (Bottom) A map showing the location of WWLLN lightning strikes relative to the Ministik Lake magnetometer station, where blue dots are lightning strikes that occurred within 0-3000 km but did not match to a magnetic pulse, red dots are lightning strikes that matched to magnetic pulses, and green dots are where the strikes matched to magnetic pulses when the IAR is most active, from 05-09 UT.
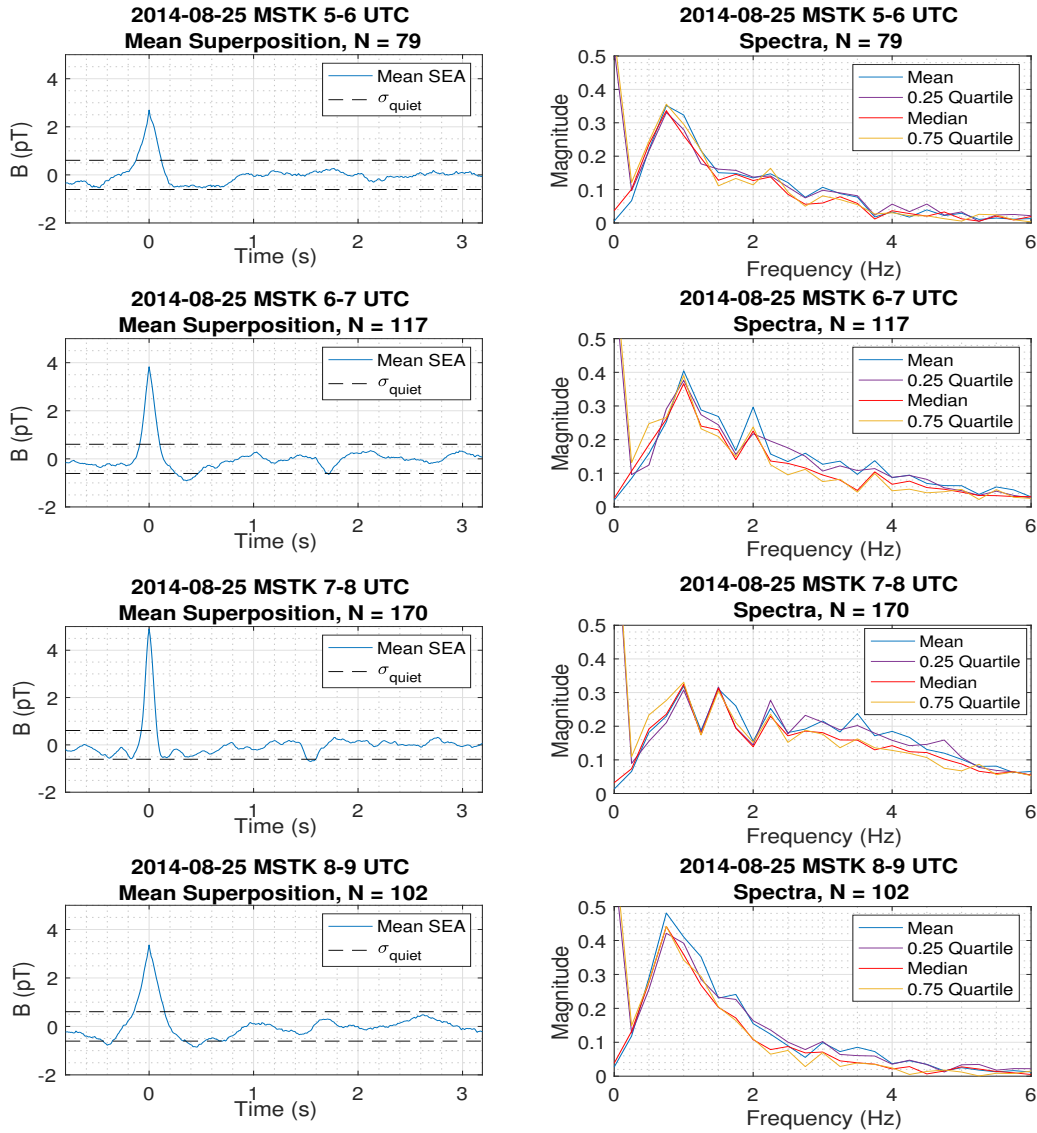
Figure B.2: Mean superposed epoch time series (left column) and spectra (right column) of data from the Ministik Lake magnetometer station matched to WWLLN lightning strikes for four 1-hour time intervals when the IAR is active, from 05-09 UT on August 25, 2014. All magnetic pulses were superposed with positive polarity at epoch time 0 seconds in each 4-second window, and the magnetic threshold of the initial pulse is set at quantile 0.95 above $\sigma_{quiet} = 0.6$ pT. The first echo from inside the IAR is clearly visible as a negative polarity pulse between T=1.5 s and T=2.5 s in each panel, for each hour from 05-09 UT, respectively. The accompanying spectra for 07-08 UT (third right) clearly shows the spectral resonance structures of the IAR, for the mean, median and quartiles in the superposed epoch time series. The number of events superposed, N, is above each panel.
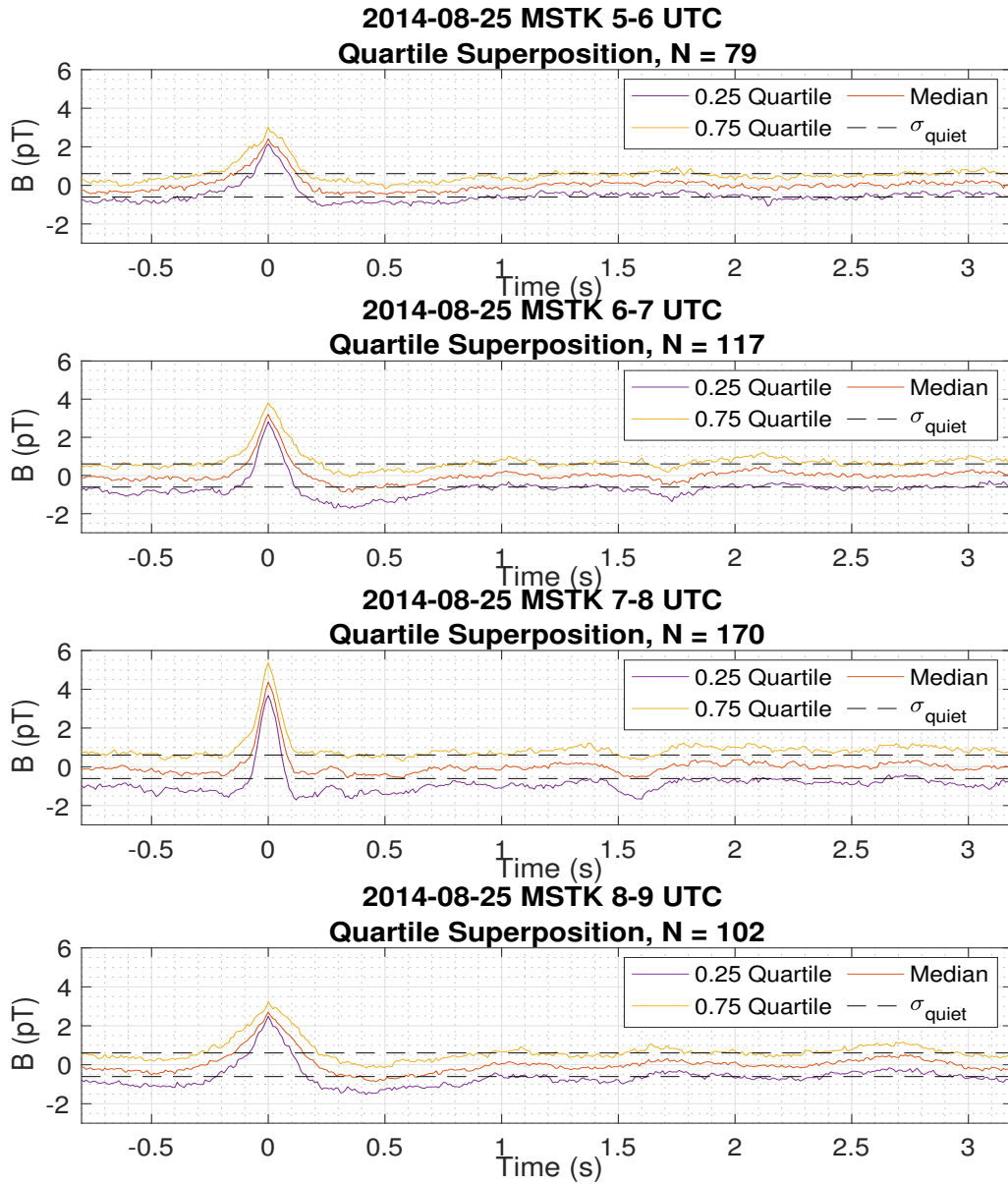
Figure B.3: Median and quartiles time series signals from the superposed epoch analysis of data from the Ministik Lake magnetometer station matched to WWLLN lightning strikes for four 1-hour time intervals when the IAR is active, from 05-09 UT on August 25, 2014. All initial lightning associated magnetic pulses were superposed with enforced positive polarity at superposed epoch 0 seconds in each 4-second window, and the initial magnetic pulse threshold was selected to be quantile 0.95 above $\sigma_{quiet} = 0.6$ pT. The first echo is visible as a negative polarity pulse between T=1.5 s and T=2.5 s for each hour from 05-09 UT, respectively. The number of events superposed, N, is above each panel.
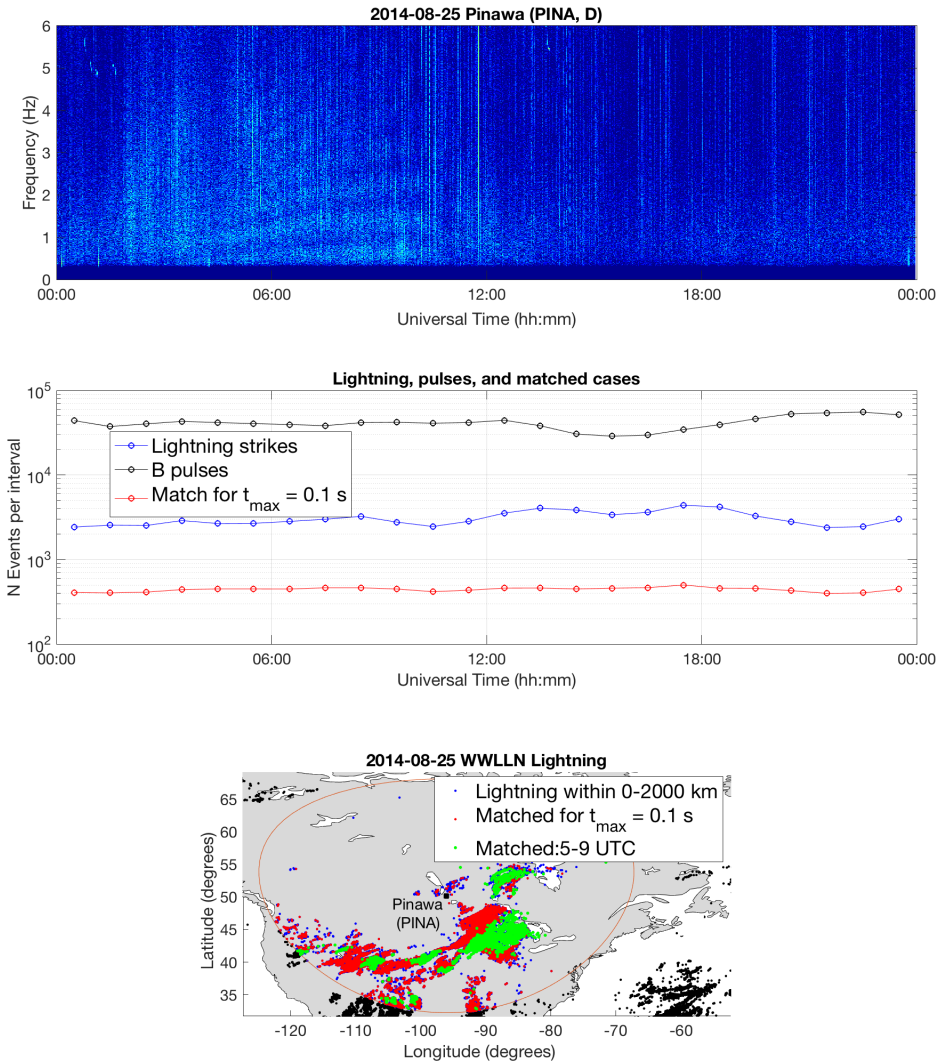
Figure B.4: A case study of lightning strikes matched to magnetic pulses in the Pinawa induction coil magnetometer data on August 25, 2014. (Top) The power spectral density plot of the D-component magnetic field data, showing the spectral resonance structures (SRS) of the ionospheric Alfvén resonator (IAR) from ∼04-10 UT. (Middle) Log scale plot of the number of lightning strikes (blue) within 0-2000 km from the Pinawa magnetometer station for each UT hour, the number of magnetic pulses (black) with amplitudes above σ_{quiet}, and of those magnetic pulses the subset of ones that occur within 0.1 s after a lightning strike (red). (Bottom) A map showing the location of WWLLN lightning strikes relative to the Pinawa magnetometer station, where blue dots are lightning strikes that occurred within 0-2000 km but did not match to a magnetic pulse, red dots are lightning strikes that matched to magnetic pulses, and green dots are where the strikes matched to magnetic pulses when the IAR is most active, from 05-09 UT.
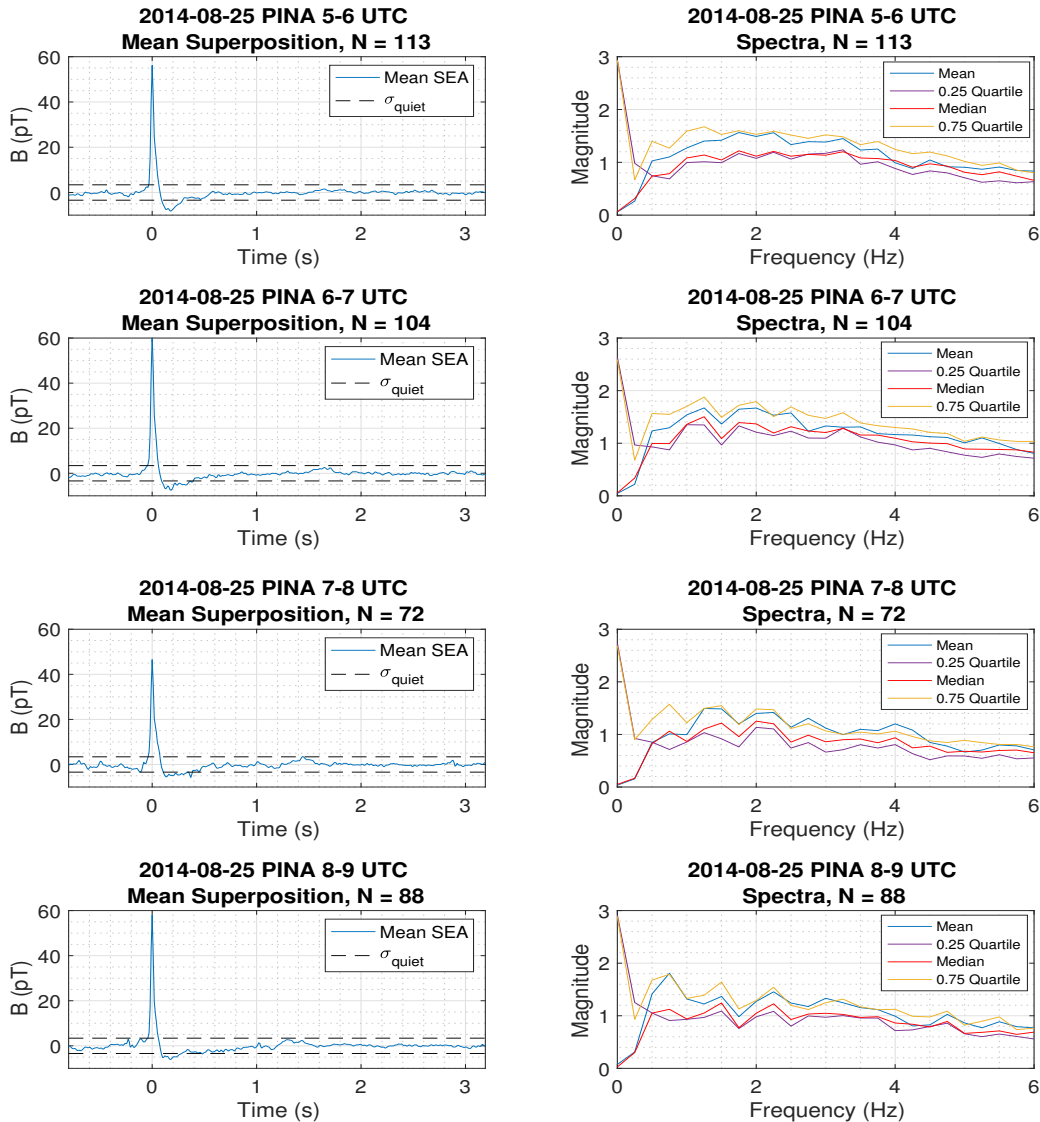
94

Figure B.5: Mean superposed epoch time series (left column) and spectra (right column) of data from the Pinawa magnetometer station matched to WWLLN lightning strikes for four 1-hour time intervals when the IAR is active, from 05-09 UT on August 25, 2014. All magnetic pulses were superposed with positive polarity at epoch time 0 seconds in each 4-second window, and the magnetic threshold of the initial pulse is set at quantile 0.992 above $\sigma_{quiet} = 3.4$ pT. The first echo from inside the IAR is clearly visible as a negative polarity pulse near T=1.5 s in each panel, for each hour from 05-09 UT, respectively. The accompanying spectra for 07-08 UT (third right) and 08-09 UT (bottom right) clearly show the spectral resonance structures of the IAR, for the mean, median and quartiles in the superposed epoch time series. The number of events superposed, N, is above each panel.
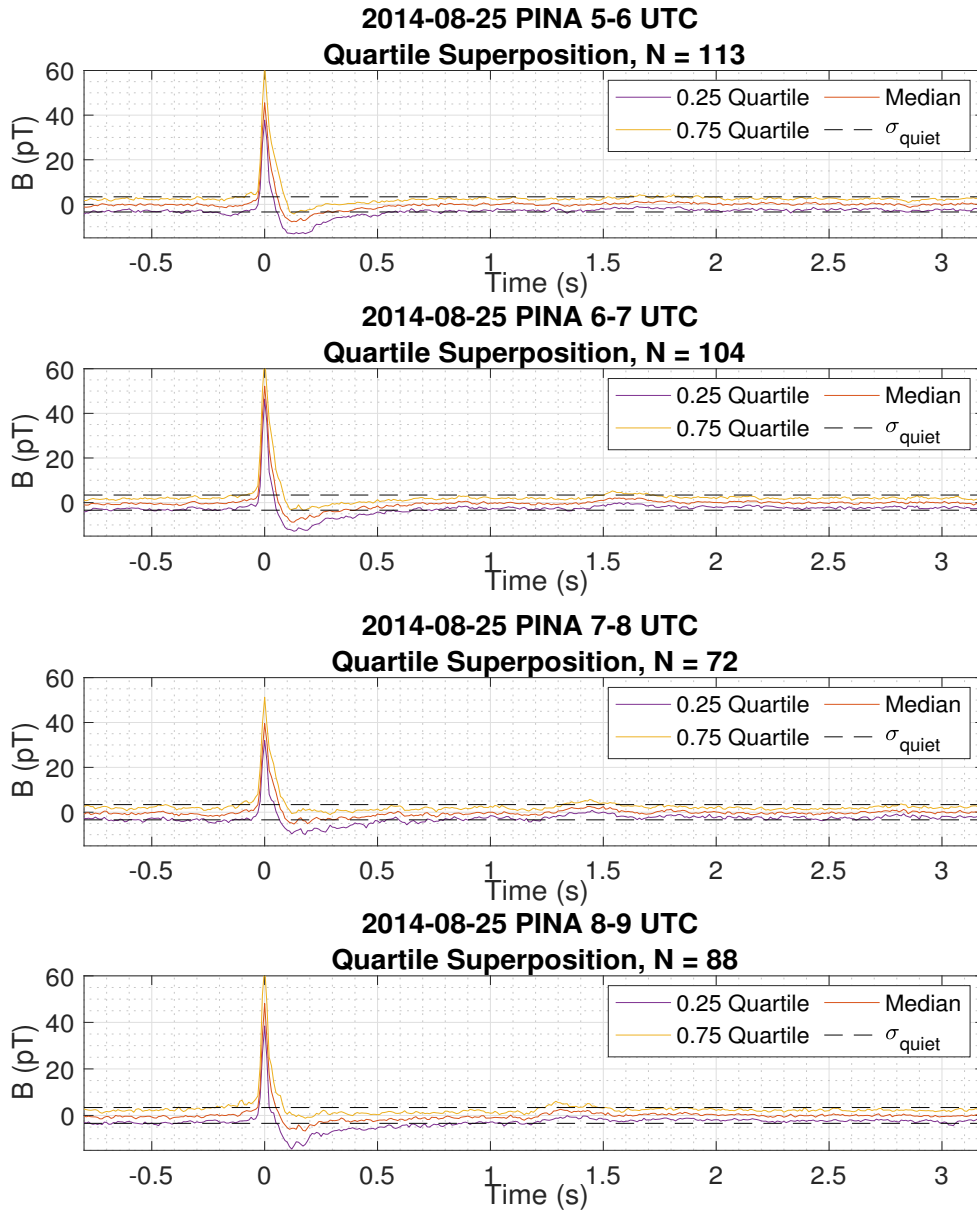
Figure B.6: Median and quartiles time series signals from the superposed epoch analysis of data from the Pinawa magnetometer station matched to WWLLN lightning strikes for four 1-hour time intervals when the IAR is active, from 05-09 UT on August 25, 2014. All initial lightning associated magnetic pulses were superposed with enforced positive polarity at superposed epoch 0 seconds in each 4-second window, and the initial magnetic pulse threshold was selected to be quantile 0.992 above $\sigma_{quiet} = 3.4$ pT. The first echo is clearly visible as a positive polarity pulse near T=1.5 s for each hour from 05-09 UT, respectively. However, the signal stays below σ_{quiet} indicating a weak reflection response. The number of events superposed, N, is above each panel.
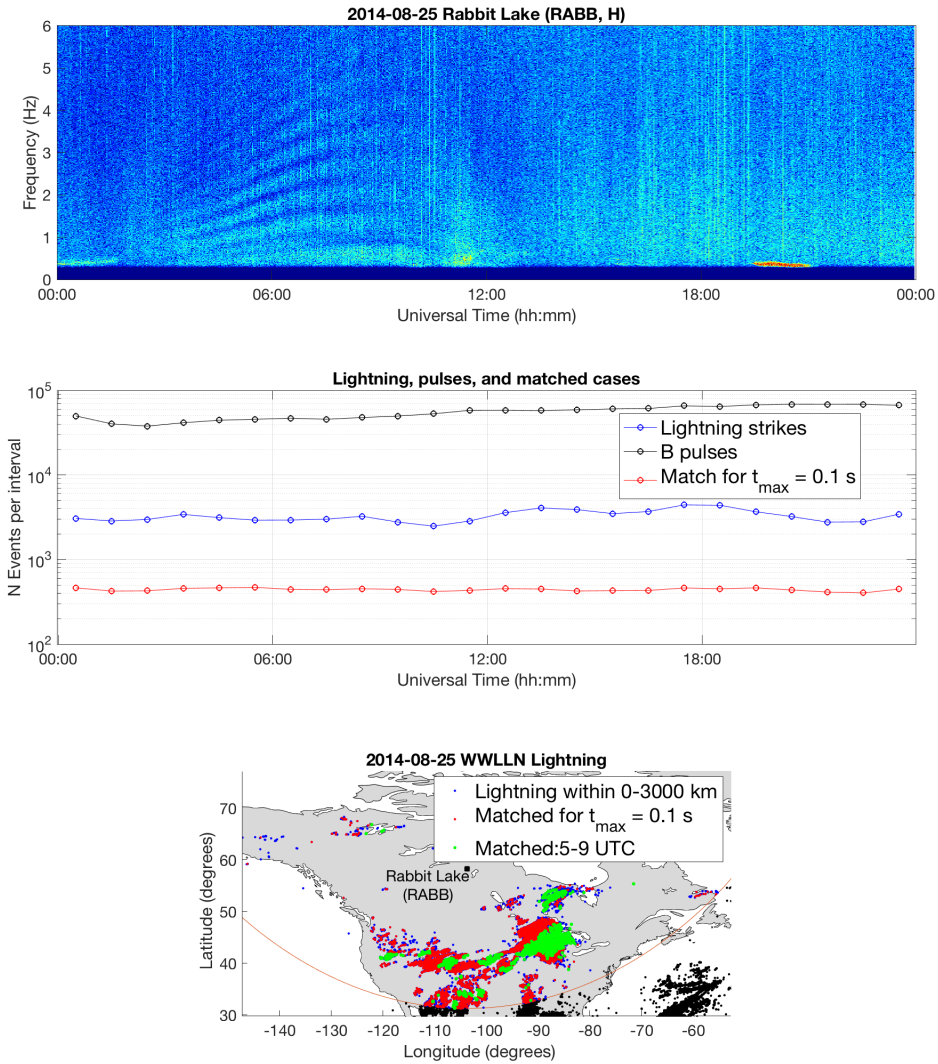
Figure B.7: A case study of lightning strikes matched to magnetic pulses in the Rabbit Lake induction coil magnetometer data on August 25, 2014. (Top) The power spectral density plot of the H-component magnetic field data, showing the spectral resonance structures (SRS) of the ionospheric Alfvén resonator (IAR) from ∼03-11 UT. (Middle) Log scale plot of the number of lightning strikes (blue) within 0-3000 km from the Rabbit Lake magnetometer station for each UT hour, the number of magnetic pulses (black) with amplitudes above σ_{quiet}, and of those magnetic pulses the subset of ones that occur within 0.1 s after a lightning strike (red). (Bottom) A map showing the location of WWLLN lightning strikes relative to the Rabbit Lake magnetometer station, where blue dots are lightning strikes that occurred within 0-3000 km but did not match to a magnetic pulse, red dots are lightning strikes that matched to magnetic pulses, and green dots are where the strikes matched to magnetic pulses when the IAR is most active, from 05-09 UT.
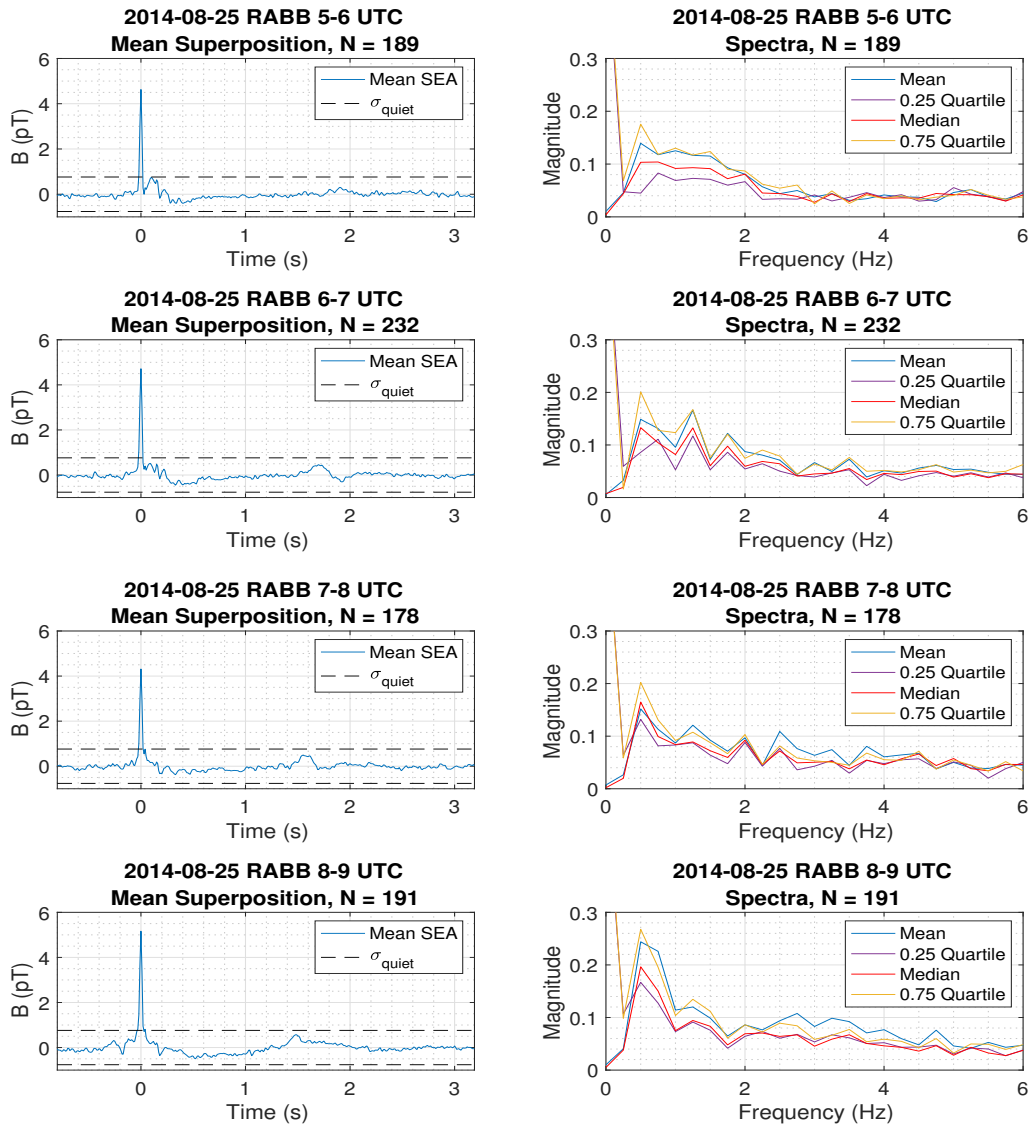
Figure B.8: Mean superposed epoch time series (left column) and spectra (right column) of data from the Rabbit Lake magnetometer station matched to WWLLN lightning strikes for four 1-hour time intervals when the IAR is active, from 05-09 UT on August 25, 2014. All magnetic pulses were superposed with positive polarity at epoch time 0 seconds in each 4-second window, and the magnetic threshold of the initial pulse is set at quantile 0.95 above $\sigma_{quiet} = 0.8$ pT. The first echo from inside the IAR is clearly visible as a negative polarity pulse between T=1.5 s and T=2 s in each panel, for each hour from 05-09 UT, respectively. However, the signal stays below σ_{quiet}, indicating a weak reflection response. The accompanying spectra for the three lower panels show the spectral resonance structures of the IAR, for the mean, median and quartiles in the superposed epoch time series. The number of events superposed, N, is above each panel.
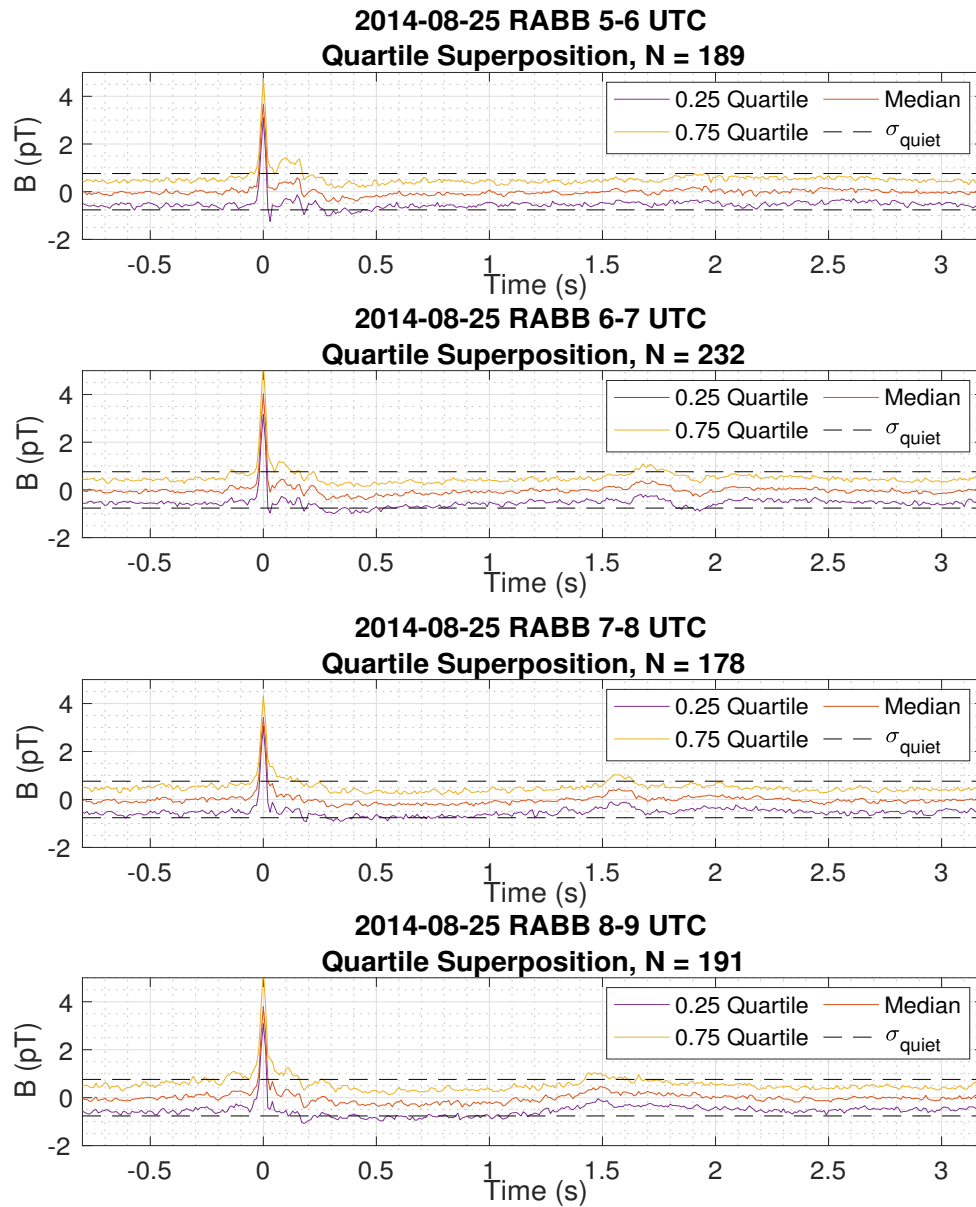
98

Figure B.9: Median and quartiles time series signals from the superposed epoch analysis of data from the Rabbit Lake magnetometer station matched to WWLLN lightning strikes for four 1-hour time intervals when the IAR is active, from 05-09 UT on August 25, 2014. All initial lightning associated magnetic pulses were superposed with enforced positive polarity at superposed epoch 0 seconds in each 4-second window, and the initial magnetic pulse threshold was selected to be quantile 0.95 above $\sigma_{quiet} = 0.8$ pT. The first echo is clearly visible as a positive polarity pulse between T=1.5 s and T=2 s for each hour from 05-09 UT, respectively. However, the signal stays below σ_{quiet} indicating a weak reflection response. The number of events superposed, N, is above each panel.
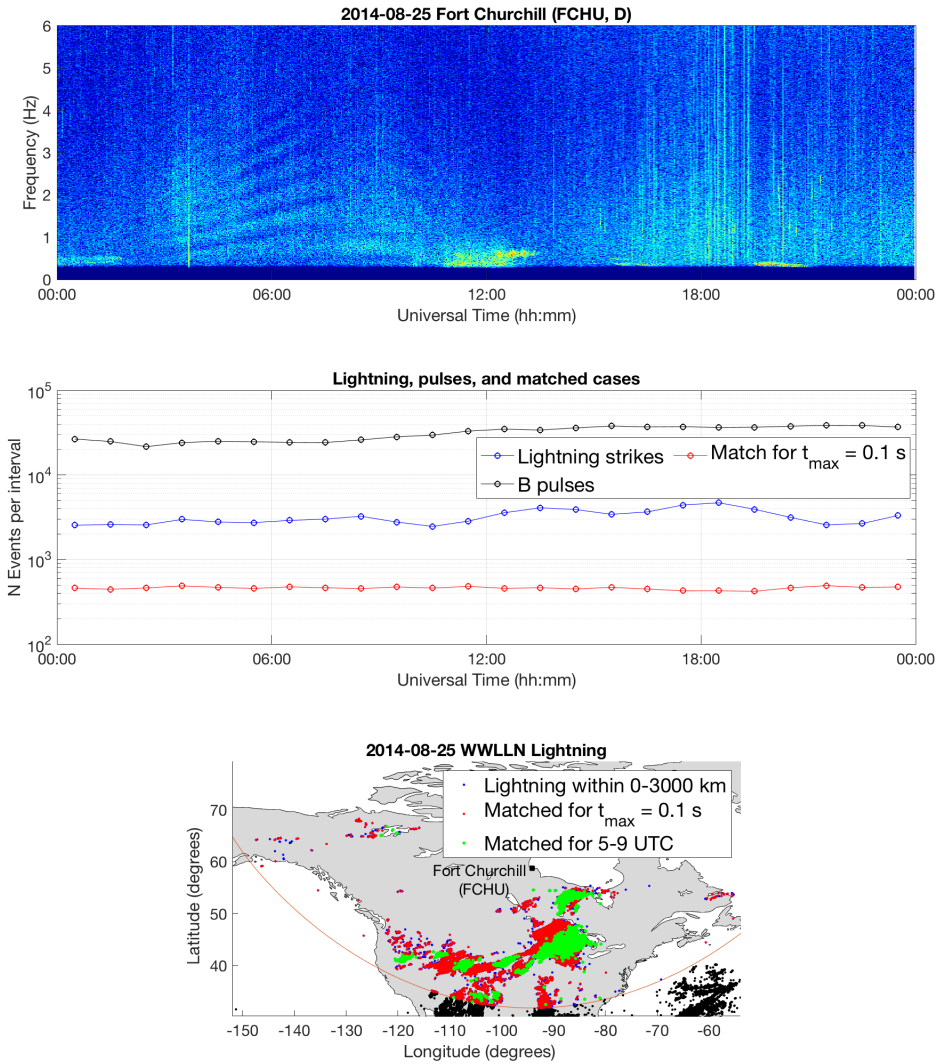
Figure B.10: A case study of lightning strikes matched to magnetic pulses in the Fort Churchill induction coil magnetometer data on August 25, 2014. (Top) The power spectral density plot of the H-component magnetic field data, showing the spectral resonance structures (SRS) of the ionospheric Alfvén resonator (IAR) from ∼04-10 UT. (Middle) Log scale plot of the number of lightning strikes (blue) within 0-3000 km from the Fort Churchill magnetometer station for each UT hour, the number of magnetic pulses (black) with amplitudes above σ_{quiet}, and of those magnetic pulses the subset of ones that occur within 0.1s after a lightning strike (red). (Bottom) A map showing the location of WWLLN lightning strikes relative to the Fort Churchill magnetometer station, where blue dots are lightning strikes that occurred within 0-3000 km but did not match to a magnetic pulse, red dots are lightning strikes that matched to magnetic pulses, and green dots are where the strikes matched to magnetic pulses when the IAR is most active, from 05-09 UT.
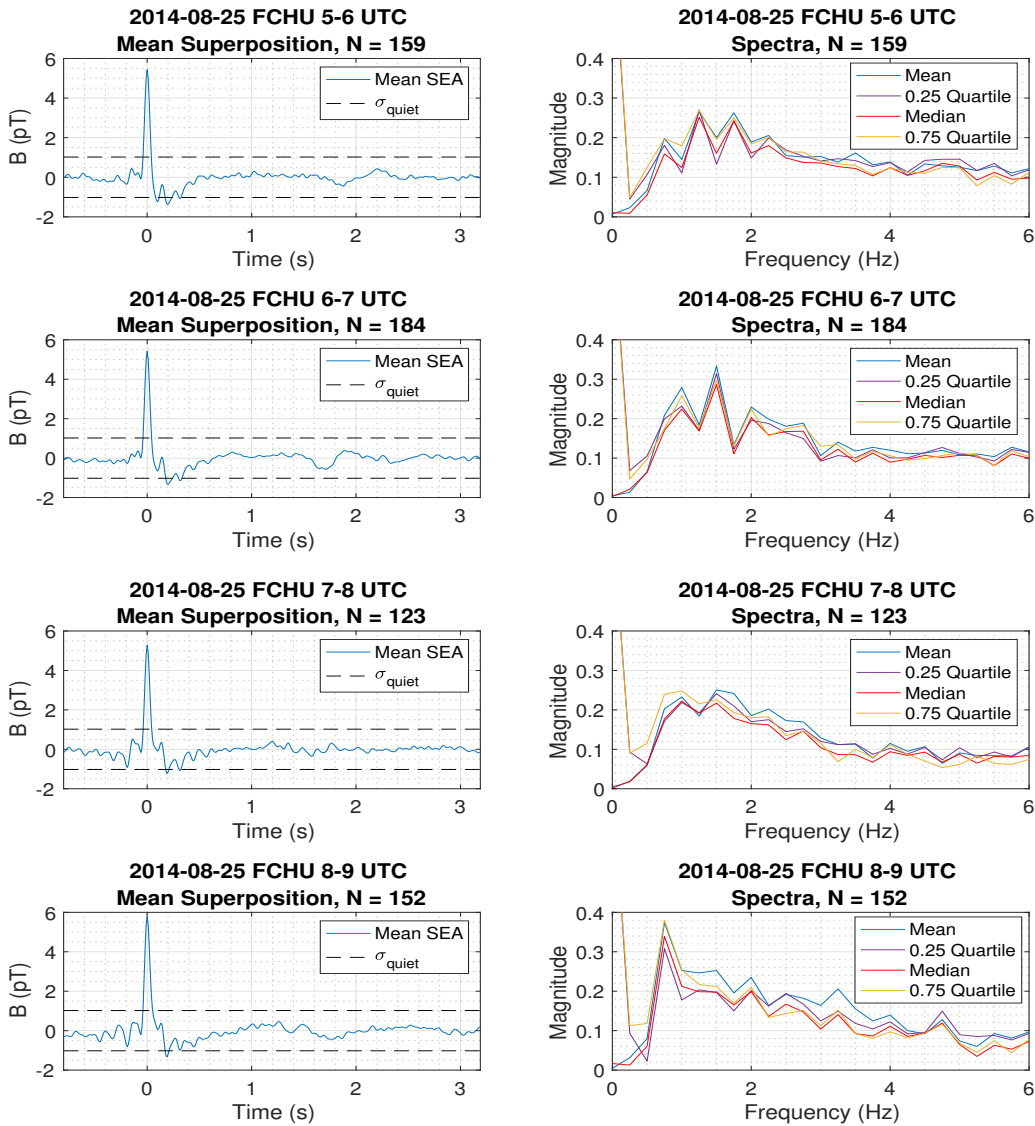
Figure B.11: Mean superposed epoch time series (left column) and spectra (right column) of data from the Fort Churchill magnetometer station matched to WWLLN lightning strikes for four 1-hour time intervals when the IAR is active, from 05-09 UT on August 25, 2014. All magnetic pulses were superposed with positive polarity at epoch time 0 seconds in each 4-second window, and the magnetic threshold of the initial pulse is set at quantile 0.95 above $\sigma_{quiet} = 1$ pT. The first echo from inside the IAR is clearly visible as a negative polarity pulse between T=1.5 s and T=2 s in each panel, for each hour from 05-09 UT, respectively. However, the signal stays below σ_{quiet}, indicating a weak reflection response. The accompanying spectra for 05-06 UT (top right) and 06-07 UT (second right) clearly show the spectral resonance structures of the IAR, for the mean, median and quartiles in the superposed epoch time series. The number of events superposed, N, is above each panel.
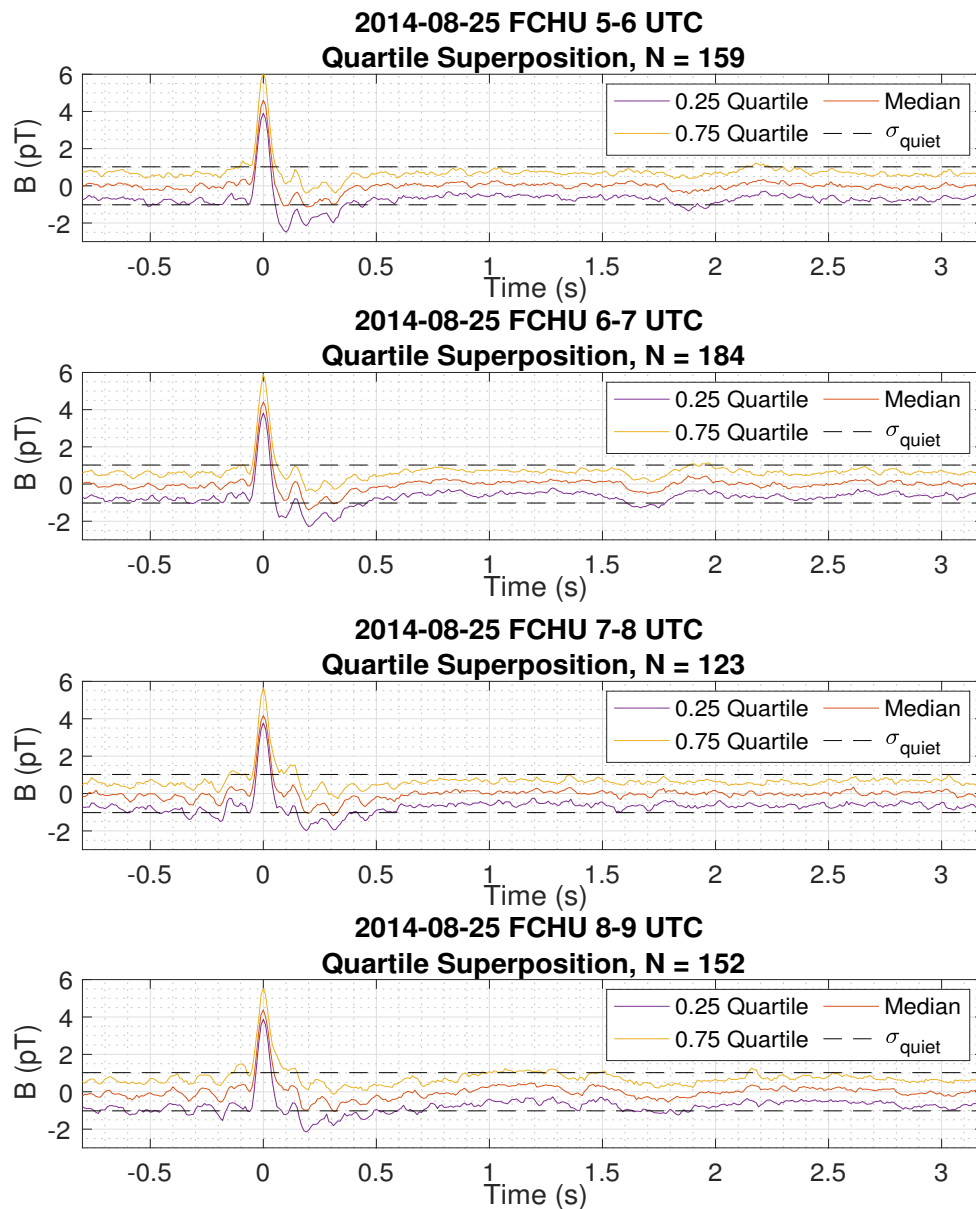
Figure B.12: Median and quartiles time series signals from the superposed epoch analysis of data from the Fort Churchill magnetometer station matched to WWLLN lightning strikes for four 1-hour time intervals when the IAR is active, from 05-09 UT on August 25, 2014. All initial lightning associated magnetic pulses were superposed with enforced positive polarity at superposed epoch 0 seconds in each 4-second window, and the initial magnetic pulse threshold was selected to be quantile 0.95 above $\sigma_{quiet} = 1$ pT. The first echo is clearly visible as a positive polarity pulse between T=1.5 s and T=2 s for each hour from 05-09 UT, respectively. However, the signal stays below σ_{quiet} indicating a weak reflection response. The number of events superposed, N, is above each panel.

Appendix C

A Null Hypothesis Testing the Causal Connection Matching Lightning to Magnetic Pulses

This appendix presents the results of a null hypothesis used to test the validity of the proposed causal connection matching lightning strikes to magnetic pulses in the magnetometer data. The null hypothesis is as follows:

The matching analysis assumes that a lightning strike must be followed by a pulse in the signal measured by an induction coil magnetometer, such that this process is sequentially ordered and time-dependent, not random. Therefore, conducting the same matching and superposed epoch analysis for lightning data on a date that does not correspond to the date of the magnetometer data should result in random noise signals in the superposed time series and which do not reveal the characteristic pulse-echo signal which we associate with both the initial lightning strike related magnetic pulse and its reflection inside the IAR.

Figure C.1 presents the power spectral density plot of magnetometer data for August 25, 2009, a day when the IAR is active, as the SRS are visible in the spectral density plot. Figure C.2 shows the mean superposed epoch time series (left column) and associated frequency spectra (right column) of data from the Ministik Lake magnetometer station on August **25**, 2009 matched to WWLLN lightning strikes from August **24**, 2009 for four 1-hour time intervals when the IAR is active, from 07-11 UT. This was accomplished by creating a copy of

the lightning dataset and changing all the dates from August 24 to August 25, as this modification was simple and did not require any changes in the analysis codes. Figure C.3 provides the time domain superposed responses for the mean, median, and quartiles from which the associated spectra in Figure C.2 are derived. These two Figures C.2 and C.3 demonstrate that combining magnetometer data from one date with lightning strike data from another day, extracting cases that meet the matching criteria for both thresholding and timing (see Chapter 3 for details) and conducting the superposed epoch analysis only reveals a trend corresponding to the Schumann resonances. There is no evidence of a echo signal corresponding to an Alfvén wave reflecting inside the IAR. Figure C.4 reinforces this point by showing the relationship between the lightning strike to magnetometer distance and the propagation time of the strike to the peak of the initial magnetic pulse. The result presented in Chapter 5 for the same analysis revealed a trend marked by regions of high occurrence density between 0.04s and 0.06s, with lines of best fit demonstrating a propagation speed close to the speed of light. In Figure C.4 there are no regions of high occurrance matching a trend, the result is essentially random.

Since the analysis resulted in disorder and no clear pulse-echo signal, the null hypothesis is validated. This confirms the causal connection between the magnetic signals and their ordering by the time of lightning strikes.
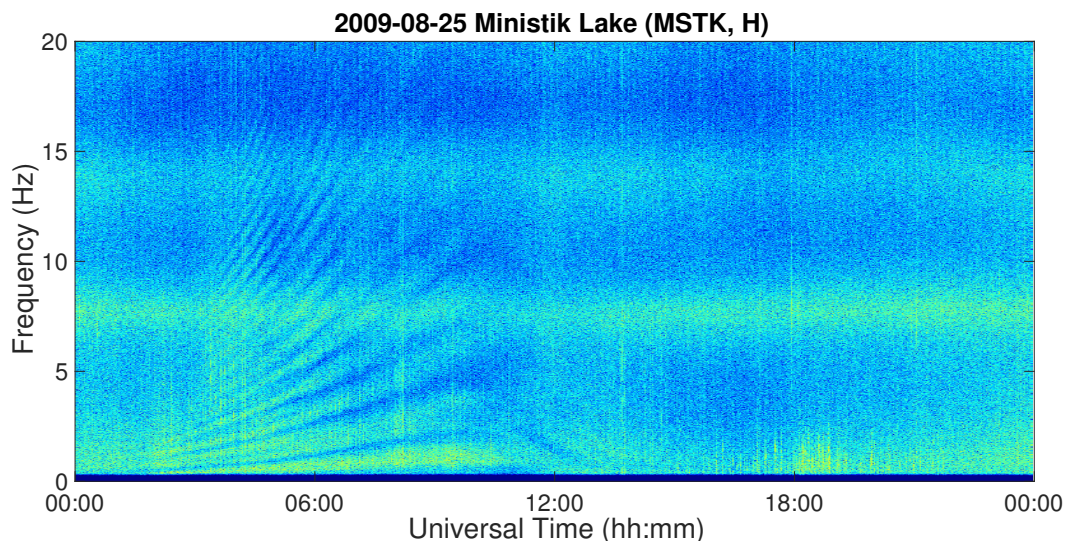
Figure C.1: Power spectral density plot for H (North-South) component induction coil magnetometer data from Ministik Lake on August 25, 2009, exhibiting IAR spectral resonance structures and Schumann Resonances.
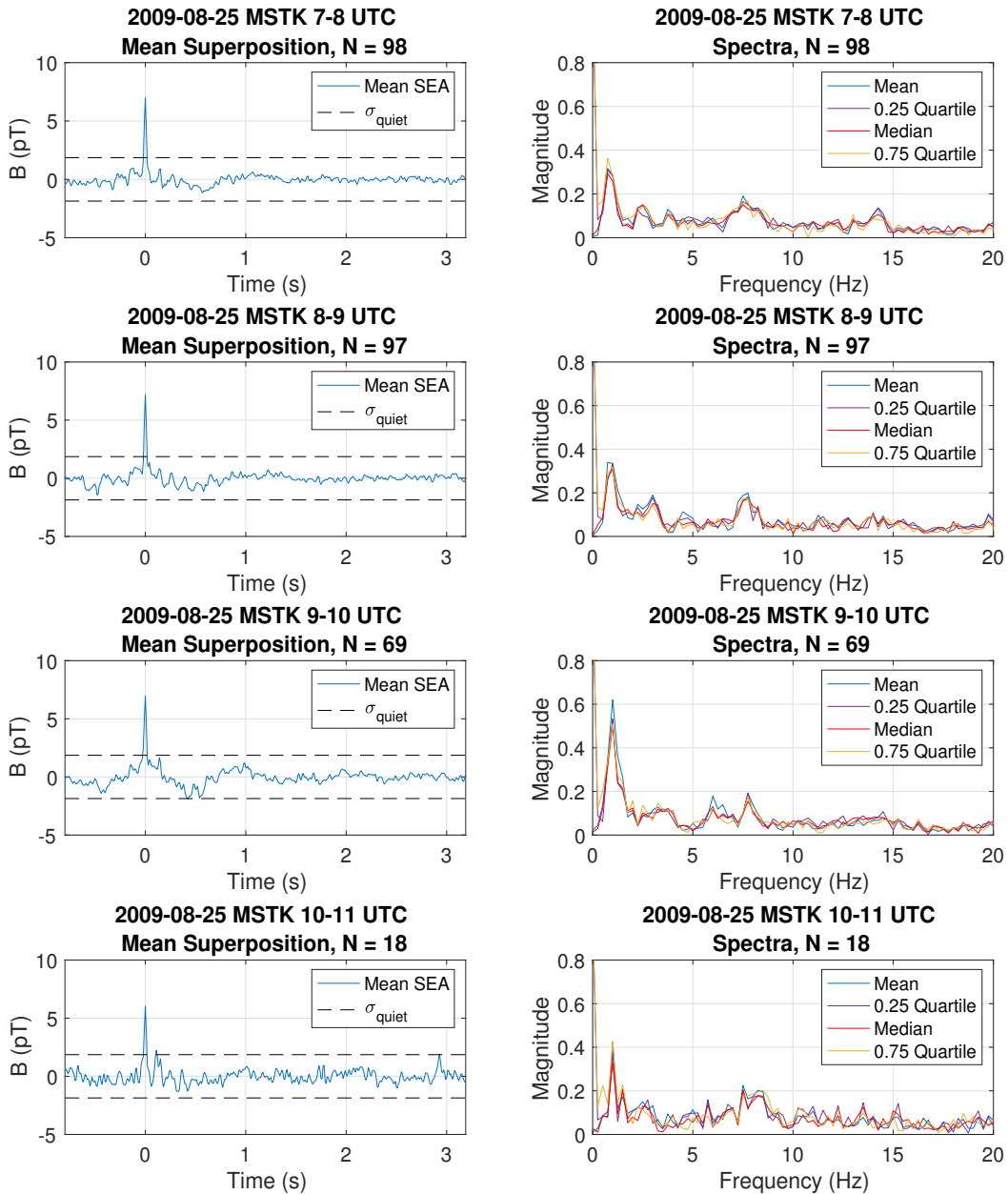
Figure C.2: Mean superposed epoch time series (left column) and spectra (right column) of data from the Ministik Lake magnetometer station for August 25, 2009 matched to WWLLN lightning strikes from August 24, 2009 within 0-2000 km for four 1-hour time intervals when the IAR is active, 07-11 UT. The intentional mismatch results in a randomized matching of events, and so the pulse-echo signature in the superposed interval does not appear. However, the Schumann resonances do appear in the top two sets of panels. All initial lightning associated magnetic pulses were superposed with enforced positive polarity at superposed epoch 0 seconds in each 4-second window, and the initial magnetic pulse threshold is set at quantile 0.9 of $\sigma_{quiet} = 1.9$ pT. The number of events superposed, N, is above each panel.
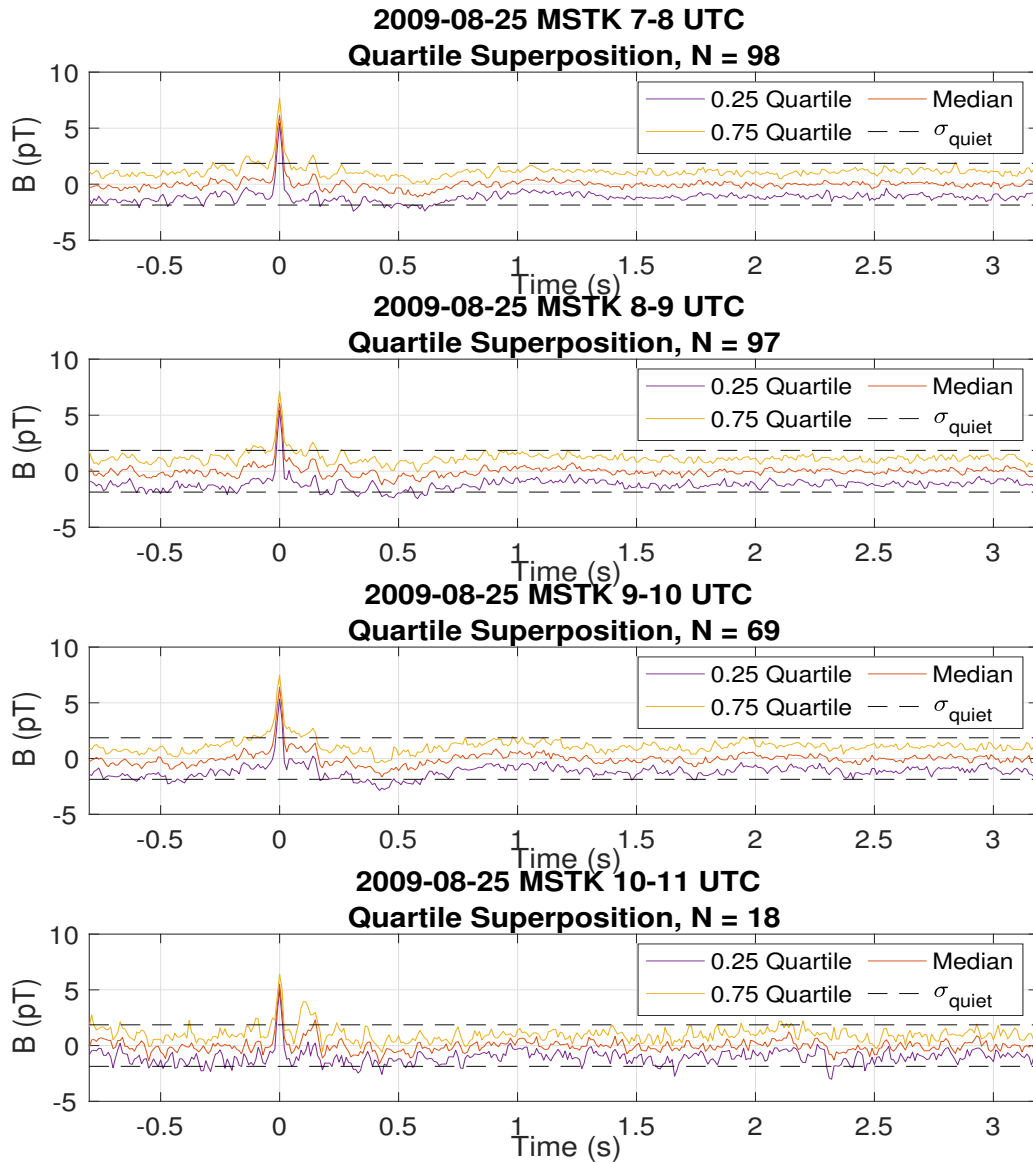
Figure C.3: Median and quartiles superposed epoch time series of data from the Ministik Lake magnetometer station for August 25, 2009 matched to WWLLN lightning strikes from August 24, 2009 within 0-2000 km for four 1-hour time intervals when the IAR is active, 07-11 UT. The intentional mismatch results in a randomized matching of events, and so the pulse-echo signature in the superposed interval does not appear. All initial lightning associated magnetic pulses were superposed with enforced positive polarity at supoerposed epoch 0 seconds in each 4-second window, and the initial magnetic pulse threshold is quantile 0.9 of $\sigma_{quiet} = 1.9$ pT. The number of events superposed, N, is above each panel.
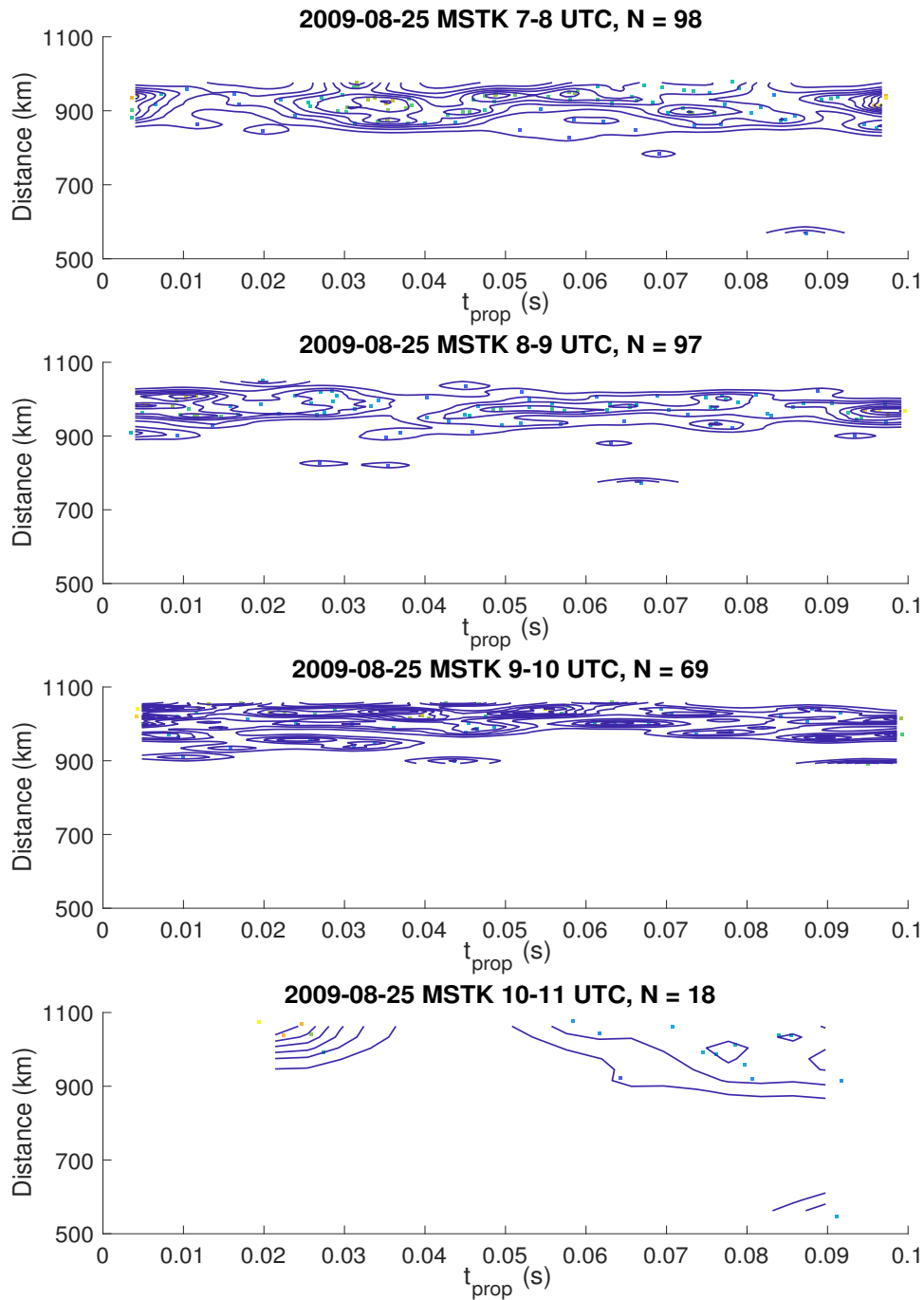
Figure C.4: A case study of the relationship between the lightning strike to magnetometer distance and the propagation time of the strike to the peak of the initial magnetic pulse on August 25, 2009 and WWLLN lightning strikes from August 24, 2009 within 0-2000 km. The scatter plot is combined with density contours identifying the areas of largest occurrence where most data points occur for the Ministik Lake station. There are no clear regions of highest density, it is a very random distribution localized near the storm centre.

Appendix D

Chapter 5 Supplementary Materials

This appendix provides additional results in Figures B.1 to B.12. The time domain superposed responses for the mean, median, and quartiles, corresponding to the results presented in Figures 5.3 to 5.7 in Chapter 5 and from which the associated spectra in Figures 5.3 to 5.7 are obtained. These results show the statistical significance of the initial lightning associated magnetic pulse followed by the echo from reflection of the Alfvén wave inside the IAR for lightning occurrences at distances between 0-10,000 km.
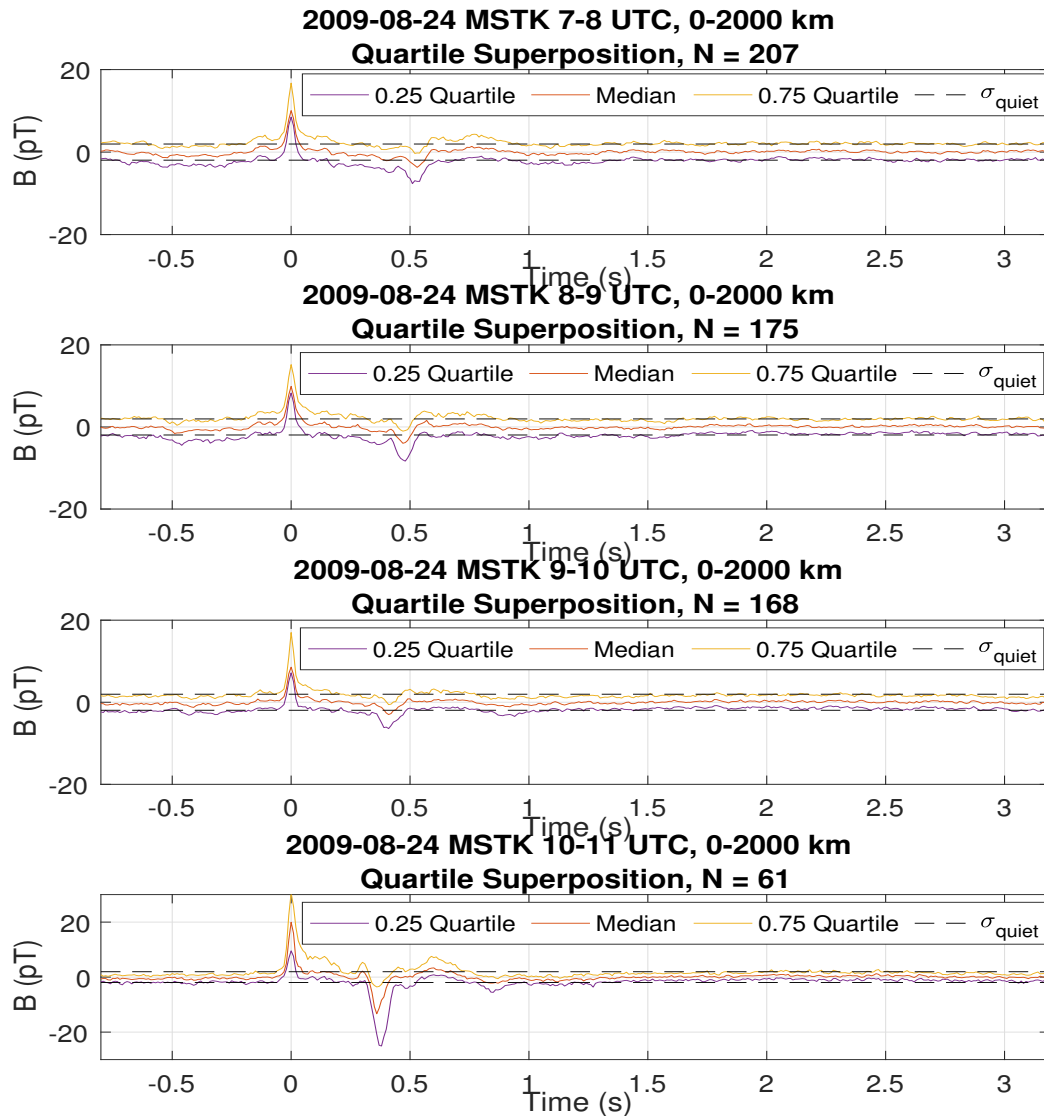
Figure D.1: Median and quartiles time series signals from the superposed epoch analysis of data from the Ministik Lake magnetometer station matched to WWLLN lightning strikes within 0-2000 km for four 1-hour time intervals when the IAR is active, 07-11 UT on August 24, 2009. All initial lightning associated magnetic pulses were superposed with positive polarity at superposed epoch 0 seconds in each 4-second window, and the initial magnetic pulse threshold was selected to be quantile 0.9 of $\sigma_{quiet} = 2$ pT. The first echo from inside the IAR is clearly visible in all three curves as a negative polarity pulse at $T = 0.52$ s (top), $T = 0.47$ s (second), $T = 0.41$ s (third), and $T = 0.37$ s (bottom) for each hour from 07-11 UT, respectively. The number of events superposed, N, is above each panel.
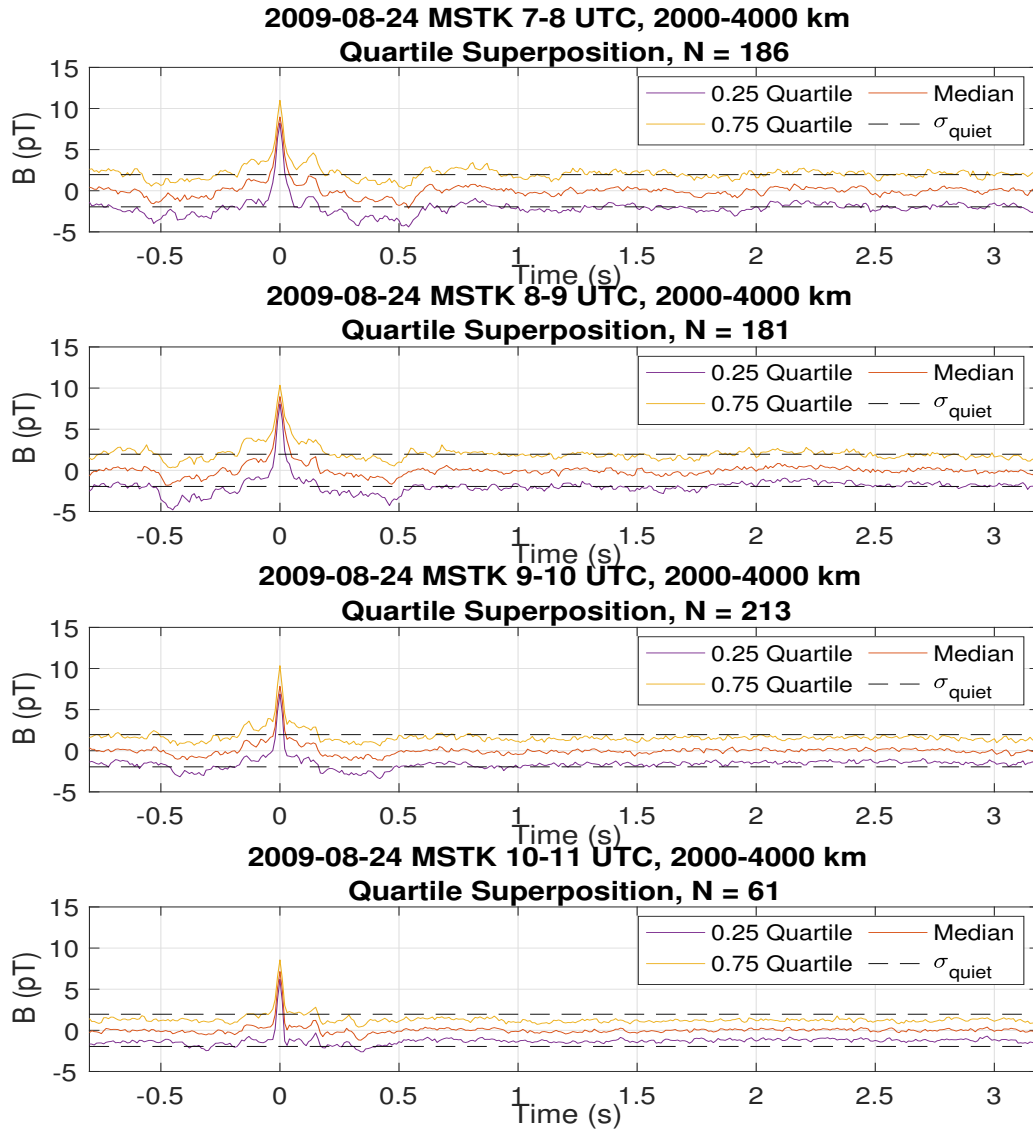
Figure D.2: Median and quartiles time series signals from the superposed epoch analysis of data from the Ministik Lake magnetometer station matched to WWLLN lightning strikes within 2000-4000 km for four 1-hour time intervals when the IAR is active, 07-11 UT on August 24, 2009. All initial lightning associated magnetic pulses were superposed with positive polarity at superposed epoch 0 seconds in each 4-second window, and the initial magnetic pulse threshold was selected to be quantile 0.9 of $\sigma_{quiet} = 2$ pT. The first echo from inside the IAR is visible in all three curves as a negative polarity pulse between T=0.3 s and T=0.5 s, for each hour from 07-11 UT, respectively. The number of events superposed, N, is above each panel.
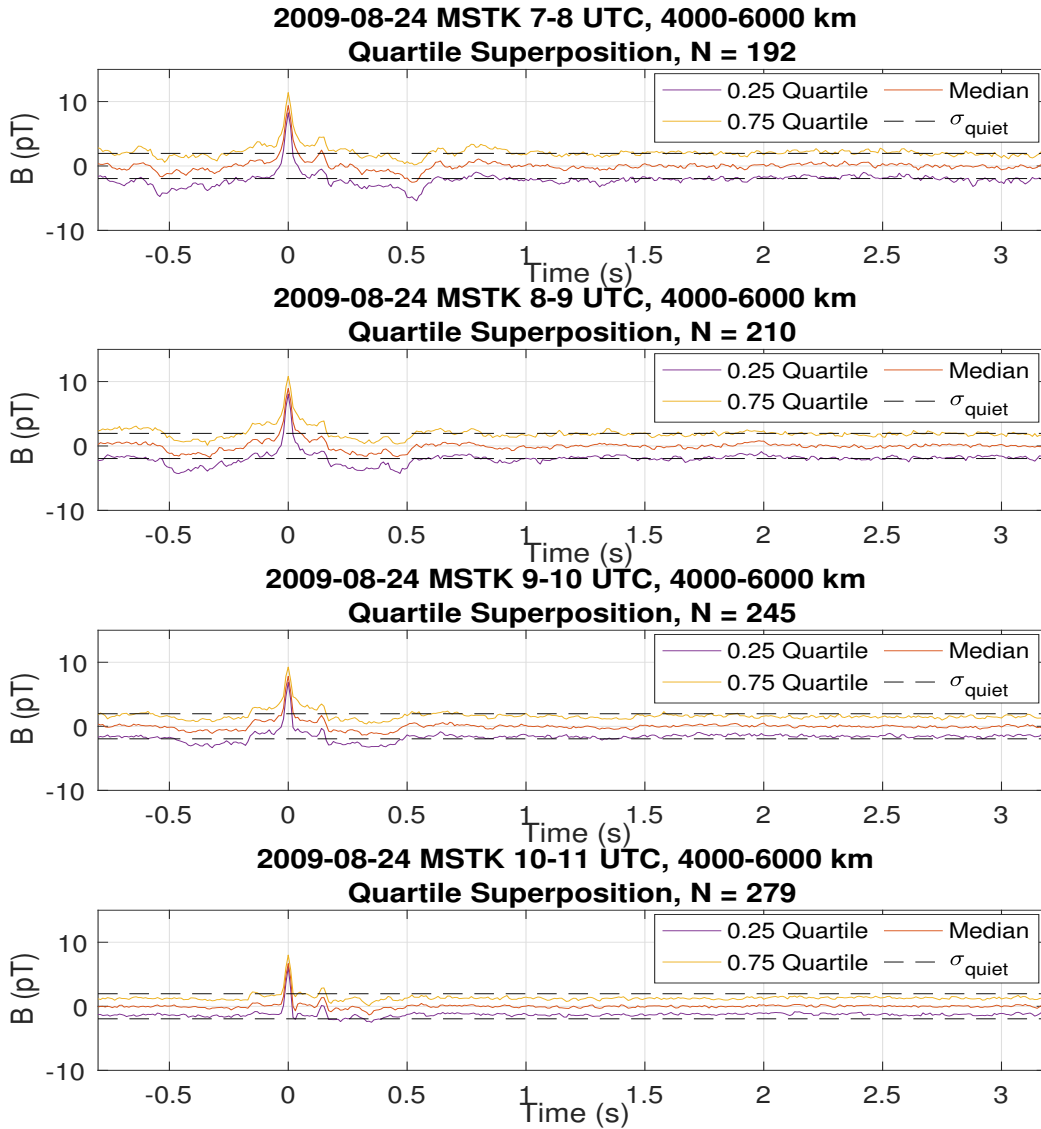
Figure D.3: Median and quartiles time series signals from the superposed epoch analysis of data from the Ministik Lake magnetometer station matched to WWLLN lightning strikes within 4000-6000 km for four 1-hour time intervals when the IAR is active, 07-11 UT on August 24, 2009. All initial lightning associated magnetic pulses were superposed with positive polarity at superposed epoch 0 seconds in each 4-second window, and the initial magnetic pulse threshold was selected to be quantile 0.9 of $\sigma_{quiet} = 2$ pT. The first echo from inside the IAR is visible in all three curves as a negative polarity pulse between T=0.3 s and T=0.5 s, for each hour from 07-11 UT, respectively. The number of events superposed, N, is above each panel.
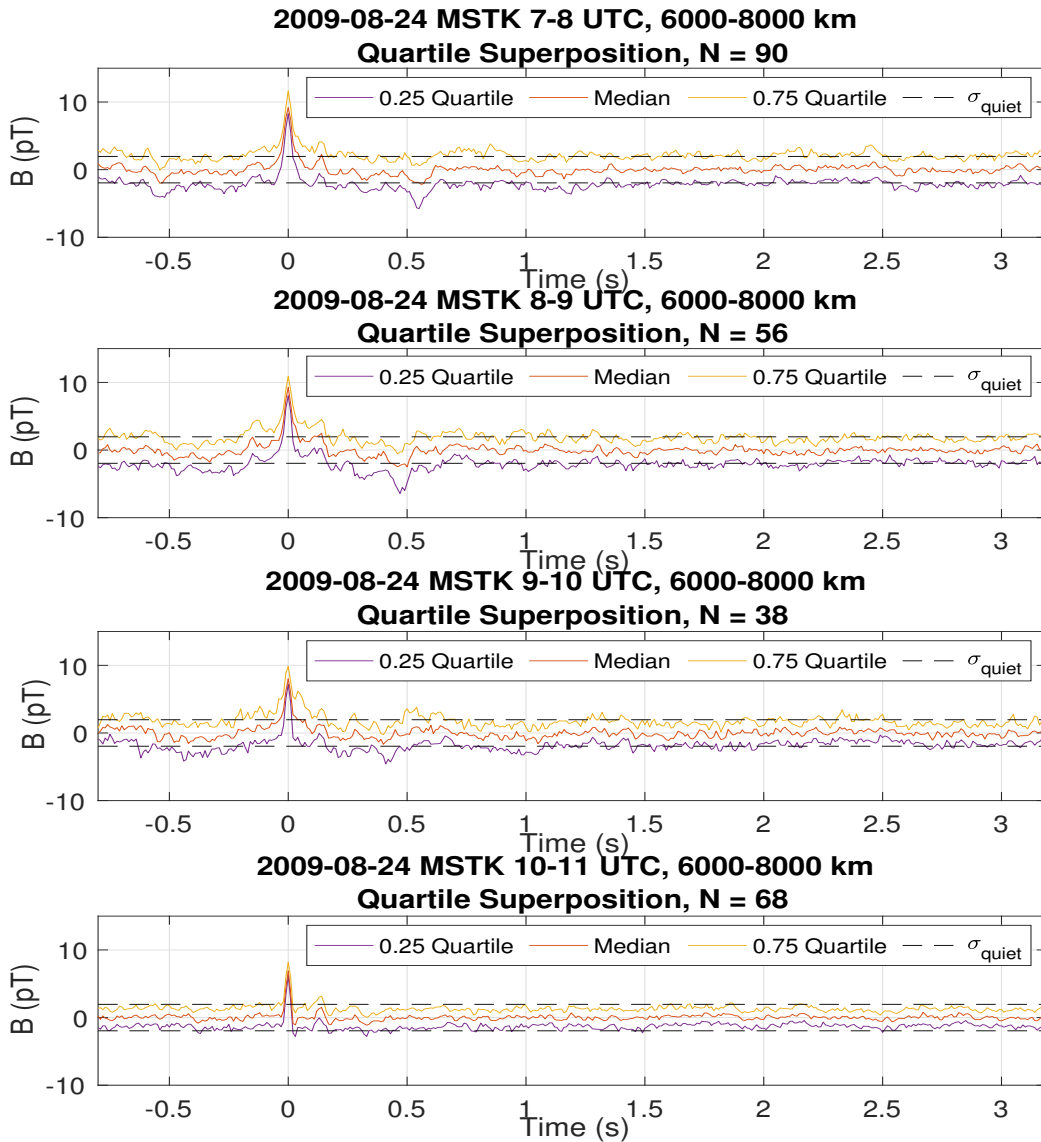
Figure D.4: Median and quartiles time series signals from the superposed epoch analysis of data from the Ministik Lake magnetometer station matched to WWLLN lightning strikes within 6000-8000 km for four 1-hour time intervals when the IAR is active, 07-11 UT on August 24, 2009. All initial lightning associated magnetic pulses were superposed with positive polarity at superposed epoch 0 seconds in each 4-second window, and the initial magnetic pulse threshold was selected to be quantile 0.9 of $\sigma_{quiet} = 2$ pT. The first echo from inside the IAR is visible in all three curves as a negative polarity pulse between T=0.3 s and T=0.5 s, for each hour from 07-11 UT, respectively. The number of events superposed, N, is above each panel.
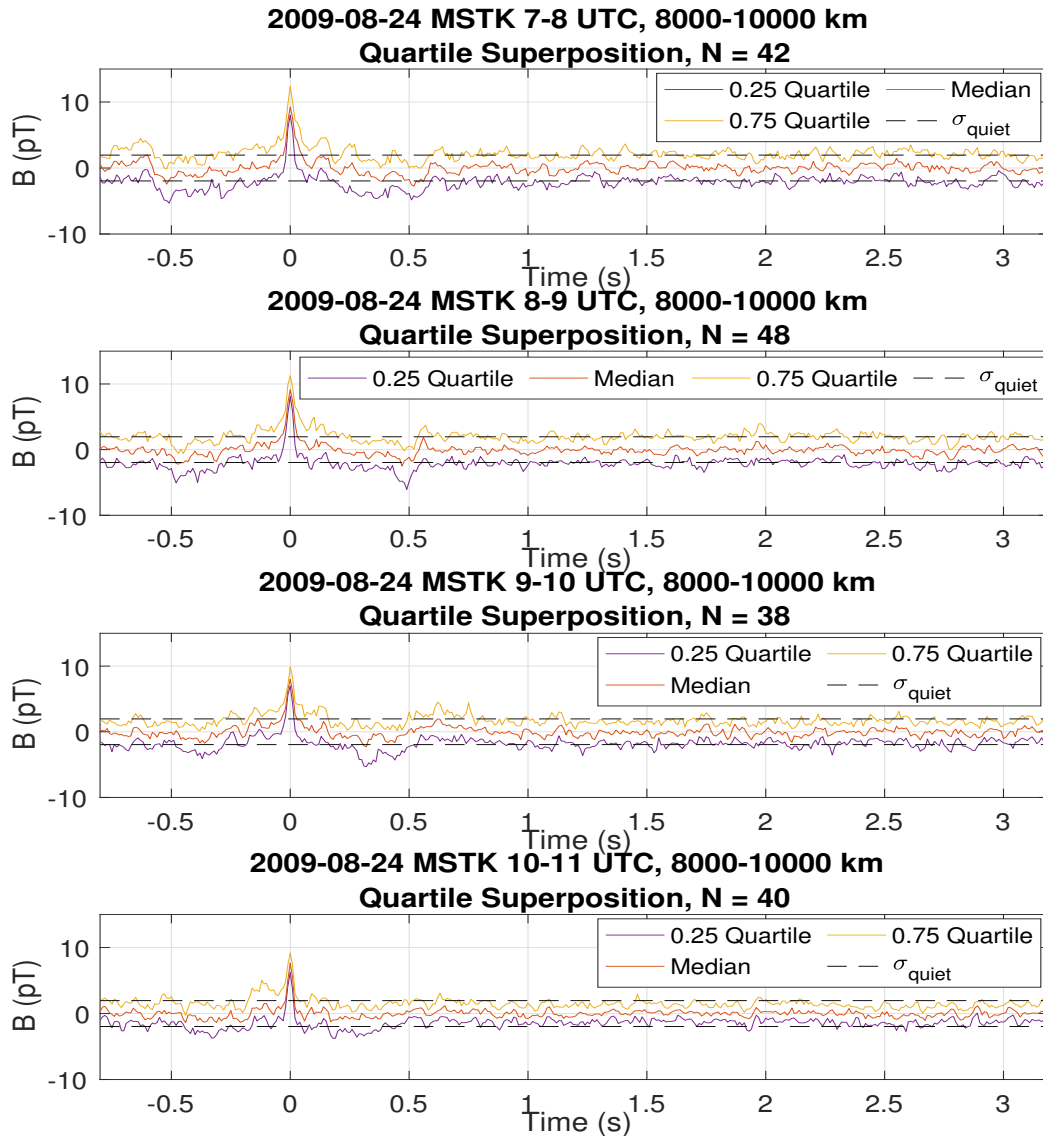
Figure D.5: Median and quartiles time series signals from the superposed epoch analysis of data from the Ministik Lake magnetometer station matched to WWLLN lightning strikes within 8000-10,000 km for four 1-hour time intervals when the IAR is active, 07-11 UT on August 24, 2009. All initial lightning associated magnetic pulses were superposed with positive polarity at superposed epoch 0 seconds in each 4-second window, and the initial magnetic pulse threshold was selected to be quantile 0.9 of $\sigma_{quiet} = 2$ pT. The first echo from inside the IAR is visible in all three curves as a negative polarity pulse between T=0.3 s and T=0.5 s, for each hour from 07-11 UT, respectively. The number of events superposed, N, is above each panel.

Appendix E

MATLAB Code

Code for the analysis in this thesis was written in Matlab. 26 Matlab functions were created in all. All 26 functions have been deposited in the Education & Research Archive (ERA) of the University of Alberta as Matlab files in a deposit titled MATLAB functions for Lightning Excitation of the Ionospheric Alfvén Resonator by Charles Nokes and can be found by searching the following list of keywords on the ERA portal (https://era.library.ualberta.ca/): **Lightning, Ionosphere, Excitation, Ionospheric Alfvén Resonator, code, Matlab, function, CARISMA, WWLLN, solar, terrestrial**, or by going to this link: https://era.library.ualberta.ca/items/0d588fc1-74fc-4744 -b94f-2b071ee1c6dc

E.1   Getting Started

lightning_and_iar.m is the function in which all the main input parameters are set. It then calls the next function, *lightning_and_iar_functions.m*, which takes all the inputs and runs all the other functions to analyze and plot the data, producing the figures in this thesis and more.

E.2   Questions

For questions please email Charles Nokes: cnokes@ualberta.ca, or Professor Ian Mann: imann@ualberta.ca